The Effects of Temperature and Microstructure on Slip Localization in Microtextured Ti-6Al-2Sn-4Zr-2Mo under Dwell Fatigue

by

Michelle E. Harr

A dissertation submitted in partial fulfillment
of the requirements for the degree of
Doctor of Philosophy
(Mechanical Engineering)
in the University of Michigan
2021

Doctoral Committee:

Professor Samantha Daly, Co-Chair, University of California Santa Barbara
Professor Katsuo Kurabayashi, Co-Chair
Professor John Allison
Professor James Barber
Dr. Adam Pilchak, Air Force Research Labs

Michelle E Harr

meharr@umich.edu

ORCID iD: 0000-0001-5905-7448

Acknowledgements

The research was financially supported by the National Science Foundation Graduate Research Fellowship under Grant No. 1256260 DGE and the Air Force Research Labs under Contract #FA8650-16-C-5235.

I would like to first thank and acknowledge my advisor, Professor Samantha Daly. Thank you for the tremendous amount of expertise, mentorship, advice, and patience over the last 5+ years. The experiments in this thesis were incredibly trying, so thank you for always encouraging me to keep at it while reminding me to measure 12 times and cut once. You have provided support through this academic PhD thesis, as well as a cross country university move and many other life changes. Thanks for bringing me to UCSB and making it possible to complete my degree at the University of Michigan. I know it wasn’t simple, and I appreciate your commitment to me and this project from the beginning.

I need to thank Professor Katsuo Kurabayashi and Professor Jim Barber for their instrumental involvement in my work at the University of Michigan and for acting as my co-advisors. I really appreciate all the time, energy, and effort you have put in to help me complete my graduate studies. I couldn’t have done this without you both.

I would also like to thank my AFRL co-advisor, Dr. Adam Pilchak, for hiring me as an intern during undergrad and continuing to whole-heartedly support me for the past 8 years. Your insight and expertise are invaluable to both this project and my career. Thanks for always investing in me and encouraging me to invest in others. I am thankful for your kindness, patience, mentorship and advice. I owe my love of titanium, old school metallurgy, and MATLAB to you.

I would also like to thank the remaining member of my committee, Dr. John Allison, for his insight and advice on this PhD project, specifically on how to focus my research interests.

I must also specifically thank Kirk Fields for his help and insights with experimental methodologies and testing. Without your expertise in the mechanical testing lab and advice on rigging heated tests, these experiments never would have been possible. Thank you for the significant amount of time you spent running experiments with me when I would fly to UCSB and only had a week to run experiments - you taught me about the time it *actually* takes to run an experiment and what a reasonable test plan looks like. I would also like to thank you for the moral boosts, support, and fun conversations through every part of this process.

I must acknowledge the informative conversations and troubleshooting on instrumentation, experimental methodologies, analysis techniques, and titanium theory with Dr. J.C. Stinville, Dr. Patrick Callahan, Dave Bothman, Dr. Claire Chisholm, Mark Cornish, Dr. Aidan Taylor, Darin Randall, Chris Torbet and Dr. J. Wayne Jones. I greatly appreciated every patient, informative response to every frantic email I sent over the past five years.

My fellow Daly group members, past and present, were instrumental in providing experimental guidance, analysis advice, camaraderie, and friendship. Thank you to Dr. Zhe Chen, Dr. Jason Geathers, Dr. Joyce Yue Gong, Dr. Will Lepage, Dr. Marissa Linne, Dr. Neal Brodnik, Anna Washabaugh, Bhavana Swaminathan, Jeffrey Rossin, Jayden Plumb, Caelin Muer, Andrew Christison, Madeline Dippel, Clement Baillieul, Daisy Zavala, Aine McNulty, Casey Magid, and Daniele Offidani. I would like to specifically thank Dr. Zhe Chen for sharing all his knowledge and codes for the external scan controller, DIC data processing, and titanium orientation mapping. It was only by building on the experimental and analysis foundations he provided that this progress to our understanding of dwell fatigue in titanium was possible. I would also like to highlight the undergraduates who have given me the pleasure of working with and have directly contributed to the work in this thesis. Thanks to Daniele Offidani, Aine McNulty, and Casey Magid for taking on time consuming DIC analysis, segmentation tasks, and stitching tasks that were vital to the progress of this project.

I would like to thank my family for all their love and support throughout my education. Thank you for caring about me and asking about my research, even if I'm not sure you particularly understand (or care) about titanium dwell fatigue. I appreciate your listening ears when times were trying, and your constant encouragement to hold to the Harr motto, "Finish Strong".

Finally, I must thank my colleague and partner, Dr. Glenn Balbus. Thank you for sputtering my samples with silver for me; otherwise I would likely still be in the lab at all hours attempting to achieve a good DIC pattern to this day. Without your love, care, support, humor, listening ear, and cooking, my life would be far less fulfilled and far less joyful. I love you. Thank you for completing your PhD journey alongside mine, and I look forward to continuing our life journey together.

Table of Contents

List of Tables

List of Figures

Abstract

Near-alpha titanium alloys, such as Ti-6242, experience a reduction in fatigue lifetime when the peak stress is held for each loading cycle. This type of sustained peak loading is known as dwell fatigue, and it mimics the long durations of high mean stress that gas turbine engine disks experience during aircraft takeoff. The significant reduction in lifetime, known as the dwell debit, is attributed to the phenomenon of load shedding. Load shedding occurs when an alpha grain well oriented for slip, termed a soft grain, lies adjacent to an alpha grain poorly oriented for slip, termed a hard grain. At the same macroscopic load, the soft grain stress relaxes and loses its ability to carry load, thereby requiring the hard grain to carry a higher load, creating stress localization. The region of high local stress acts as a favorable location for early crack nucleation relative to standard low cycle fatigue models. This phenomenon is known to be affected by local microstructure and temperature, but the underlying mechanisms are not well understood.

This work utilized Digital Image Correlation with Scanning Electron Microscopy and Electron Backscatter Diffraction at multiple length scales to experimentally investigate and statistically quantify the effects of temperature and microstructure on strain localization and damage accumulation of Ti-6242 during dwell fatigue loading. Plastic strain accumulation was observed in heavily microtextured Ti-6242 under dwell fatigue loading at room temperature, 120°C, and 200°C. After 2 and 200 dwell cycles, plastic deformation maps of the 4 mm x 2.5 mm and 500 µm x 500 µm with over 150 million data points were collected to investigate the full gauge response and the response of individual grains. Slip traces traversing through 1 to as many as 140 grains were segmented from each deformation map. The length of each slip trace, orientation, and

Schmid factors of the grains each trace traverses through, and the active slip family for each trace were studied to identify the critical grain characteristics that allow for the percolation of long-range plastic slip. The room temperature and 120°C cases had significantly more plastic slip activity than the 200°C case. At every temperature, plasticity occurred primarily as long-range basal slip traces through grains with a high basal Schmid factor that were located in subfeatures of microtextured regions, as defined by the current prevailing methods. While there was almost no prismatic slip activity at any temperature or length scale, a significant amount of short-range pyramidal slip occurred in regions near the long-range basal slip traces. These slip family trends were clear after 2 dwell cycles and remained constant with additional cycling to 200 dwell cycles. These findings indicate the microstructure of the material, specifically the distribution of basally soft grains, dictates the location of plastic strain accumulation from very early dwell cycling regardless of temperature. Microstructural regions that behave as a unit under plastic deformation are bound by regions with a low basal strength-to-stiffness, a metric which relates the propensity basal Schmid factor and the effective elastic modulus of a microstructural region. These results are relevant to the phenomenon of load shedding and the dwell fatigue debit, and they can be used to inform and improve current and future temperature-dependent dwell fatigue models and MTR segmentation strategies.

Chapter 1 Introduction

Near-alpha titanium alloys have an excellent strength-to-weight ratio, highly tailorable mechanical properties, and are corrosion resistant, leading to their widespread adoption in aerospace applications. In particular, the titanium alloy Ti-6242 is under widespread use in the compressor disks and blades of gas turbine engines. The compressor disk and blades within the intermediate pressure section of gas turbine engines are considered life critical and require reliable lifetime predictions [1]. When designing and maintaining these components, a parameter for which the mechanisms are not well understood is dwell fatigue. Due to this knowledge gap, fan and compressor disks are failing unexpectedly early, causing dangerous and expensive failures.

Dwell fatigue is characterized by a constant hold at the peak of each load cycle, creating a trapezoidal waveform. The hold models the sustained peak stress that components experience during take-off, and to a lesser extent the cruise between take-off and landing. Each flight represents one dwell cycle in a laboratory setting. The disk dwell fatigue lifetimes of titanium with this hold at peak load are dramatically shorter than the lifetimes predicted by standard cyclic fatigue estimates. This reduction in lifetime is termed the *dwell debit*. In Ti-6242, the dwell debit is commonly ten to twenty times below the lifetime predicted by low cycle fatigue calculations.

A recent in-service example of a dwell fatigue engine failure in another titanium alloy, Ti-6Al-4V, occurred in an Airbus A380 in September 2017. The full report of the Air France A30 failure investigation from the Bureau of Enquiry and Analysis of Civil Aviation Safety (BEA) was released on September 25, 2020 [2]. The report details that the GP7200 No. 4 engine failed with an explosion five hours into the flight. The report suggests that the crack initiated after 1,800 cycles and subsequently failed at 3,500 cycles, which is four times earlier than the originally predicted 15,000 cycle minimum. The plane was able to land safely with no injuries to crew or passengers, but the fan hub separated into at least three parts, destroyed the engine casing, and struck the wing and airframe of the plane. Historically, dwell fatigue failures and resultant liberated turbine disks and blades can lead to catastrophic engine failures. Confirmed dwell fatigue flight failures include the GE CF34-3 failure in Barcelona in 2008 and the GE CF6 failure in Beijing in 1997, among others which can be found in the National Transportation Safety Board (NTSB) database [3]. To prevent these dangerous and expensive dwell fatigue failures, the titanium and aerospace community must develop a better understanding of the mechanisms and contributing factors to the initiation of dwell fatigue cracks and the dwell debit. For near-alpha titanium alloys, the dwell debit is attributed to the phenomenon of load shedding.

Load shedding is believed to occur due to the anisotropy of the HCP structure of the primary alpha particles in near-alpha titanium alloys. Depending on the relative angle between the load direction and the c-axis of the grain orientation, grains can be categorized as hard or soft. At the same macroscopic load, soft grains can easily slip and deform while the hard grains resist deformation. When dislocations from the soft grain meet the hard-soft interface, they cannot traverse into the hard grain and instead pile up at the boundary. This causes the soft grain to shed its load onto the hard grain, creating a high localized stress that promotes early crack nucleation and faceting, therefore drastically reducing the component’s fatigue lifetime [4]–[9]. This phenomenon is known to be impacted by temperature and local microstructure.

Local microstructure, specifically microtextured regions (MTRs) and their intensity, has an important but little understood effect on dwell fatigue lifetimes [10]. MTRs are currently identified by clustering similarly oriented α grains or particles with a ± 20° tolerance on the c-axis misorientation and permitting non-contiguous grouping [10]–[12]. This method produces MTRs that compare favorably with the size of the faceted initiation sight of fractured dwell fatigue samples [9], [11]–[13]. With relation to the dwell debit, it has been hypothesized that MTRs behave as giant grains that allow for large dislocation pile ups, but this theory has not been rigorously explored or validated.

Empirically, it is known that the dwell debit exists at room temperature and peaks at ~120°C. At temperatures at 200°C and above, the dwell debit disappears, and dwell fatigue lifetimes match LCF lifetimes. This non monotonic phenomenon is hypothesized to be due to a combination of a temperature dependent reduction in anisotropy and/or a temperature dependent strain rate sensitivity but has yet to be experimentally validated [14]–[16].

Although load shedding is attributed as the primary driver of dwell debit in Ti-6242, the associated strain distributions and their relationship to the microstructure and temperature have never been directly observed or validated. This work describes the quantitative characterization of strain localizations and their evolution, with relation to the local microstructure and experimental temperature, providing new insights into load shedding under dwell fatigue. Ex-situ studies were performed at room temperature (RT), 120C and 200C where Ti-6242 samples were loaded via dwell fatigue and interrupted at predetermined cycle intervals to capture the deformation response.

This work utilizes orientation information collected from electron backscatter diffraction (EBSD) and full-field plastic strain maps from digital image correlation performed in a scanning electron microscope (SEM DIC). The orientation and strain maps are aligned, which allow for the extraction and study of the temperature and local microstructural features that contribute to slip initiation and propagation over a large region.

This thesis is structured into seven chapters. Chapter 1 details the motivation for this project and provides an overview of the contents of this thesis. Chapter 2 outlines the necessary literature review and background information to understand the current theories and hypothesis relates dwell fatigue, crack initiation, and load shedding. In Chapter 3, the experimental methods of EBSD and SEM DIC were utilized to study the influence of temperature and local microstructure on the plastic strain distribution during dwell loading of Ti-6242. The deformation of groups of grains under dwell fatigue loading at RT, 120°C, and 200°C is studied over the whole gauge (4mm x 2.5mm) section of dwell samples to understand the cooperative behavior of MTRs described in Chapter 4. Chapter 5 utilizes results from the groups of grains that work cooperatively to allow for long range slip in the whole gauge section of samples to suggest the use of a strength-to-stiffness metric for defining MTRs for crack initiation and load shedding. The behavior of MTRs and cooperative clusters of grains is compared to the slip behavior of individual grain in smaller regions of interest at RT and 200°C to understand if MTRs can be considered as large grains in Chapter 6. Finally, in Chapter 7, the conclusions from the previous chapters are summarized and future work based on these findings is suggested.

Chapter 2 Background

2.1 Structure of Titanium Alloys

2.1.1 Crystal Structure

Pure titanium exhibits two predominant crystal structures, a low temperature hexagonal close packed (HCP) alpha (α) phase and a body centered cubic (BCC) beta (β) phase, as shown in Figure 2.1 [17]. For pure titanium, the α->β (HCP-BCC) allotropic phase transformation occurs at a temperature of 882°C [17]. This transformation temperature is referred to as the beta transus temperature and is heavily influenced by substitutional and interstitial alloying additions. The most common alloying element for titanium alloys is aluminum, as it is the only common metal which raises the beta transus temperature. Aluminum acts as a substitutional atom in the titanium lattice and it is highly soluble in both the α and β phase. The effects of aluminum additions on the beta transus temperature of Ti-Al alloys can be seen in the phase diagram in Figure 2.2 [18]. Other alloying additions such as oxygen, nitrogen, and carbon, all of which are interstitial species in the Ti lattice, are also commonly used as alpha stabilizers. While boron, gallium, germanium, and rare earth elements are also known to act as alpha stabilizers, none of them are commonly used as alloying elements since they are much more scarce and have a much lower solid solubility in titanium than aluminum and oxygen. Both the amount of alloying additions and the thermomechanical processing route determine the morphology of the microstructure and volume fraction of the alpha and beta phases. Depending on the relative concentrations of the α and β stabilizers, titanium alloys are typically categorized as α, near-α, α +β, or β alloys.

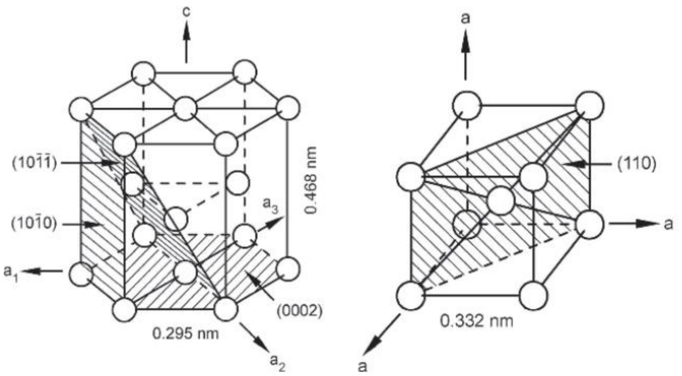

Figure 2.1:Unit cell structure of alpha and beta titanium [17]

2.1.2 Alloying and Processing

The alloy used in this thesis is Ti-6242, which is an α + β alloy with aluminum, tin, zirconium, and molybdenum additions [17]. Specifically, in Ti-6242, tin and zirconium behave as alpha stabilizers. They are thermodynamically neutral in titanium, but segregate to the alpha phase due to the chemical similarity of zirconium to titanium and the fact that tin can replace the aluminum in the hexagonal ordered Ti_3Al phase (α_2). Molybdenum acts as an isomorphous beta stabilizer and allows for the beta phase to stabilize at room temperature. These effects are shown schematically in Figure 2.3.

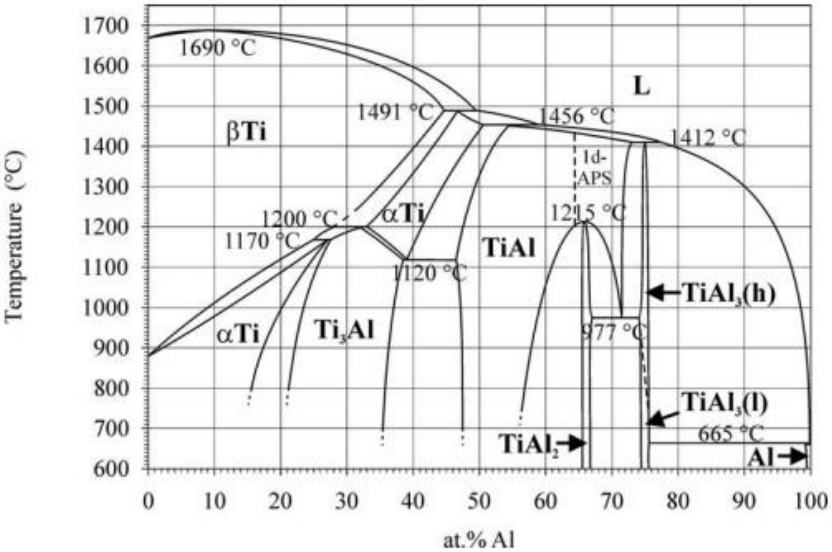

Figure 2.2: Ti-Al Phase Diagram [18]

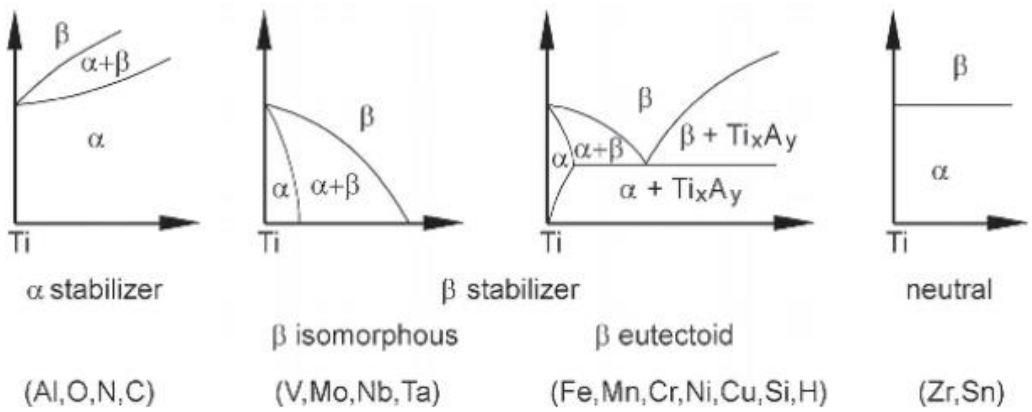

Figure 2.3: Effect of alloying elements on titanium phase diagram show schematically [17]

The thermomechanical processing of α + β alloys can be tailored to produce three specific microstructures: fully lamellar, fully equiaxed, or a bi-modal microstructure. The Ti-6242 used in this study was processed to produce a fully equiaxed microstructure. Fully equiaxed microstructures are typically produced in a four-step process: homogenization, deformation, recrystallization, and annealing. The first is homogenization of the beta phase field above the beta transus temperature. The cooling rate from the homogenization temperature is critical for determining the resultant microstructure, as it determines the thickness of the alpha lamella formed during cooling. Slower cooling rates result in thicker alpha lamellae, which relates to a larger final alpha particle size. Next, the material is deformed plastically to introduce sufficient dislocation content for complete recrystallization during the next step. Step III is the recrystallization process, where annealing at temperatures below the beta transus temperature allows for dislocation evolution (e.g. cell formation, sub-grain boundary formation) and the eventual formation of new alpha grains with few residual dislocations. The temperature that this step is performed at determines for volume fraction of recrystallized equiaxed primary alpha grains, and a low cooling rate is required for fully equiaxed structures to prevent further alpha lamellae formation within the beta phase and allow only the recrystallized alpha particle grains to grow during this step. The final annealing heat treatment temperature determines whether Ti_3Al particles will form or not. At lower temperatures Ti_3Al will precipitate and age-harden the alpha phase, whereas higher temperature annealing will only act as a stress relieving treatment. Additionally, the annealing temperature will dictate the formation of secondary alpha in the beta phase of the material. The material in this study has been processed to contain only a small amount of the beta phase (less than 10 % by volume) and is termed a near-alpha alloy. A summary of the processing route for full equiaxed $\alpha + \beta$ titanium alloys and the influence of different processing parameters is summarized in Figure 2.4 and Table 2.1 [17].

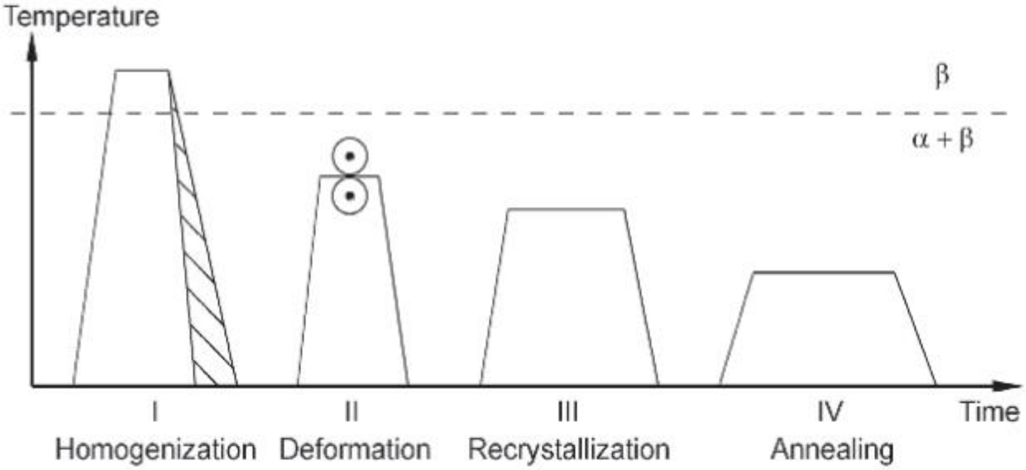

Figure 2.4: Processing route for fully equiaxed microstructure of α+β titanium alloy recrystallized at low temperatures schematically [17]

Table 2.1 : Important processing parameters and resulting microstructural features for fully equiaxed microstructures [17]

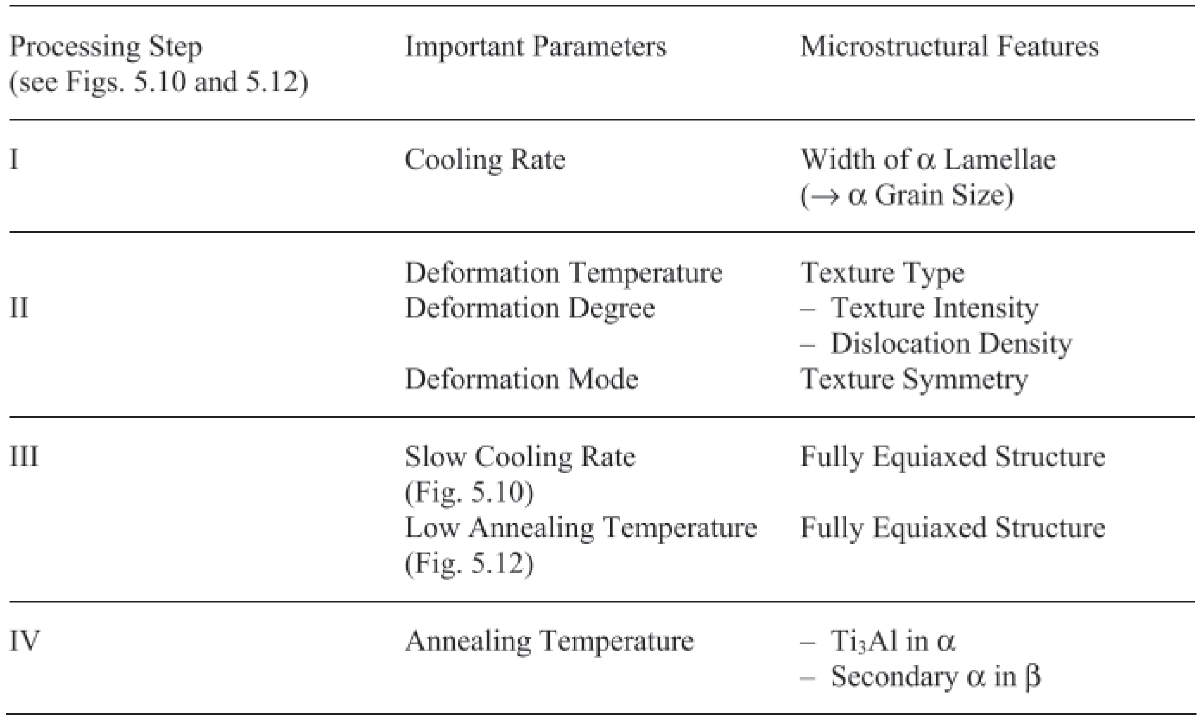

Processing Step (see Figs. 5.10 and 5.12)	Important Parameters	Microstructural Features
I	Cooling Rate	Width of α Lamellae (→ α Grain Size)
II	Deformation Temperature	Texture Type
	Deformation Degree	– Texture Intensity – Dislocation Density
	Deformation Mode	Texture Symmetry
III	Slow Cooling Rate (Fig. 5.10)	Fully Equiaxed Structure
	Low Annealing Temperature (Fig. 5.12)	Fully Equiaxed Structure
IV	Annealing Temperature	– Ti_3Al in α – Secondary α in β

2.1.3 Texture

During the deformation process of the (alpha + beta) phases, the temperature at which the process takes place can result in the development of crystallographic texture. Texture is defined as a preferential distribution of the orientation of the (0002) plane of the grains within the material relative to the processing direction [19]. Rolling is the most common processing route, and the texture is typically discussed relative to the rolling direction (RD). At low deformation temperatures, a high volume fraction of the alpha phase is present and an alpha deformation texture (called a basal/transverse) occurs. At higher deformation temperatures, a high-volume fraction of the beta phase is present and a beta deformation texture occurs. Texture refers to the crystallographic nature of the microstructure as a whole and ignores the spatial distribution of the grains with a similar orientation.

Thermomechanical processing can also induce microtexture, which differs from the overall texture of the material in that it describes the spatial clustering of grains with similar orientations. During the formation of these clusters of similarly oriented grains, the recrystallization step does not occur in the classical sense [20]. A micro textured region (MTR) refers to the clustering of α grains and transformed beta regions with similar crystallographic orientation [11], [12], [21], [22]. An example of a microtextured material with MTRs is in Figure 2.5. The deformation of beta grains during the second strep produces a texture, and the alpha plates that form upon cooling retain some aspects of this texture during the cooling process due to the burgers orientation relationship [23]. The clusters of similarly oriented grains are a result of large initial beta colony structures which form primary alpha grains with a similar orientation during the second deformation processing stage, as the number of deformation modes available to the hexagonal alpha phase is limited [21].

There have been few attempts to quantitatively characterize microtexture. One notable exception is the work of Woodfield et al. [11], [12], who segmented MTRs from EBSD data using a 20° misorientation angle between adjacent pixels. The authors developed a regression model that related characteristics of MTRs and the primary alpha grains to dwell fatigue capability. The model proposed accounted for the volume fraction and size of MTRs (called the *primary alpha colony fraction* in the original paper) as well as the size and volume fraction of and degree of crystallographic alignment of the individual primary alpha particles within the MTRs. These results were used to predict fatigue lifetime as a function of microstructure for a wide range of thermomechanical processes [11]. A later formulation by Pilchak et al. [24] extended this method to group grains based on c-axis misorientation and permitted grouping of non-contiguous grains into MTRs. The size and shapes of the MTRs obtained by these segmentation algorithms agree well with the size and shapes of the faceted initiation sites on fracture surfaces of failed dwell fatigue specimens[10], [13].

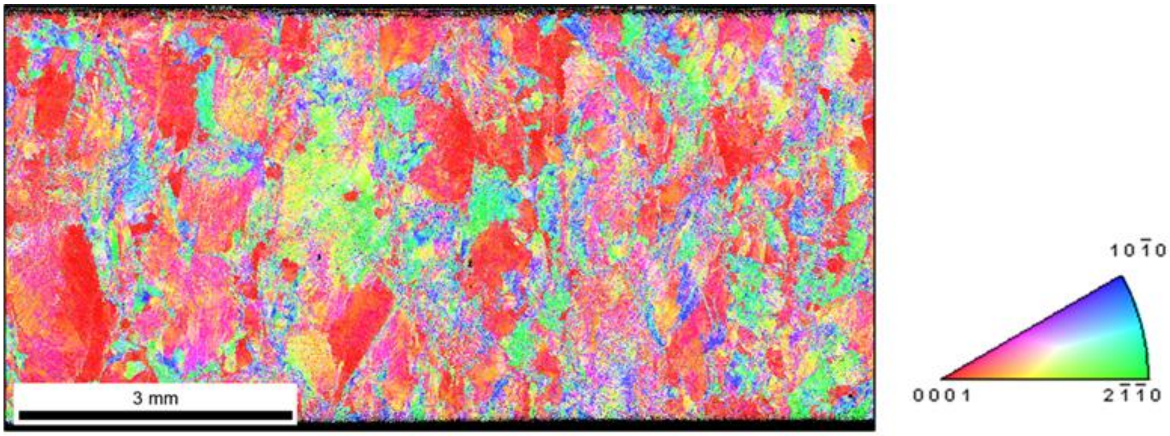

Figure 2.5: Example of previous beta-annealed and hot rolled Ti-6242 exhibiting MTRs. The average grain size is 10 µm and MTR sizes range from 1-3 mm.

2.2 Mechanical Properties of Near-alpha Titanium Alloys

Crack initiation under dwell fatigue in a near-alpha titanium alloy is a complex process that is related to the plastic and elastic anisotropy, creep behavior, strain rate sensitivity, and local microstructure. Each of these mechanisms is also known to be temperature dependent with different behavior over the range of 20°C-200°C. In the following section, each of these properties of near-alpha titanium alloys are discussed with respect to their effect on dwell crack initiation.

2.2.1 Anisotropy

As the Ti-6242 used for this study has a fully equiaxed microstructure and is considered a near-alpha alloy, its mechanical response is dictated by the anisotropy of the HCP alpha phase. The HCP structure causes an anisotropic response in the material under both elastic and plastic deformation. Since alloys with over 6% solute atoms, such as substitutional aluminum, do not undergo twinning, only the anisotropy of the modulus and planar slip activity need to be considered for our study of Ti-6242 [17], [25], [26].

2.2.2 Modulus

Both the modulus of elasticity and the shear modulus for the HCP alpha phase of titanium vary as a function of the angle between the c-axis of the grain and the loading direction. The transversely isotropic elastic response for a single crystal of pure alpha titanium between 100 GPa and 145 GPa is shown in Figure 2.6 [27]. This response occurs due to the close packing of atoms along the basal plane of the unit cell. The elastic bulk response of polycrystalline alpha titanium exhibits anisotropy due to crystallographic texture in a less dramatic way, where the intensity of the texture dictates this response. As the testing temperature increases, polycrystalline alpha titanium has an almost linear decrease of both its modulus of elasticity and shear modulus, as seen in Figure 2.7 [28].

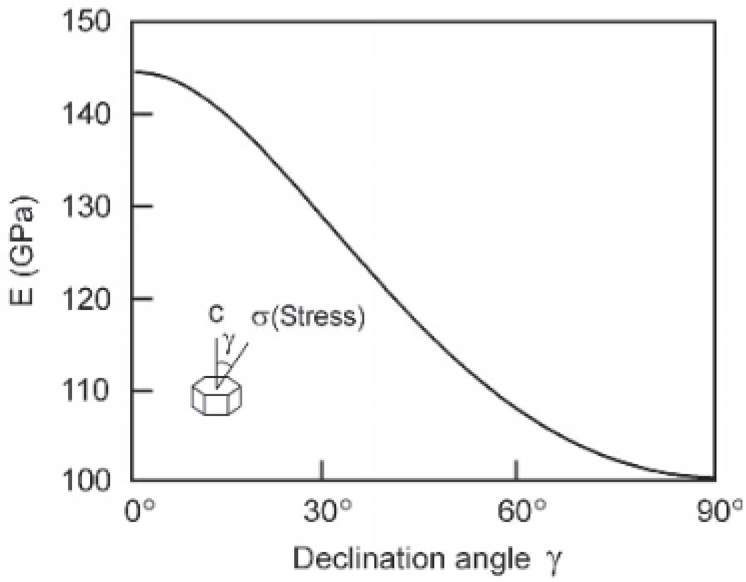

Figure 2.6: Elastic Modulus (E) of a single crystal of α Ti as a function of the declination angle (γ) relative to the loading axis misorientation [27]

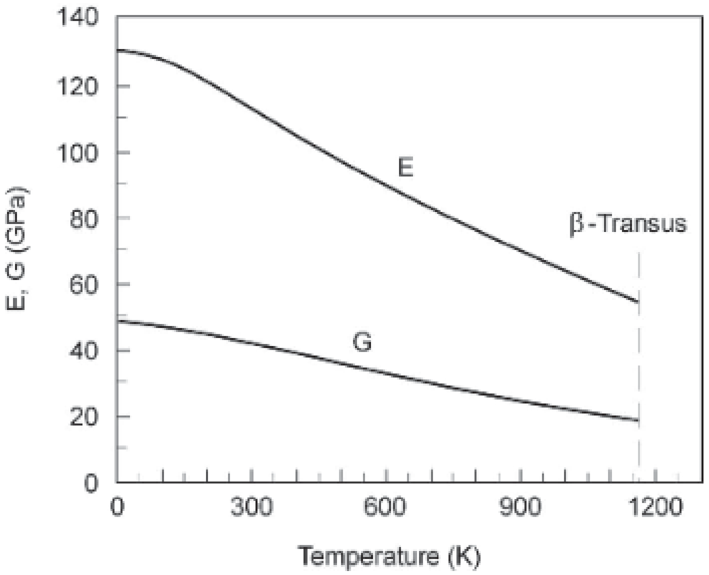

Figure 2.7: Elastic Modulus (E) and Shear Modulus (G) of α Ti polycrystals as a function of temperature [28]

2.2.3 Plastic Deformation

Since twinning is suppressed in Ti-6242 by the aluminum alloying additions, plastic deformation is accommodated by planar dislocation slip in this near-alpha titanium alloys. Slip occurs on one of the three known slip planes: basal (001), prismatic {10¯10}, and first and second order pyramidal {10-11} and {11-22} respectively, as shown in Figure 2.8. Slip directions are in the close packed <11-20> or <11-23> directions. When only considering slip in the <11-20>, there are only 4 independent slip systems [29], [30], which falls short of 5 independent slip systems required by the von Mises criterion for homogenous plastic deformation of a polycrystal. To satisfy the von Mises criterion in the absence of twinning, deformation along the c-axis with a non-basal burgers vector occurs, known as <c+a> slip or pyramidal plane slip in the <11$\bar{2}$3 > direction.

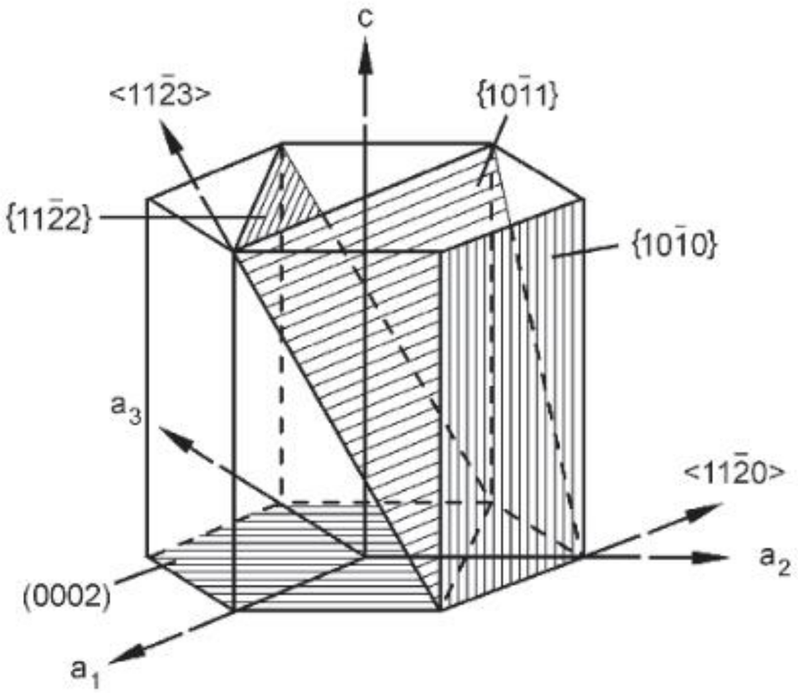

Figure 2.8: Slip planes and directions for hexagonal α phase

To activate a slip system and initiate dislocation glide, the slip system must experience a stress in excess of the critical resolved shear stress (CRSS), which is the minimum required shear stress for dislocation activity. The resolved shear stress for each individual slip system from an applied tensile stress can be calculated using Schmid's law

$$\tau_{RSS} = \sigma \times m_{schmid} \qquad (1)$$

where τ is the resolved shear stress, σ is the applied tensile stress, and m is the Schmid factor as define by

$$m_{schmid} = cos\ \kappa\ cos\ \lambda \qquad (2)$$

where κ is the angle between the slip plane normal and the applied force, and λ is the angle between the applied force and the slip direction as illustrated in Figure 2.9.

The CRSS for <c+a> slip is typically reported as being 3-5 times larger than <a> type slip in near-alpha titanium alloys, meaning that pyramidal <c+a> slip is 3-5 times more difficult to activate than basal or prismatic type slip. Despite numerous investigations, there is no consensus on the CRSS for each slip system or the ratio between the CRSS for basal, prismatic, <a> pyramidal, and <c+a> pyramidal slip in titanium alloys [4], [31]–[41]. This uncertainty is due to the difficulty in measuring the CRSS in non-cubic metals with traditional single-crystal techniques, especially since most engineering materials are two phase and therefore not available in a single crystal form for testing [42]. In Ti-6242, micropillar compression, crystal plasticity modeling, and slip activation during in-situ tensile testing have all produced conflicting CRSS results [4], [7], [14], [25], [38], [41]–[45]. There is even debate on whether basal slip or prismatic slip is more easily activated [44], [46], [47]. For the sake of simplicity, the results from a single crystal model material is presented for discussion. The CRSS values from this single crystal study are used in most of the state-of-the-art models for load shedding and crack initiation in Ti alloys [14], [15], [48]. It is hypothesized that the temperature relationships demonstrated apply to the slip systems regardless of what their actual CRSS values are [15]. The CRSS required for each type of slip in a model Ti-Al alloy, Ti-7Al is shown in Figure 2.10 from a study by Hasija et al. [7] and fitted by Ozturk et al. [14]. With an increase in temperature, the CRSS for all slip systems decreases. Between ~300 K and 570 K, the rate of decrease for the CRSS for the pyramidal slip system is significantly larger than for the basal and prismatic systems. Therefore, with increasing temperature, the material becomes less anisotropic relative to its active slip system.

Table 2.2: Slip Systems in α Ti

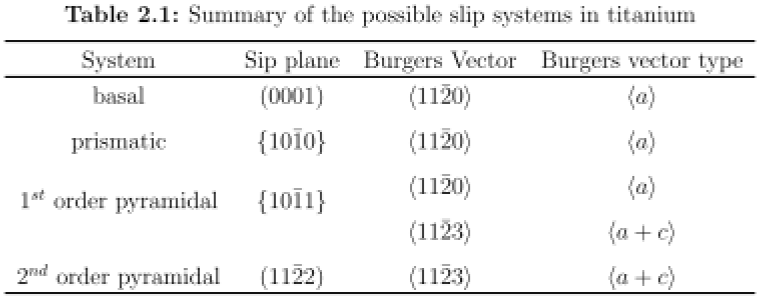

Table 2.1: Summary of the possible slip systems in titanium

System	Sip plane	Burgers Vector	Burgers vector type
basal	(0001)	$\langle 11\bar{2}0\rangle$	$\langle a\rangle$
prismatic	$\{10\bar{1}0\}$	$\langle 11\bar{2}0\rangle$	$\langle a\rangle$
1^{st} order pyramidal	$\{10\bar{1}1\}$	$\langle 11\bar{2}0\rangle$	$\langle a\rangle$
		$\langle 11\bar{2}3\rangle$	$\langle a+c\rangle$
2^{nd} order pyramidal	$(11\bar{2}2)$	$\langle 11\bar{2}3\rangle$	$\langle a+c\rangle$

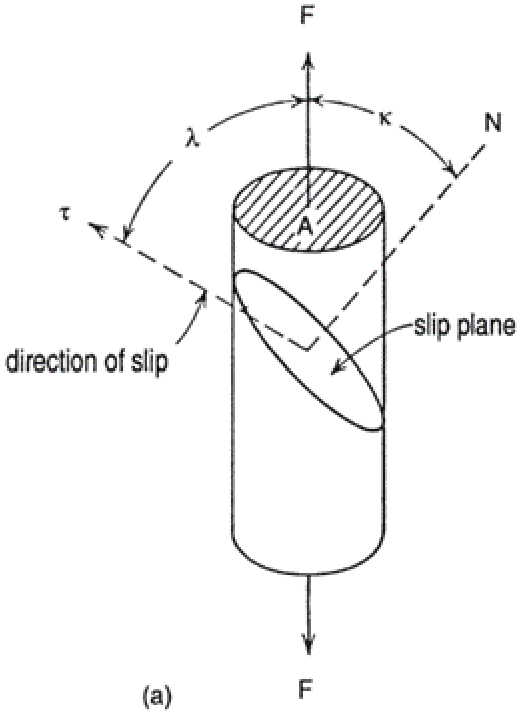

Figure 2.9: Example of a cylindrical specimen with an identified slip system for Schmid factor illustration [49]

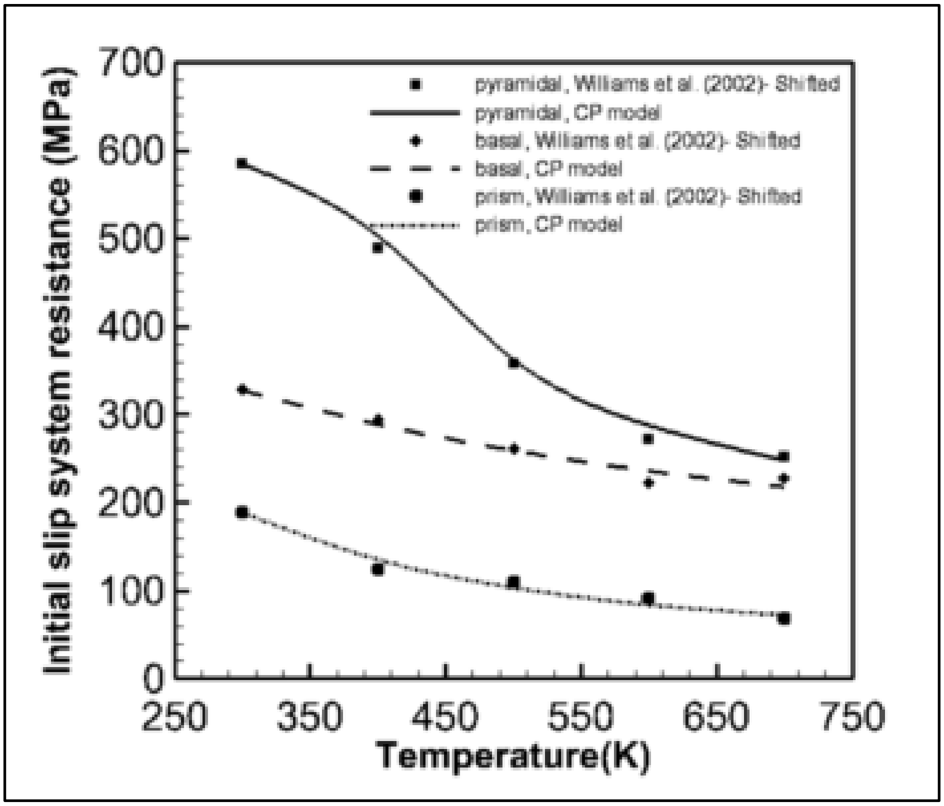

Figure 2.10: CRSS relative to temperature for Ti-7Al [7], [14]. With increasing temperature, the CRSS for all slip systems decreases. From ~270-550 K, the CRSS for pyramidal slip falls at a greater rate than the CRSS for basal and prismatic slip. Above 650 K, there is not a significant difference between the CRSS for basal, prismatic, and pyramidal slip, implying a reduction in anisotropy.

2.2.4 Creep

While creep is typically only considered a significant deformation mechanism at temperatures above half of the materials melting temperature, titanium alloys are known to experience room temperature creep at less than 0.25 its melting temperature [50], [51].

Slip on the easy to activate basal and pyramidal planes dominates the cold creep phenomenon rather than a diffusion type process as seen in other alloys at higher temperatures. The hypothesis in the scientific community is that creep deformation first occurs in grains well oriented for basal and prismatic slip, and then activates in the less favorably oriented grains with time. This phenomenon with relation to the present study is discussed at length in the following section on dwell fatigue and load shedding. The early onset and subsequent exhaustion of easy to activate slip is believed to be the cause of the material's high initial transient deformation rate which steadily decreases with time, as shown in Figure 2.11. This creep rate phenomenon has been supported by both crystal plasticity[43], [46], [52] and cellular automata models [53].

Work from Neeraj and Mills [54] used a strain-rate-sensitive Holloman flow equation to model the creep strain and determined that at room temperature Ti-6242 had a strain rate sensitivity comparable to other common materials. They instead attributed the room temperature creep and non-exhaustive transient creep behavior in Ti alloys to their low strain hardening exponents. On a microstructural level, they conclude that primary creep occurs due to the highly planar slip in the alpha phase caused by short-range ordering (SRO) of the Ti and Al atoms.

The microstructural dependence of creep behavior of Ti-6242 and Ti-6-4 was studied by Brandes et al. [55]. They found that plastic strain accumulation during creep occurred more rapidly in weaker microstructures with lower strain hardening and higher strain rate sensitivities. Additionally, a reduction in the α-lathe thickness in conjunction with thick β-ribs between the lathes and secondary α content had the highest strength and creep resistance. The strengthening from the secondary alpha is sensitive to morphology. The microstructures with long, thin α-precipitates within the β-ribs were less likely to undergo creep than microstructures that contained fine, short α-precipitates within the β-ribs. [55]

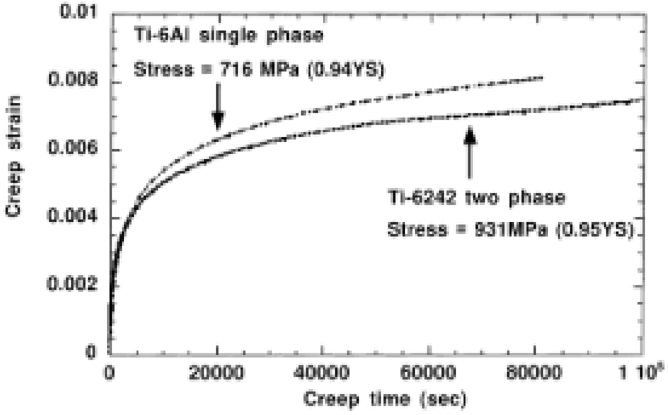

Figure 2.11: Creep rate of Ti-6242 [54]

2.3 Dwell Fatigue in Near-alpha Titanium Alloys

Before the 1970s the main consideration of room temperature creep of alpha titanium was for the dimensional stability of components under high stress. However, in 1972 the first documented instance of dwell fatigue failure occurred when two near-alpha titanium fan discs in Rolls-Royce engines ruptured unexpectedly early compared to their predicted low cycle fatigue (LCF) lifetimes. The discs of IMI 685 entered service after passing all pre-service screening [6], [56]. The final report on these premature failures were attributed to the phenomenon of dwell fatigue [57]. Dwell fatigue has continued to be an active area of study over the past fifty years, with the room temperature creep and stress redistribution of titanium alloys as the focus of this unexplained phenomenon [5], [8], [58].

Dwell fatigue fundamentally deviates from low cycle fatigue, in that at the top of each loading cycle the peak stress is held, creating a trapezoidal waveform as seen in Figure 2.12. The hold more accurately models the sustained peak stress that components experience during take-off, when the engine is initially cold and then running at max power to reach the cruising altitude. To a lesser extent, it can also model the engine cruise, but this is not the most damaging loading domain of the flight relative to dwell. Each flight cycle dramatically reduces the lifetime of near-alpha titanium alloy turbine disks when compared to the lifetime predicted by standard cyclic fatigue loading calculations. This reduction in lifetime is termed the *dwell debit*. In Ti-6242, the dwell debit is commonly ten to twenty times below the lifetime predicted by low cycle fatigue calculations. It has been shown that near-alpha Ti alloys such as Ti-6242 experience a significant dwell debit, while alpha + beta alloys with a higher volume fraction of beta, such as Ti-6-4 and Ti-6246, are significantly less dwell susceptible [17], [59]**.** All titanium alloys exhibit a small dwell debit of two to three times, but when this debit is greater than ten times, the parts fail catastrophically and unexpectedly. This fatigue damage accumulated in the alpha phase [45], [60]–[63], which is softer than the precipitation strengthened beta phase. In these near-alpha titanium alloys, a phenomenon known as load shedding in the alpha grains and MTRs is hypothesized to be the cause of this damage accumulation and lifetime reduction.

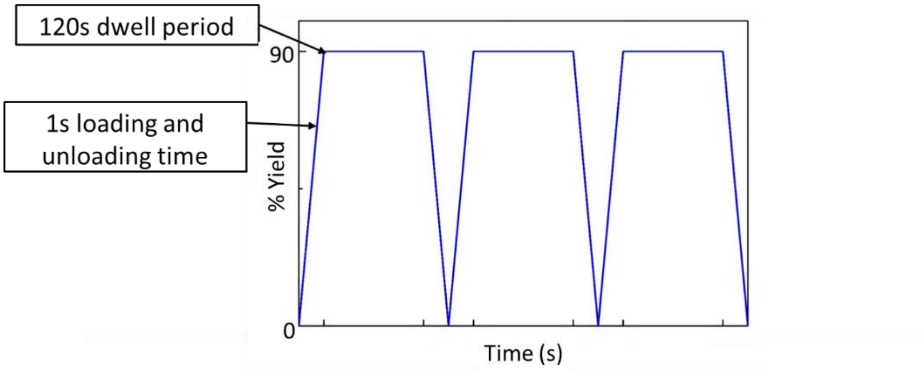

Figure 2.12: Representative dwell fatigue wave form

2.3.1 Load Shedding

Load shedding stems from crystallographic anisotropy, where favorably oriented grains undergo plastic deformation, which forces neighboring elastically deforming grains to carry a higher stress. In Ti-6242, the orientation of the c-axis of the alpha grains relative to the loading direction produces a distinct elastic modulus in each grain. In the dwell fatigue literature, grains with their c-axis near parallel to the loading direction are termed “hard grains,” whereas grains with their c-axis near perpendicular to the loading direction are termed “soft grains.” Hard grains are well oriented for pyramidal slip, whereas soft grains are well oriented for basal, prismatic, or basal and prismatic slip. The critical resolved shear stress (CRSS) required to activate pyramidal slip is at least three times greater than the CRSS for basal and prismatic slip [4]. This difference in CRSS implies that hard grains remain resistant to plastic deformation while dislocation slip can remain active in the soft grains. When this occurs, the interaction between the hard and soft grains was first described by a modified Stroh model [5]. According to the model, macroscopically applied loads can cause slip to occur in the soft grains, where dislocations move through the soft grain until they meet the hard grain boundary. The dislocations then pile up at this hard-soft interface and create a significant stress riser, as shown in Figure 2.13. The stress relaxation of the soft grain requires the hard grain to carry a higher load, and therefore the soft grain has shed its load onto the hard grain [7]–[9]. The hard and soft grain adjacent to each other during load shedding are termed a *rouge pair*. The soft grain described here is typically modeled as a grain well oriented for prismatic slip, with its c-axis near perpendicular to the load direction. This is because in many cases, prismatic <a> slip is considered the most easily activated slip system in the α phase of most titanium alloys. As mentioned in section 2.2.3, there is much debate over the actual CRSS for each slip system, relative ratios, and whether basal or prismatic slip is more easily activated. Experimental work from Bantounas on Ti-6Al-4V and Sinha on Ti-6242 supports this pile up model for crack initiation [9], [64]. This region of highly localized stress creates a favorable location for crack nucleation and faceting, limiting the lifetime of the component [7]. The initiation site is characterized by a subsurface faceted crack initiation with a physical orientation near 45° to the loading direction within a few degrees of the basal $(0002)_\alpha$ orientation [13].

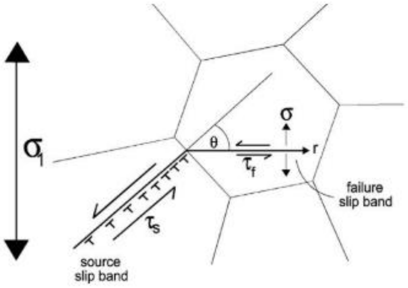

Figure 2.13: Modified Stroh model adopted by Evans and Bache to describe dwell crack initiation [5], [17]

Experimental work by Brandes et al. [59] expanded the definition of a hard-soft pair relative to the modified Stroh model for crack initiation. By examining fracture surfaces of Ti-7Al dwell fatigue samples, faceted initiation sites and extensive grain pile up were observed to occur between grains that would be traditionally defined as soft-soft pairs in the absence of traditional-hard-soft pairs [59]. While both grains in these pairs were independently well oriented for basal and/or prismatic slip, the grains themselves were not well oriented relative to each other for slip transfer between grains, which resulted in a pile up at the interface. The orientations of grains that experience dislocation pile up between them are illustrated in Figure 2.14. Samples that experience this soft-soft initiation, were textured via extrusion to exclude traditional hard grain orientations. This work highlights the importance of neighborhood effects and slip transfer as the primary consideration for crack initiation and the modified Stroh model rather than a simple “hard-soft” pair.

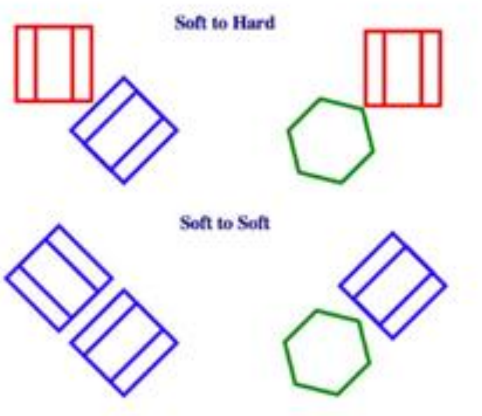

Figure 2.14: Examples of grain pairs that are capable of producing basal place facets in titanium alloys according to Brandes et al.[59]

While the modified Stroh model by Evans and Bache accounts for the necessary but not sufficient requirement related to crystallographic orientation, shortcomings of the model include that it does not account for the dwell effect of the time dependence of the load shedding phenomenon [6], [65]. In recent years, more complex crystal plasticity finite element models (CPFEM) and discrete dislocation plasticity (DDP) models have been developed to describe the load shedding phenomenon, but they are still based on the idea of dislocation pile ups.

Hasija et al. and Deka et al. developed rate dependent CPFE models that investigate the effect of time-dependent slip and stress relaxation in the soft grains that produce stress concentrations in the hard grains due to the compatibility requirement [7], [46]. They found that the time-dependent local creep and stress redistribution increases incrementally with each dwell cycle.

Venkatramani et al. expanded on this time dependent model to investigate the size-dependence of the hard and soft features [43], [52]. Their model incorporated the effects of the microstructure, grain size, colony size. Their model predicted that the stress concentration that occurred on the hard grain increased in the presence of (1) large soft regions and (2) high fractions of alpha-phase material in a two-phase titanium alloy. Those two features led to a larger amount of plastic strain in the soft regions, which in turn created a larger stress concentration in the hard grain.

Further progress with this framework was performed by Anahid et al. [66], [67] to create a microstructurally dependent crack nucleation model that would predict the number of cycles and microstructural location of crack nucleation. The model relied on the development of stress in the hard grain and the accumulation of slip and dislocation activity in the soft grain. This was later developed into a hierarchical model of nucleation, which accounts for microstructure, grain size, crystal orientation, and microtexture [68], [69].

The foundational CPFE dwell fatigue crack nucleation model from Anahid was further developed by Ozturk to investigate the effects of temperature and microstructure on dwell fatigue crack nucleation [14]. By comparing models run with cyclic loading and dwell fatigue loading, they found that MTRs accumulate more strain and are more detrimental to the fatigue lifetime under dwell loading. They also concluded that as the dwell time is reduced and approaches the loading profile of cyclic fatigue, the number of cycles to crack nucleation increases. The temperature dependent portion of the model and associated findings are explained in section 2.3.3.

A separate rate dependent CPFE model developed originally by Dunne et al. [65], [70] investigated the grain boundary morphology and relaxation time scale during dwell loading. They utilized geometrically necessary dislocations in their model which provided a physical length scale for plasticity. In this work, they found that the test control mode significantly affected load shedding. Dwell held in strain control resulted in less load shedding and smaller stress concentrations on the hard grain that dwell cycles held in stress control. This indicates a stress dependent criterion for dwell crack nucleation.

The Dunne CPFE model was furthered by Zhang et al. who investigated the temperature dependent creep and load shedding behavior during dwell of a near alpha alloys [15]. They linked the temperature dependence of the dwell debit to the strain rate sensitivity and stress relaxation of α titanium, which is discussed more in section 2.3.3. The rate sensitivity was further investigated by Zheng et al. [71] with a rate sensitive DDP model which allowed for the thermal dislocation escape from obstacles, further discussed in section 2.3.3. The CPFE model from Zhang et al. was subsequently updated to include alternative loading stress states and the results from the DPP model by Zheng et al. [71] The models from Dunne et al. [65], [70], Zhang et al. [15], and Zheng et al. [71] all focus on the time-dependent and temperature dependent strain rate sensitivity as the primary driving force for dwell fatigue crack nucleation.

The load shedding phenomenon and dwell debit are influenced by several factors, including hold time, ambient temperature, rate sensitivity, test control mode, local microstructure. Each of these factors will be discussed briefly in this background, but the bulk of this thesis will focus on the mechanisms related to local microstructure and ambient temperature.

2.3.2 Hold Time

Dwell fatigue is characterized by a hold at peak stress, and the duration of that hold influences dwell debit. An early study of the dwell debit by Evans and Gostelow confirmed that a 600 second hold at peak stress imposed a significant dwell debit [72]. Systematic research by Bache et al. demonstrated an increased strain accumulation and subsequent increase in dwell debit for holds up to 600 seconds [5]. In this study and in the dwell community at large, a dwell time of 120 s is used. Previous studies show that the dwell debit increases up to 120 s and that only a minimal increase in dwell debit occurs past that point [17]. When comparing static loading conditions to dwell fatigue, dwell fatigue experiments accumulate a greater amount of plastic strain at the same peak stress [6], [58], [73], [74]. The critical hold time that would maximize the dwell debit is believed to be somewhere in the 2-5 minute range [6], [74], [75]. As dwell experiments are time consuming and costly, and the creep mechanism should be the same within that time range (i.e. a single dwell test to 10,000 cycles with a 600 second hold and 1 second loading unloading would take almost 70 days of continuous running), the 2 minute hold has become the industry standard for lab experiments [6], [17].

2.3.3 Thermal Dependence

The mechanisms behind load shedding are temperature dependent. The most significant dwell debit for Ti-6242 has been observed at approximately 120°C, with dwell sensitivity essentially disappearing at temperatures above nominally 200°C [15], [76]. However, there are different hypotheses under investigation for how this occurs. Two current theories on the role of temperature in load shedding are as follows:

(1) The thermal dependence of load shedding is due to the decrease in the difference in strengths of different grain orientations with increasing temperature, as determined through Crystal Plasticity Finite Element (CPFE) modeling [14]. At 120°C, the CRSS required to activate pyramidal slip is more than two times greater than CRSS for prismatic and basal slip [25]. As the temperature rises, the CRSS required for pyramidal slip decreases to match the CRSS required for basal and prismatic slip [25]. The strength mismatch between the hard and soft grains thereby diminishes, quickly redistributing the stress and allowing dislocations to traverse through the hard grain rather than collect at the boundary. It is further hypothesized that this drop in CRSS results in a more homogeneous deformation at the microscale, but this has not been thoroughly validated [7]. One shortcoming of this model is that it does not predict that the peak dwell sensitivity occurs at 120°C, as is known

empirically. Rather the dwell debit is worse at room temperature, and then decreases with increasing temperature.

(2) The second model identifies the effect of the temperature dependence of strain rate sensitivity in addition to the change of slip strength as the primary mechanisms for load shedding [15], [77]. During the loading cycle, dislocations are pinned at obstacles, and time-dependent thermally activated dislocation escape allows the dislocations to continue moving through the material. At 120°C in Ti-6242, the time constant associated with the activation energy required for dislocation escape is comparable to the dwell hold time. This allows for significant load shedding to occur, since the dislocations overcome their obstacle during the dwell period which allows more dislocations to nucleate and form extended pile up structures at the hard-soft boundary. At 200°C, the pinned dislocations escape so rapidly prior to the stress hold that the material reaches an equilibrium state before the dwell period, and no load shedding occurs. If the temperature is too low or the activation energy too high relative to the hold time, an additional case is proposed where load shedding is absent as the dislocations are completely unable to escape their obstacles [77], [78]. It is further shown that this strain rate sensitivity also depends upon crystallographic orientation, wherein the sensitivities of the basal and prismatic slip systems were shown to be very different in Ti-6242 through single crystal pillar compression experiments and micro-tensile experiments [15], [78], [79].

The exact mechanisms behind load shedding and the associated dwell debit have yet to be fully understood or rigorously tested. The second model fundamentally deviates from the first, as it accounts for a thermally activated obstacle escape in addition to the temperature dependence of the material anisotropy. Both models predict a temperature dependent accumulation and redistribution of stress and strain in individual grains and MTRs during each dwell load cycle, a thermal phenomenon that has yet to be experimentally observed.

2.3.4 Stain Rate Sensitivity

The strain rate sensitivity of near-alpha titanium alloys is believed to be the cause of load shedding and high basal stress necessary for crack nucleation [67], [80], [81]. Fundamentally the strain rate sensitivity relates the flow stress and strain rate assuming a constant strain rate and temperature [78]. Since dwell fatigue is a time sensitive deformation phenomenon, as seen in previous studies of the hold time [6], [74], [75], it is important to consider the rate sensitive properties of the material [47], [58]. The anisotropy of the elastic and plastic response of the material imply that the strain rate sensitivity exhibits anisotropy relative to grain orientation relative to loading and corresponding slip systems [78]. Therefore the time dependent stress amplification as a result of material strain rate sensitivity should play a role in the load shedding and early crack nucleation of dwell fatigue near-alpha titanium alloys [82].

Experimental work by Chichili et al. [83] studied the bulk room temperature strain rate sensitivity of alpha-titanium alloys over the strain rate range of 10^{-5} to 10^{5} s^{-1}. Their results indicate that with increasing strain rate, the flow stress increases, and the alloy exhibits a significant increase in strain rate sensitivity. They concluded that plastic deformation is primarily accommodated by dislocation slip at both low and high strain rates, and that the rate of dislocation accumulation and density increased with increasing strain rate. Additionally, with increasing strain rate, they observed a greater number of twin nucleation sites, but plastic deformation was still predominantly accommodated by dislocations.

These anisotropic rate sensitive mechanisms can influence the dislocation pile up behavior thought to underpin load shedding. This was evidenced in nanoindentation work by Jun et al. which investigated the localized strain rate sensitivity of individual alpha-particle orientations by quasi-static pillar compression experiments at different strain rates [78]. Specifically, they observed that the strain rate sensitivity of prism slip is 2-3 times higher than the rate sensitivity for basal slip. The basal oriented grains were more resistant to dislocation motion and exhibited more complicated dislocation interactions, which created more slip localization and a higher hardening gradient.

Discrete Dislocation Plasticity (DDP) modeling by Zheng et al. has been used to understand mechanistic behavior for this room temperature strain rate sensitivity [71], [84]. Traditional DDP models only include rate sensitivity contributions from dislocation nucleation and mobility, both of which are typically only active at large strain rates and temperatures. In most materials, it is hypothesized that the increase in plastic flow stress with an increase in strain rates is due to a transition from thermal dislocation activation events at low strain rates to the viscous drag of dislocations at high strain rates [85]. Modeling work by Zheng et al. that incorporated the activation energy for self-diffusion into a DDP model for α Titanium alloys produced a strain rate sensitivity response that matches experimental strain rate sensitivities at low temperature [47], [71]. The addition of the thermally activated dislocation motion at room temperature explains the associated strain rate sensitivity in near-alpha titanium alloys.

2.3.5 Test Control Mode

For the loading curve, it is important to note that a stress-controlled hold is more damaging than a strain-controlled hold. Crystal Plasticity Finite Element (CPFE) Modeling by Zhang et al. [15] utilized the strain rate sensitivity, creep, and stress relaxation of individual grains. They found that under strain-controlled loading, local rate-dependent slip accumulation does not occur. The stress on each grain remains the same and very little stress relaxation occurs in the soft grain, so no load shedding occurs. In strain-controlled testing, the material experiences an overall reduction in stress over the dwell period and no stress accommodation is necessary. During a stress-controlled test, the soft grain in a rouge pair experiences significant creep via rate-dependent slip accumulation and load shedding from the soft to the hard grain occurs. The experiments in this thesis are performed under load-control to induce and study load shedding and its sensitivity to temperature and local microstructure.

2.3.6 MTR Dependence

The effects of microstructure are an important yet little understood parameter for dwell fatigue and associated lifetimes. A significant amount of excellent work has been done to study this effect but with such complex materials with limited test volumes, it is difficult to isolate the exact conditions which lead to early failure. Dwell sensitivity and load shedding depend on the local microstructure, specifically the presence of microtextured regions (MTRs). Microtexture refers to the clustering of α grains and transformed beta regions with similar crystallographic orientation. The key attributes of MTRs important to dwell fatigue include the volume fraction, the size, and the orientation spread of the aligned grains. These attributes may be grouped together and collectively referred to as the “intensity” of the MTRs, which enables a single parameter characterization that can be used for volumetric statistical extrapolation [10]. Microtexture is believed to assist in the formation of fatigue cracks [8], [43]. Globally, MTRs are believed to define the “effective structural unit” size, implying that the interfaces between these regions is the upper bound of the slip length due to the ease of slip transmission between grains with similar orientation [9], [43], [86]–[91]. It has been postulated that load shedding is dictated by the evolution of the plastic strain within the soft grain or MTR [43]. As the size of the soft region increases, there are more potential locations for long-range slip to occur, producing a greater number of dislocations in the pileup, a stronger stress concentration at the boundary with the hard grain, and a greater load-shedding effect [8], [43]. MTRs can potentially produce especially large load shedding effects due to their size, as processing can produce MTRs many orders of magnitude greater than the individual grain size [8].

2.3.7 Dwell Fatigue Fracture Surfaces

During dwell fatigue of near alpha titanium alloys, dislocation pile ups result in crack nucleation, typically in one alpha grain. If suitably oriented grains are present, the cracks will continue to grow faceted planes on the fracture surface that are visually similar to cleavage like fracture, as shown in Figure 2.15. These formation facets generally occur in subsurface grains within the bulk of the material that have their c-axis near-perpendicular to the loading direction, when loaded below the macroscopic yield strength [5], [62], [72]. Grain orientation studies performed on dwelled titanium fracture surfaces indicate that the grains involved in the initiation site fracture on a plane approximately 10° from its basal slip plane [9]. While these sites are visually similar to brittle fracture, TEM analysis on the facets regions of dwelled fracture surfaces show significant <c+a> slip, and the samples strain accumulation indicated significant plastic deformation [63].

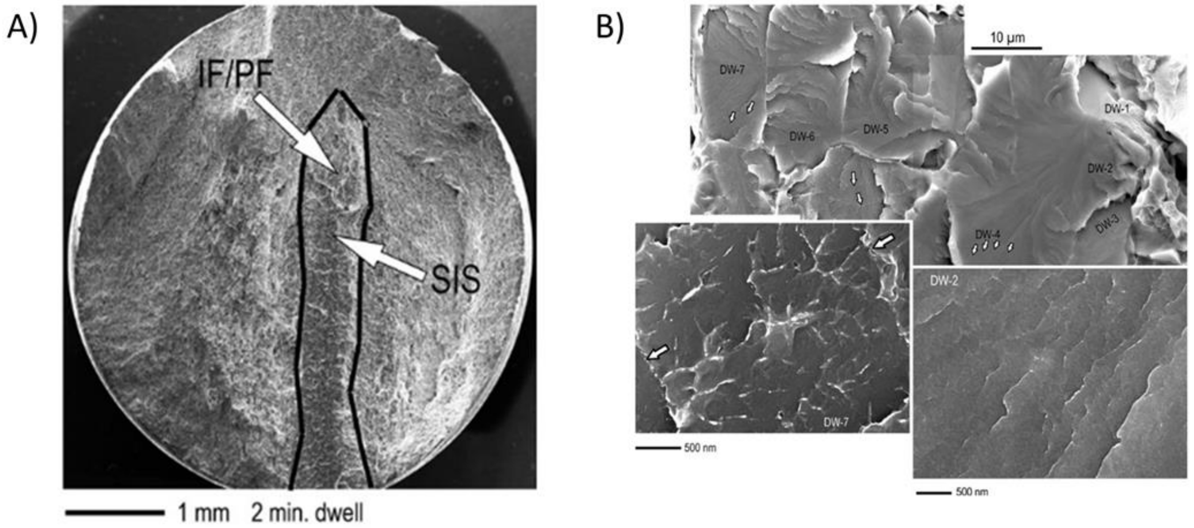

Figure 2.15: Faceted fracture surface of a dwelled sample of near-alpha titanium alloy, Ti-8Al-1Mo-1V, loaded with 2 minute peak holds with a peak stress of 95% of the macroscopic yield strength. **(A)** Low magnification SEM image of the fracture surface. The faceted region is enclosed with the black line, and the initiation facet, propagation facets and secondary initiation site are labeled by IF, PF, and SIS respectively. **(B)** High resolution SEM image of the initiation facet (DW-1) and the propagation facets (DW-2 through DW-7). The initiation facet is included substantially relative to the loading direction and propagation facets.[62]

Chapter 3 Methodology

Forged and hot-rolled Ti-6242 plates of ~11.5 mm thickness provided by AFRL were processed to produce large MTRs on the order of 1-3 mm. 50mm x 50mm x 50mm plates were cut from a beta annealed billet and hot rolled at 1500°F at 10% reduction in thickness per pass to a total reduction of approximately 75% reduction. The final reduced plates were heat treated at 1750°F for 2 hours and furnace cooled. Fatigue specimens were electrodischarge machined from the plates into flat pin loaded dogbone-shaped samples with dimensions of 50mm x 10mm x 1mm, with a gauge cross section of 1mm x 3mm and length of 6 mm. The schematic for the pin loaded dog bones is seen in Figure 3.1.

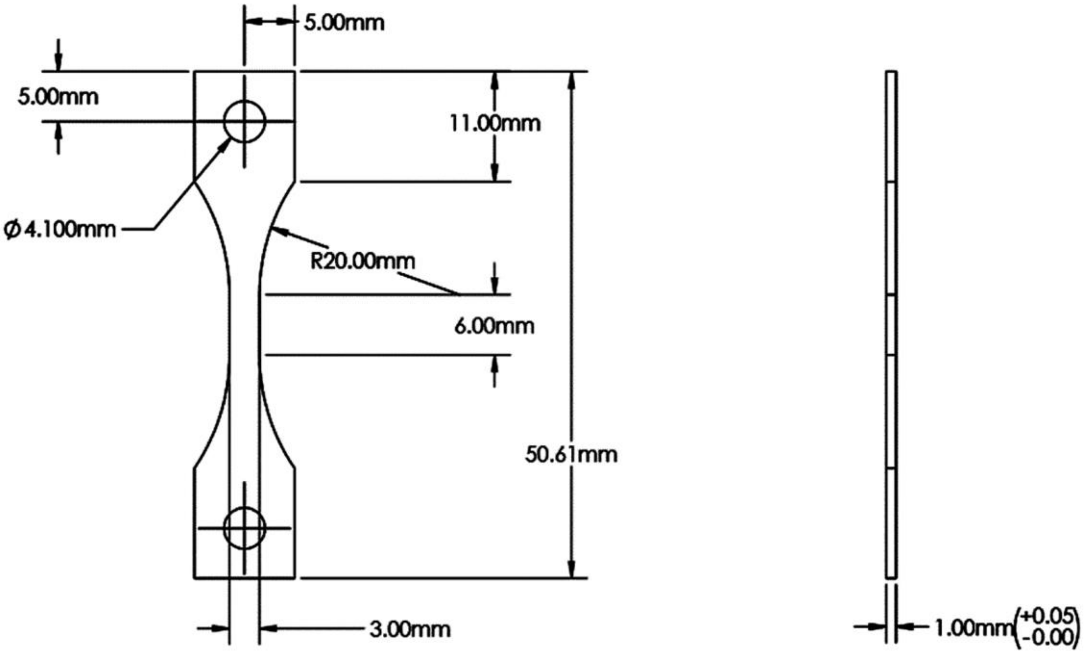

Figure 3.1: Schematic of pin loaded dwell fatigue dogbone with overall dimensions of 50mm x 10mm x 1mm and a gauge cross section of 1mm x 3mm and length of 6mm

Five samples were then mechanically ground at 240, 400, 600, and 800 grit with a final polishing to a mirror finish using a 1:4 30% hydrogen peroxide solution: MasterMet 2 Colloidal mixture. The areas of interest (AOI) were defined in the center of each sample gage (Three samples with a large 4 mm x 2.5 mm AOI and two samples with a small 500 µm x 500 µm AOI) by placing 15 µm x 7 µm and 500 nm thick fiducial markers by platinum vapor deposition at the four corners of the region. Electron backscatter diffraction (EBSD) maps were collected over the region of interest for each sample with a step size of 2 um per pixel for the large AOI and a step size of 0.5 µm per pixel for the small AOI using an EDAX/TSL Hikari EBSD camera. The inverse pole figure map relative to the loading direction of each sample is shown in Figure 3.2 and Figure 3.3. A moderate [0 0 0 1] texture relative to the loading direction was observed for each specimen, as shown in the pole figures.

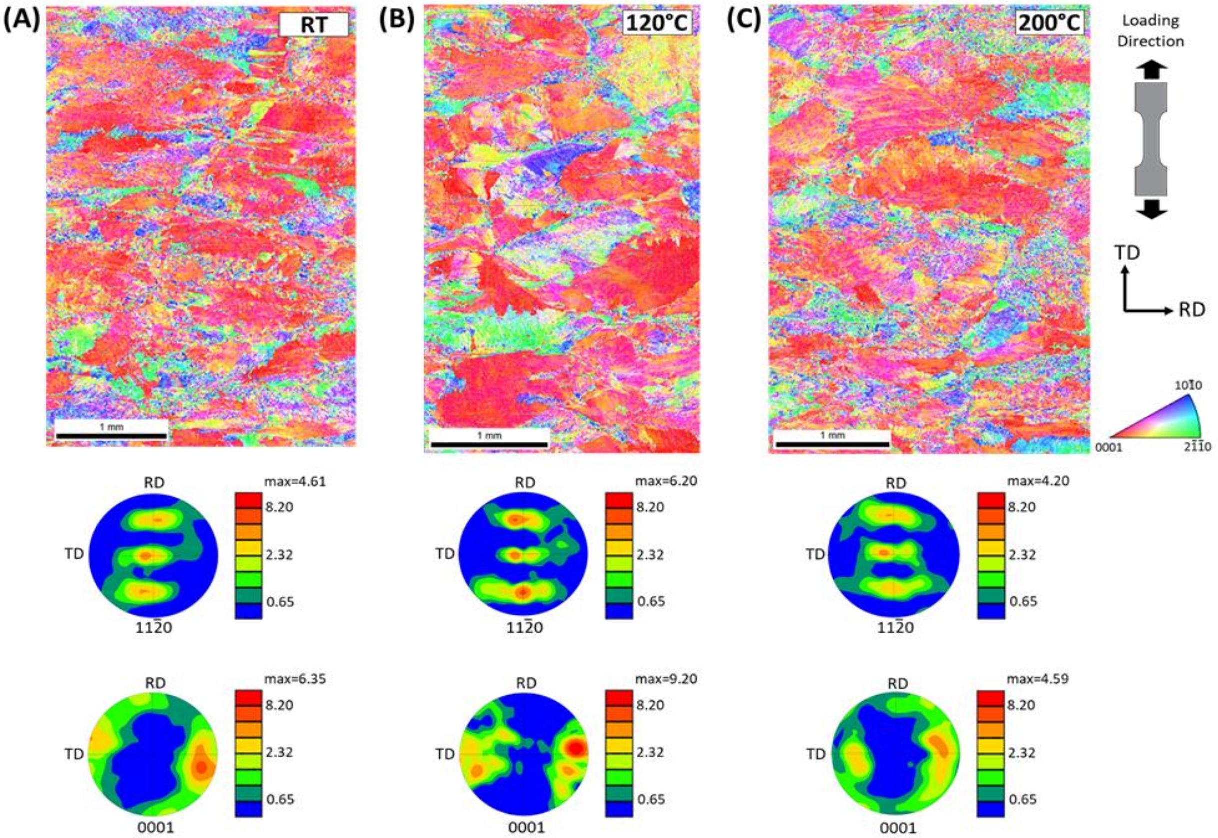

Figure 3.2: (Top) EBSD data and (Bottom) pole figures showing large MTRs on the length scale of 1-3mm and a moderate 0001 texture relative to the loading direction for **(A)** Sample A (RT), **(B)** Sample B (120°C), and **(C)** Sample C (200°C)

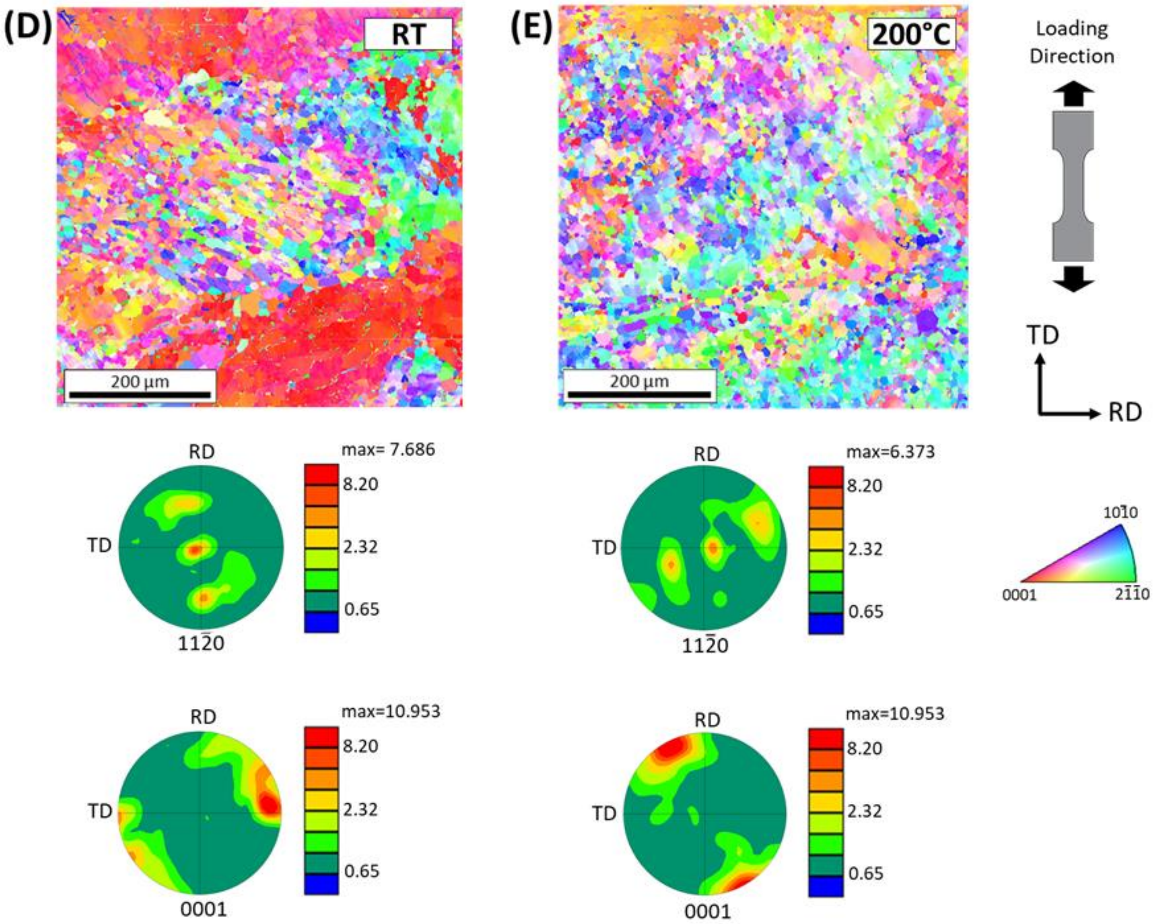

Figure 3.3: (Top) EBSD data and (Bottom) pole figures showing a moderate 0001 texture relative to the loading direction for **(D)** Sample D (RT) and **(E)** Sample E (200°C)

After EBSD, a random speckle pattern was applied to the specimen surface for SEM-DIC, in which Digital Image Correlation (DIC) is performed inside a scanning electron microscope (SEM) to characterize full-field microscale surface deformations. DIC is a full-field, length scale independent, surface displacement measurement technique. As the specimen undergoes deformation, images are taken of the surface, and the relative displacements of the random speckle pattern features are used to calculate a full-field surface displacement map, from which the surface strains can be calculated. High resolution images were captured in-SEM and stitched together to investigate strain localization and deformation at the microstructural length scale across mm-scale fields of view [92]–[94]; for example, Specimen A in Table I had a 4 mm x 2.5mm field of view (FOV) collected by stitching a 14 x 22 array of individual 250 µm x 250 µm SEM images. An external scan control of the electron beam was implemented to minimize the spatial and temporal image distortions that can result from rastering of the electron beam during SEM image collection [95], [96]. The random speckle pattern was applied following the method of Montgomery et al. [97], in which the specimen surface was sputtered with a 3 nm passivating layer of titanium followed by a 17 nm thick layer of silver in a sputter deposition system (AJA ATC 1800) equipped with 2-inch diameter sputter sources. Each sample was subsequently soaked for ~1.75 hour in a solution of 1 wt. % NaCl in distilled water to reconfigure the silver layer into a pattern of approximately 200 nm speckles. The imaging and testing parameters of each specimen are shown in Table 3.1.

Table 3.1: Test temperature, loading, and image conditions for each sample

	Test Temperature	Macroscopic Yield Strength	Tile Size	Number of Tiles	Total Imaged Area
Sample A	Room Temperature	905 MPa	300 µm	18 x 11 tiles	4 mm x 2.5 mm
Sample B	120°C	824 MPa	250 µm	22x14 tiles	4 mm x 2.5 mm
Sample C	200°C	647 MPa	250 µm	22 x 14 tiles	4 mm x 2.5 mm
Sample D	Room Temperature	905 MPa	60 µm	11 x 11 tiles	500 µm x 500 µm
Sample E	200°C	647 MPa	60 µm	11 x 11 tiles	500 µm x 500 µm

Mechanical testing was performed at room temperature (RT), 120°C, and 200°C, as shown in Table 3.1. These temperatures were selected to represent the following cases: (1) a dwell sensitive temperature (RT); (2) the largest dwell debit typically observed in industry (120°C); and (3) no dwell debit typically observed (200°C) [15], [76]. Dwell fatigue loading is defined by a trapezoidal waveform with a 120 second load hold at the 90% of macroscopic yield with a one second load/unload. The yield strength at each of these three temperatures was determined by performing displacement-controlled uniaxial tension tests to failure in an 810 MTS test machine. The samples were pin loaded and heated using two 500 Watt induction heaters (Tempco model CRR30015), and the temperature was monitored and maintained to ±2°C with a glass fiber ratio pyrometer (model Micro-Epsilon CTRM series) and a PID controller (model Omega CN8200 series). Three tensile tests were performed at each temperature, and the 0.2% offset yield strength was averaged over these tests to determine the macroscopic yield strength of the bulk material. The macroscopic yield strengths at RT, 120°C, and 200°C were 905 MPa, 736 MPa and 647 MPa, respectively as shown in Figure 3.4.

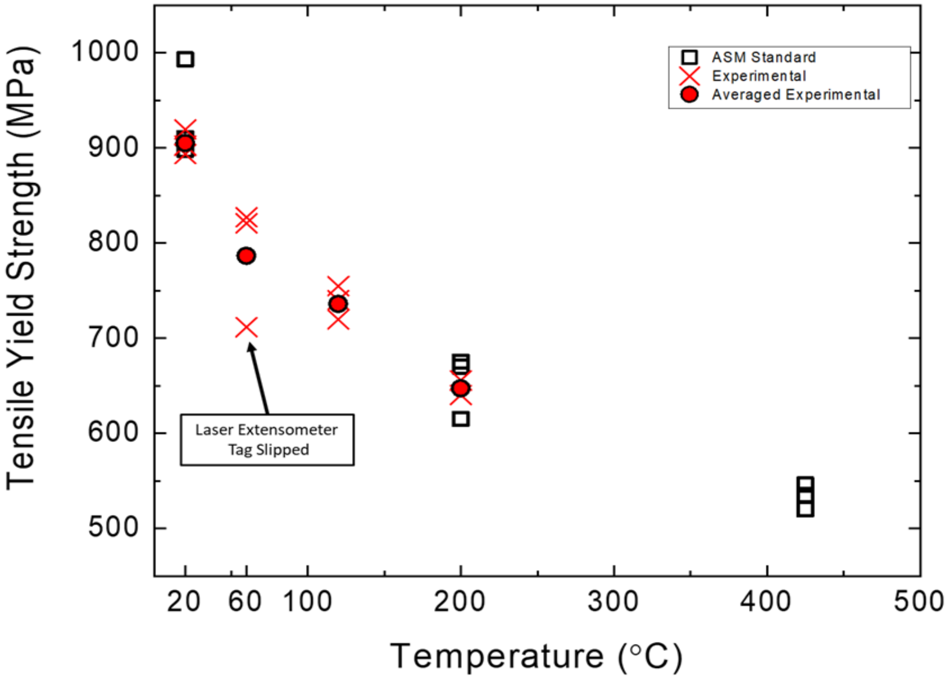

Figure 3.4: Temperature adjusted 0.2% offset yield strength for the Ti-6242 alloys used in this study compared to the ASTM standard values for the temperature adjusted yield strength of Ti-6242. Three tests were run at each of four temperatures (RT, 60°C, 120°C, and 200°C), and the yield strength from each test was averaged to determine the temperature adjusted yield strength. The result from each individual experiment and the averaged values are plotted with red Xs and filled circles, respectively. The temperature adjusted yield strength from the ASTM handbook for Ti-6242 is plotted (black squares) for comparison. While some texture, processing, and sample variation is expected, there is good agreement between the ASTM standard values and the measured strengths. A non-contact laser extensometer and adhesive reflective tags were used to track the elongation of the gauge section with loading.

Load-controlled dwell fatigue experiments were performed to 200 dwell cycles with the experimental setup shown in Figure 3.5. The peak load was held for 120 seconds at 90% of the macroscopic bulk yield strength. Loading was interrupted after 1,2, 5, 50, 100, and 200 dwell cycles to collect SEM images for *ex-situ* SEM-DIC. At each imaging point, the sample was fully unloaded, cooled to room temperature in ambient air, and transferred to a SEM (FEI Teneo). After imaging, the sample was returned to the load frame, heated (if not a room temperature test), and cycled to the next imaging point. Note that during image collection of cycle 1 for the full-gauge AOI samples tested at RT, a beam aberration occurred and distorted a portion of the image tiles. As negligible additional strain or slip activity accumulated between cycles 1 and 2 across all temperatures, cycle 2 is used as the early cycle for comparison rather than cycle 1.

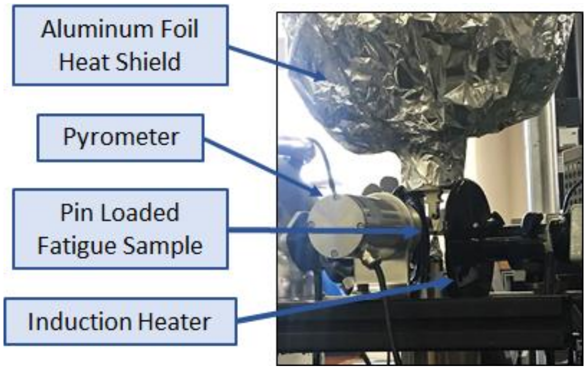

Figure 3.5: Experimental setup in MTS load frame for loading, specimen heating, and thermal monitoring.

The images collected during fatigue interruptions were individually correlated with commercial DIC software (VIC-2D 6) [98] to calculate displacement fields. The displacement fields were then stitched together using the method of Chen et al. [99], from which plastic strain maps over the ~4 mm x 2.5 mm regions and ~500 μm x 500 μm regions of interest were calculated. The resulting ε_{xx} ε_{yy} ε_{xy} strain maps consisted of over 300 million data points at each load step. The stitched DIC strain maps and the EBSD orientation maps were then aligned using the platinum fiducial markers and a projective transformation; although this scheme can cause alignment perturbations local to the grain boundaries that need adjustment at higher resolution studies, this alignment was sufficient at the length scales examined here [99]. The resultant strain maps exhibited long-range plastic slip features, regions of cross slip and pile up, and regions with little plastic strain, as shown in Figure 3.6 and Figure 3.7. The patchwork background of the 200°C DIC strain maps is due to small slip activity and localized and global strains, which resulted in noisier strain fields and a much lower signal-to-noise ratio. At 200°C, the strains are so small that the background strains vary within this noise threshold, creating a tiled look. In this work, the size, shape, and location of the slip features in the strain field were analyzed to understand the effect of temperature and microstructure on residual plastic strain during dwell fatigue. The slip traces are beyond that noise threshold and were therefore able to be individually identified in the strain fields. Note that the commercial DIC algorithm used in this work is a local approach that incurs error in calculating discontinuous strains, such as those exhibited by slip activity; however, the strain values at the slip traces were not considered, but rather their presence and activity.

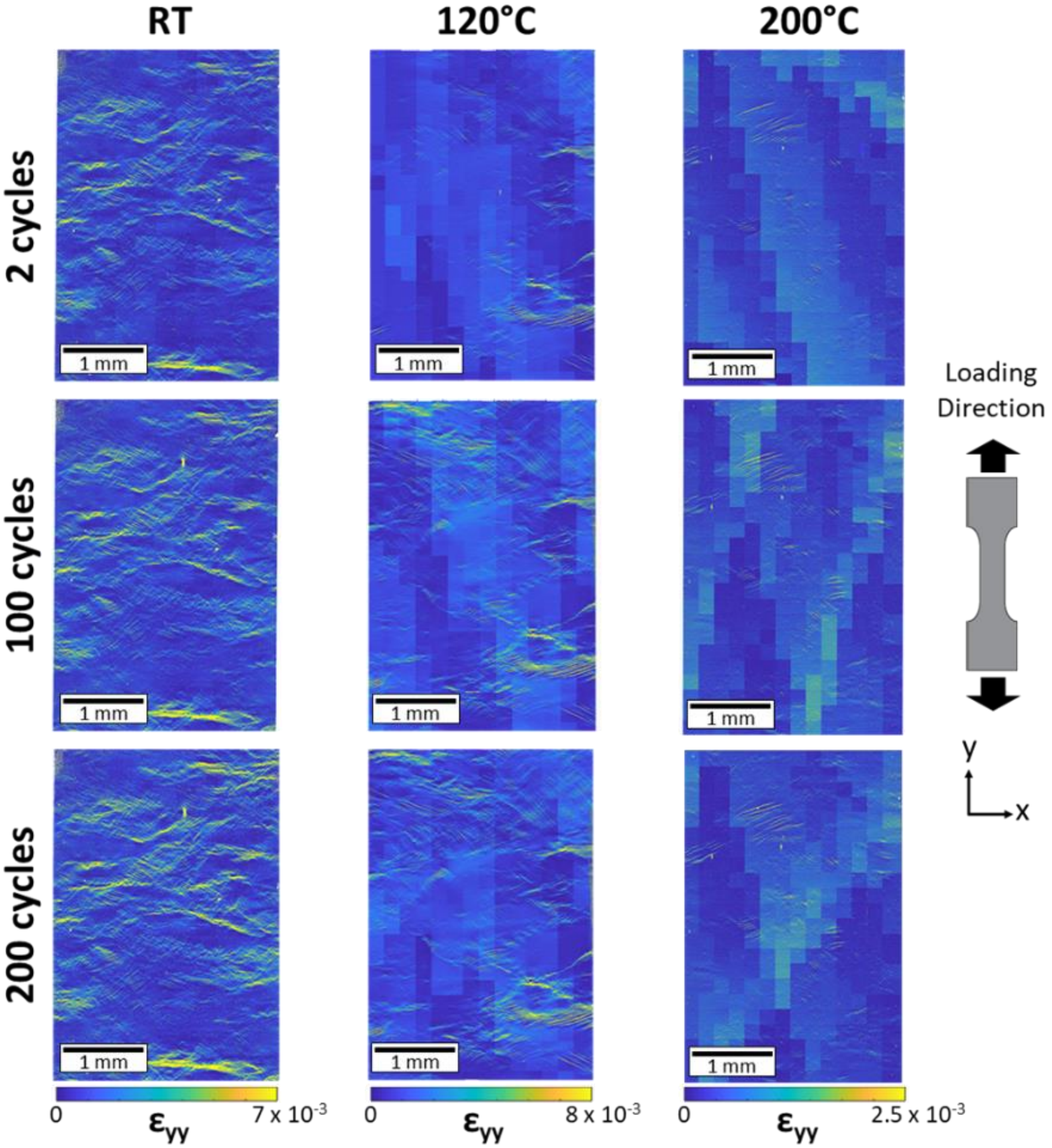

Figure 3.6: Axial strain maps for RT, 120°C, and 200°C after cycles 2, 100, and 200. There is significantly more slip activity and global strain at RT and 120°C. Note that 120°C and 200°C have background noise differences in each tile due to their low strains and low signal to noise ratio (SNR). However, this work investigates the presence and activity of slip rather than the strain values, and these small differences in background noise do not impede the ability to discern slip localization.

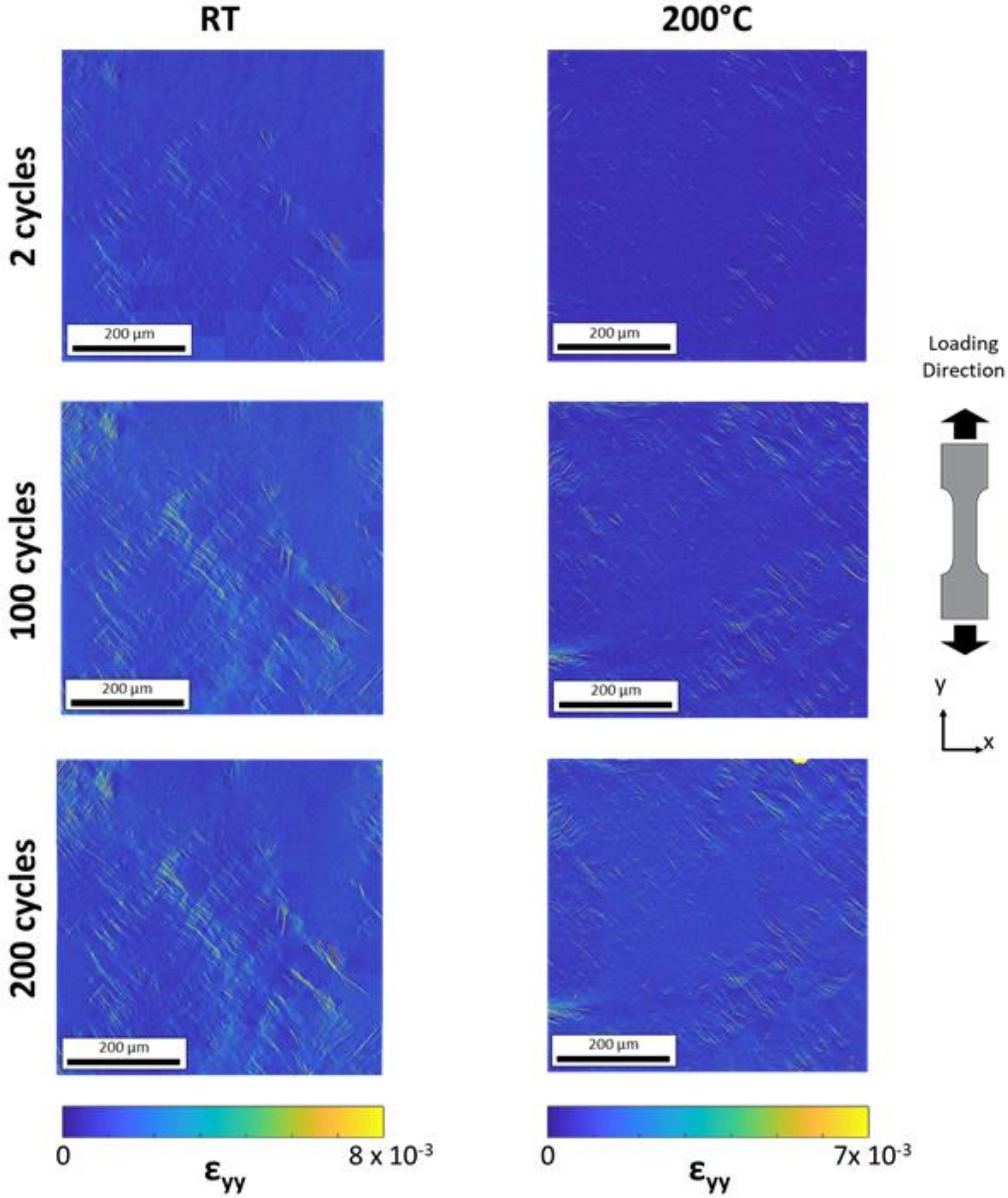

Figure 3.7: Axial strain maps for grain level study for RT and 200°C after cycles 2, 100, and 200. This work investigates the presence and activity of slip rather than the strain values, and the small differences in background noise do not impede the ability to discern slip localization.

3.1 Slip Band Segmentation Algorithm

Manual segmentation of the full datasets was infeasible due to their large size and would greatly limit the amount of data that can be analyzed. In a broader sense, as the amount of data that can be experimentally collected continues to grow rapidly, whether by SEM-DIC or by other methods such as diffraction, there is a corresponding need to increase the throughput rate of data segmentation and analysis by automated methods.

A segmentation approach for an automated first pass, followed by a refining pass on a significantly smaller subset, was created to produce binary masks of slip features through the use of clustering and image processing techniques as follows: First, each strain tile was clustered in the ε_{xx}, ε_{yy}, ε_{xy} strain components using k-means clustering, as slip traces exhibit distinctive surface strains [100]. Typically, six clusters were selected, but increased image noise caused by variations in pattern density or localized clumping required that the number of clusters be increased for a number of tiles after visual inspection. An example of a clustered tile is shown in Figure 3.8B. The cluster with the highest strain values encompassed the slip traces; therefore, this cluster was individually plotted and subsequently converted to a binary skeletonized image. Connected component analysis was applied to identify each feature using the *bwconncomp* function in the MATLAB Image Processing Toolbox with connectivity defined through four nearest neighbors, which takes a binary image and groups regions with adjacent true pixels into distinct features. Individual long-range slip features should exist as a continuous line along a similar slope, but the skeletonization process of thick adjacent slip traces left perpendicular connected branches and loops as artifacts. To eliminate these, these loops were filled and the features re-skeletonized. Next, the feature slope was calculated by applying a linear regression to all points in the feature (Figure 3.8D). The branch points in the feature were identified with the image processing toolbox and removed to break the feature up into individual line segments (Figure 3.8F). The slopes of the individual linear sub-features were calculated and compared to the slope of the original feature. Sub-features with slopes perpendicular to that of the original feature were removed, and sub-features with slopes similar to that of the original feature were reconnected by replacement of the removed branch points. This process was repeated for each individual feature from the original binarization to remove the perpendicular connections of every feature. Connected component analysis was then applied to the binary image to identify the new final linear slip traces (Figure 3.8H). This process was repeated for every tile in the stitched SEM-DIC strain map.

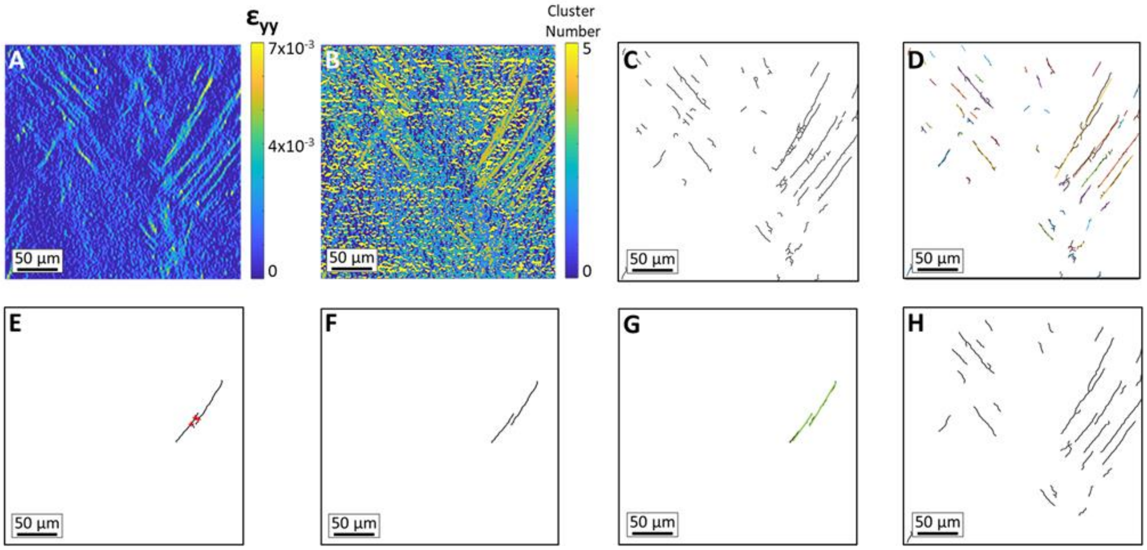

Figure 3.8: Slip Trace Segmentation Process: **(A)** Strain map of individual tile from which to segment slip traces; **(B)** Clustered map of ε_{xx}, ε_{yy}, ε_{xy} strain components of strain tile; **(C)** Binarized image of cluster; **(D)** Slope of binarized features calculated by linear regression; **(E)** Highlighted branch points of an individual slip trace; **(F)** Near perpendicular branches feature removed and remaining near parallel branches divided into individual features; **(G)** Hough transform used to identify individual slopes of slip traces; **(H)** Resultant segmentation mask of slip traces in tile A.

The slip trace segmentation was compared to the strain field for verification. Tiles that exhibited areas of higher noise, due to isolated local issues such as a pattern clump, were more difficult for the automated segmentation process to analyze. A significant amount of cross slip or pile up could also cause segmentation error in the automated technique. However, the point of this initial automated algorithm was not to create a perfect segmentation, but rather to make this process feasible in the first place by automating the majority of the segmentation, combined with a short manual segmentation step on a few select areas. During manual segmentation, the visualization of the clustered strain field aids in separating actual strain features from noise in low signal to noise ratio (SNR) DIC strain fields, such as the fully unloaded plastic strain fields in this study. This procedure is best suited for strain fields with a high SNR and a limited amount of cross slip. Towards the goal of a fully automated segmentation, this process could be improved with the application of machine learning techniques, such as convolutional neural networks, to increase robustness to noisy strain fields and to aid in identifying and separating intersecting slip features. Following this process, the segmentation masks were then overlaid on the strain data and stitched to produce a continuous binary segmentation mask over the entirety of the region of interest Figure 3.9.

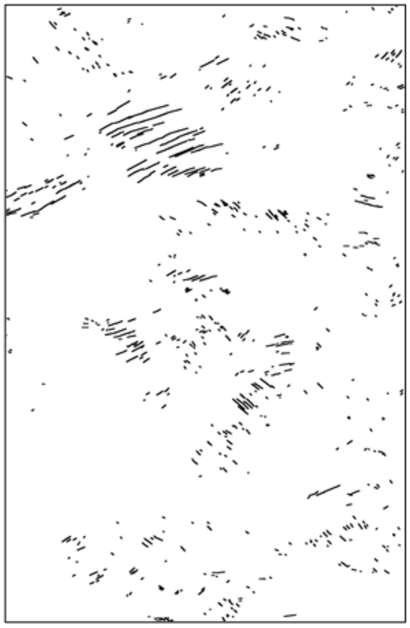

Figure 3.9: : Full-field stitched continuous slip trace segmentation map for Sample C (200°C)

The EBSD orientation information corresponding to each plastic slip feature was indexed and extracted from the multimodal dataset of the aligned DIC strain fields, segmentation masks, and EBSD orientation maps. The Euler angles for all grains that a slip trace passed through were identified, and the statistics of the crystallographic orientations and Schmid factors among these grains were calculated. Additionally, the highest frequency grain orientation (the mode) that the individual slip trace passed through was identified as the dominant orientation using the MTEX toolbox [101]. The length of each slip trace was also calculated by using the MATLAB image processing toolbox. The length of each slip trace was measured directly from the DIC-calculated axial (ε_{xx}) strain fields, and the number of grains that each slip trace traversed was approximated using the average grain diameter. The groups of grains that work cooperatively to allow for slip at each temperature were characterized by considering the relationships between the active slip systems, grain orientations, and geometry of the surface traces. The results and implications of these analyses are presented in the subsequent chapters of this thesis.

Chapter 4 The Effect of Temperature on Slip in Microtextured Ti-6242

4.1 Introduction

The effects of microstructure and temperature on the presence of slip through multiple grains, and the contribution of this slip to the dwell debit of a heavily microtextured near-alpha titanium alloy, were investigated. Plastic slip activity was analyzed in Ti-6242 samples subjected to dwell fatigue at room temperature (RT), 120°C, and 200°C. Slip activity was compared after 2 and 200 dwell cycles following 120 second dwells at 90% of the macroscopic 0.2% yield strength at each temperature, as seen in Figure 3.6.

Due to the non-monotonic dwell sensitivity of Ti-6242, which increases from RT to 120°C and subsequently decreases and effectively disappears beyond 200°C, it is hypothesized that a thermodynamically driven difference in slip activity exists [7], [14], [15], [77]. There is a large disparity in CRSS at low temperature that diminishes at elevated temperature. Consequently, it is tempting to conclude that slip may localize to soft MTRs at low temperature, resulting in the formation of pileups, load-shedding, and crack nucleation, while at elevated temperature more extensive slip in MTRs of all orientations eliminates the possibility of load shedding. However, our experimental findings demonstrate that this is not the case. Plastic slip traces traversing over 100 grain diameters existed at all test temperatures. In all cases, these large slip bands formed only in a contiguous collection of grains well-oriented for basal slip that were themselves embedded inside an aggregate of slightly harder grains.

There have been few attempts to quantitatively characterize microtexture. One notable exception is the work of Woodfield et al. [11], [12], who segmented MTRs from EBSD data using a 20° misorientation angle between adjacent pixels. The authors developed a regression model that related characteristics of MTRs and the primary alpha grains to dwell fatigue capability. The terms in the model included the volume fraction and size of MTRs (called the *primary alpha colony fraction* in the original paper) as well as the size and volume fraction of and degree of crystallographic alignment of the individual primary alpha particles within the MTRs. These results were used to predict fatigue lifetime as a function of microstructure for a wide range of thermomechanical processes [11]. A later formulation by Pilchak et al. [24] extended this method to group grains based on c-axis misorientation and also permitted grouping of non-contiguous pixels into MTRs. The size and shapes of the MTRs obtained by these segmentation algorithms agree well with the size and shapes of the faceted initiation sites on fracture surfaces of failed dwell fatigue specimens [9], [13].

Such observations support the hypothesis that MTRs can behave as large aggregates that allow slip bands to develop across their entirety [9], [43], [86]–[89], but there have only been a limited number of experiments that directly characterize this behavior [90], [91]. These prior works showed the formation of slip traces through similarly oriented grains in a MTR for the first time in Ti-6-4 [90], and highlighted the importance of the physical location and orientation of the MTR relative to the loading direction [91]. Echlin et al. [90] used in-SEM DIC to map slip activity over a range of applied strains below macroscopic yield in Ti-6-4 during uniaxial tensile testing. They investigated slip band formation that occurred in soft regions of a 500 µm x 500 µm field of view encompassing a sandwich-type structure of 3-4 MTR interfaces. The material under study had a basal/transverse texture and was loaded along the rolling direction, and hence did not contain MTRs well oriented for basal slip. There were, however, individual grains well oriented for basal slip within the hard MTRs and also in more randomly oriented regions of material. It was in these grains that basal slip was first observed after an axial strain of 0.65%. Significant amounts of prismatic slip occurred with additional loading. In some cases, these bands traversed the entirety of prismatically soft MTRs. Lunt et al. [91] investigated Ti-6-4 that was unidirectionally rolled to produce a strongly microtextured material. Samples were loaded in tension to 2.5% global strain, and shear strain localized in MTRs that were preferentially oriented for prismatic and basal slip activity when the MTR was physically oriented 45 and 90 degrees to the loading direction. These experiments were not at sufficient spatial resolution to identify plastic slip, but instead were targeted to capture heterogeneous strain behavior across MTRs spanning a large number of grains.

Our experimental findings suggest that current segmentation approaches may not be sufficient to capture the intricate details that govern whether a particular MTR will develop slip. Rather than slip being accommodated homogeneously and diffusely throughout soft-oriented MTRs, we found that plastic slip was instead accommodated by sub-features within classically segmented MTRs (Figure 4.1). These sub-features were well-oriented for basal slip and spatially arranged in a way that aligned the basal slip traces of the individual alpha particles (Figure 4.2 and Figure 4.3).

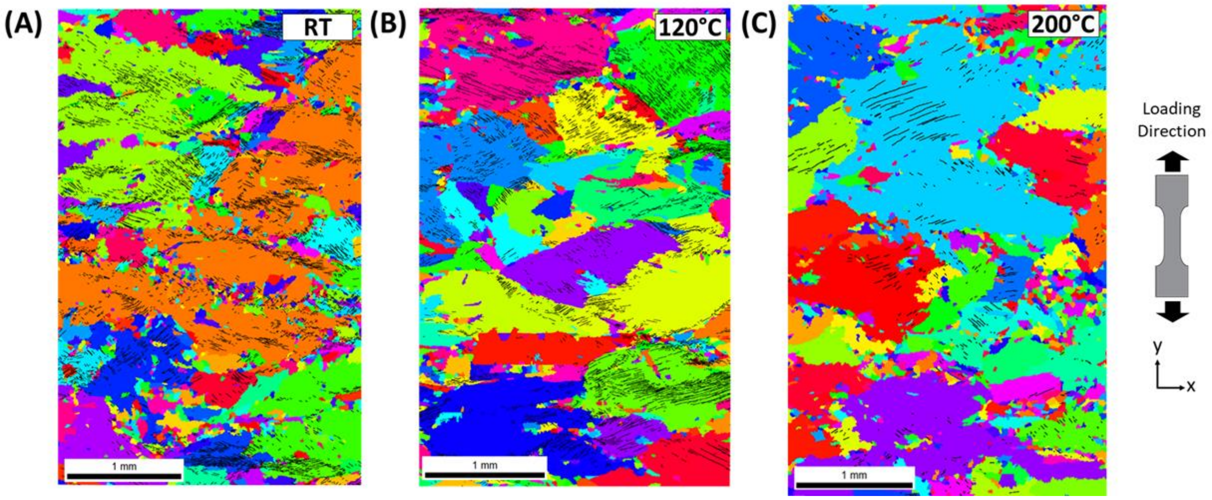

Figure 4.1: A MTR segmentation using prevailing segmentation methods produced by DREAM3D [102] using a 20° misorientation angle between adjacent pixels overlaid with a slip band

segmentation mask obtained from DIC. Different colors represent different MTRs. Long range slip traces exist within MTRs, but they do not traverse across the entire MTR.

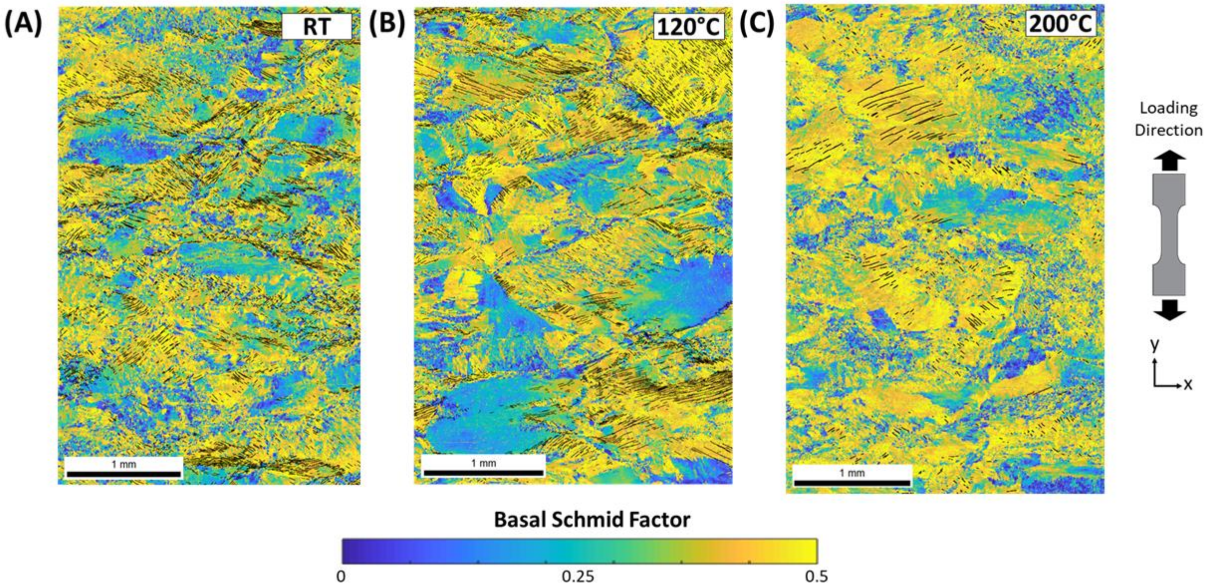

Figure 4.2: A color map of the basal Schmid factor for each point in the EBSD map with slip traces overlaid in black. Rather than slip traces extending through the entirety of the MTRs as defined by a misorientation tolerance (Figure 4.1), slip occurs within and extends through regions with a high basal Schmid factor.

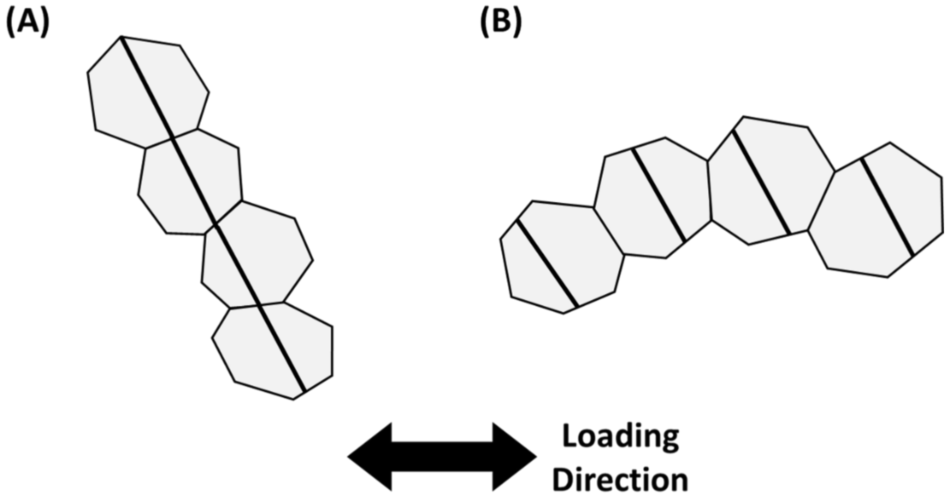

Figure 4.3: Co-located grains must be spatially arranged such that the basal planes of each grain align well for slip transfer. The basal slip planes of the grains in (A) are spatially arranged such that basal slip is able to transfer between grains and form slip features. While the grains in (B) are also spatially co-located and the basal places are at the same angle in each grain, the basal planes of the grains are not arranged to allow for easy basal slip transfer and therefore impede slip.

4.2 Results and Discussion

4.2.1 Number and Accumulation of Slip Traces with Dwell Cycling

At all dwell cycles, the number of slip traces at RT and 120°C was significantly larger than at 200°C (Table 4.1). The lack of slip activity at 200°C may be related to the temperature dependence of strain rate sensitivity [14], [15], [77], where a more rapid stress relaxation occurs with increasing temperature; this reduces the number of dislocations in a given pileup and results in lower effective stresses, due to decreased localized plastic strain accumulation. For example, after two cycles at RT and 120°C, 1909 and 2119 slip traces respectively had formed, versus only 468 slip traces at 200°C. This observation contrasts with Crystal Plasticity Finite Element (CPFE) modeling by Zhang et al. on Ti-6Al [15], a material commonly used as a model material system for Ti-6-4 and Ti6242, loaded to 95% of the temperature-corrected 0.2% offset macroscopic yield strength. Their modeling predicted a higher amount of total (elastic and plastic) strain after one cycle at 200°C than at RT and 120°C.

However, our experimental results on strain accumulation aligned with findings in CPFE modeling performed by Zhang et al. [15] and by Ozturk et al. (on textured Ti-62642) [14], although they attribute this result to different mechanisms. Both found that dwell cycling at RT and 120°C accumulate significant plastic strain after the first cycle, whereas cycling at 200°C does not. In this work, between 2 to 200 cycles, the number of slip traces increased by a factor of 2-3x at both RT and 120°C, but only increased by a factor of 1.4x at 200°C (Table 4.1). Ozturk et al. [14]attributed this lower strain accumulation to load shedding stemming from a reduction in plastic anisotropy at 200°C in the HCP structure of the alpha titanium grains, where the ratio of CRSS required for basal to <c+a> pyramidal slip reduces from 1.8 at RT to 1.2 at 326°C. In addition to a reduced plastic anisotropy, Zhang et al. [15] postulated an additional effect of *cyclic load shedding* active at temperatures below ~200°C. This phenomenon implies the progressive, cycle-by-cycle redistribution of stress from the soft to the hard grain, which occurs by soft grain ratcheting of plastic strain. This occurs only during the hold at peak stress, during which creep strain accumulates via dislocation glide. The magnitude of accumulated strain is a function of the temperature-dependent strain rate sensitivity of the material. Plastic strain accumulates more readily at the intermediate temperature of 160°C when compared to RT, which may explain the increased dwell sensitivity. On the other hand, the creep rate is so high at temperatures above 230^{o}C that strain accumulates over the order of seconds, saturates, and redistributes readily. As a result, the progressive load shedding mechanism that precedes early dwell fatigue crack nucleation is effectively shut off.

Table 4.1: Number of slip traces in each sample after 2 and 200 cycles, at room temperature (RT), 120°C, and 200°C.

	RT	120°C	200°C
Number of Traces After 2 Dwell Cycles	1909	2119	468
Number of Traces After 200 Dwell Cycles	6031	5685	641

At all temperatures, new slip traces occurred largely in regions that had already exhibited slip, as shown in the full-field strain maps of Figure 3.6. There were no locations that exhibited little slip activity after two dwell cycles and subsequently accumulated significant slip. This supports the conjecture that slip and its evolution under dwell cycling are microstructurally driven by groups of grains that allow the traversal of contiguous slip activity.

4.2.2 Slip Features

Of the slip features that developed after two dwell cycles, a larger percentage were long-range at 120°C and 200°C than at RT. This phenomenon is related to active slip family and grain co-location and is discussed in detail in the next section. As shown in the histograms of slip lengths in Figure 4.4, the majority of slip traces formed at 120°C and 200°C after two dwell cycles were greater than 50 microns long (70% and 55%, respectively), versus less than 20% at RT. Additionally, ~30% of the slip traces at 120°C and 200°C were longer than 100 microns, versus only 3% of traces at RT. The distributions at 120°C and 200°C also had much longer tails, indicating that 10% of traces were longer than 200 microns (i.e. traveling through approximately 20 grains or more), with a few extreme cases where traces extended through 1000 microns (~100 grains). In contrast, at RT over 99.9% of the slip trace lengths were under 140 microns long.

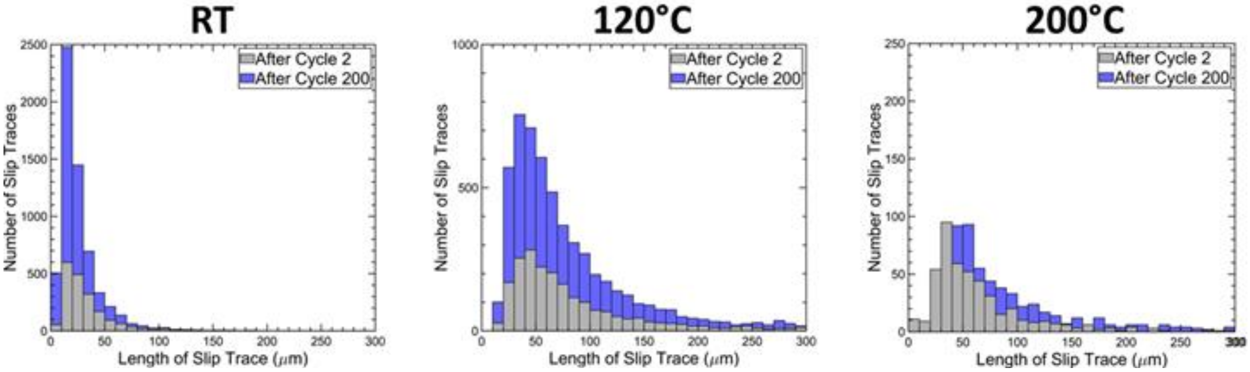

Figure 4.4: Distribution of Slip Trace Lengths. As shown in (A) and in Table II, significantly more slip traces formed at RT and 120°C than at 200°C. Cumulative distribution plots were also assessed to examine the tails of the distributions, but no significant differences were found. The y-axis varies with temperature for clarity.

The slip trace length distributions remained consistent with cycling at all temperatures (Figure 4.4). However, these distributions shifted horizontally with cycling at RT and 200°C. At RT, the distribution shifted slightly left toward shorter slip traces, indicating that most new traces were under 20 microns (<2 grains) long. At 120°C, there was little evolution in the distribution of the slip trace lengths with cycling, indicating that the lengths and regions of slip were determined from the earliest cycles. In contrast, at 200°C a shift right toward longer slip traces occurred with cycling. This shift right indicates that most of the new slip traces that formed in the 200°C case were long, with 60% of them longer than 70 microns and 10% longer than 200 microns. It is important to note that the number of slip traces at 200°C was 10% that of RT, and therefore the weight of each slip trace length contributed more significantly to the slip length distribution.

4.2.3 Grain Orientation Effects

At all temperatures, grains that behaved cooperatively and exhibited plastic slip were (i) co-located; (ii) had high basal and/or pyramidal Schmid factors, with basally-soft slip dominating; and (iii) exhibited small variations in orientation. These factors provided routes for easy slip percolation in basally soft regions at stresses below macroscopic yield.

For each slip feature, the dominant crystal orientation was calculated as the statistical mode of the grain orientations that the trace traversed. This dominant orientation was then used to calculate the Schmid factors for each possible slip system for that crystallographic orientation. The dominant orientation and known global stress state of the sample were also used to identify the active slip system for each of the slip traces. The slope of the projection of each slip trace on the surface of the sample was compared to the slope of the observed plastic slip surface trace. The slope of the observed surface trace was identified in the slip trace segmentation mask using a Hough transform. Only slip traces within nine degrees of the predicted slip trace were considered identifiable. Approximately 18% of traces were not able to be identified because the deviation between the measured slip band and the nearest slip plane trace exceeded the tolerance angle. The statistics of unidentified bands were investigated and there was no evidence that would indicate disproportionate misidentification of any particular slip family. The dominant crystal orientation of each slip trace is shown on an inverse pole figure (IPF) in Figure 4.5. For every temperature, slip traces tended to occur through grains with their c-axis near 30°-45° to the loading direction and with a high resolved shear stress on the basal plane.

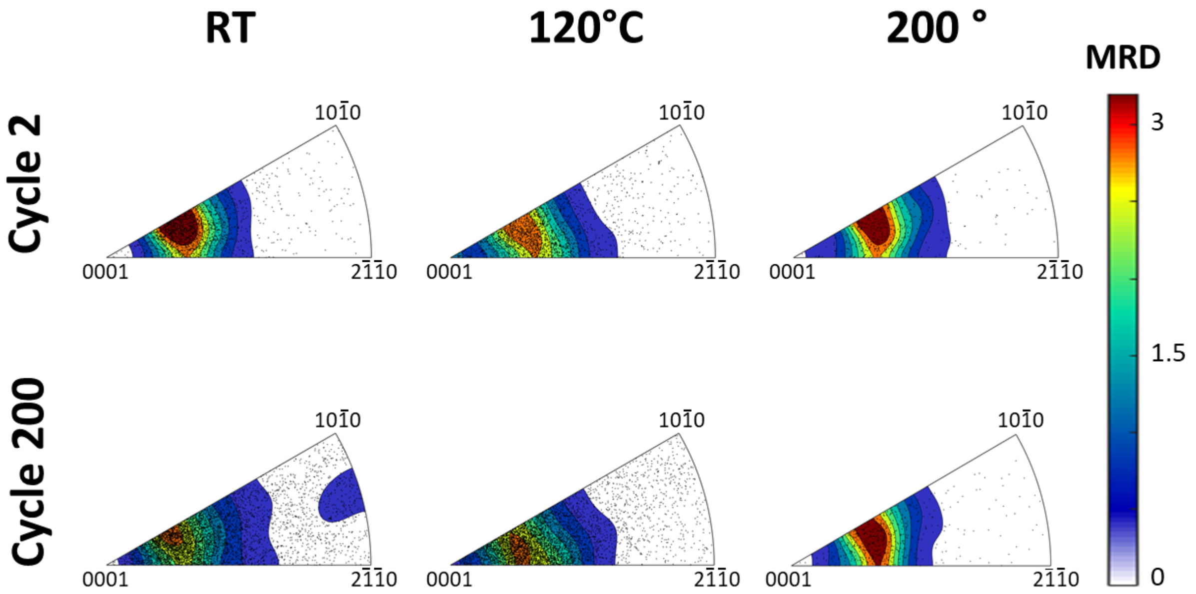

Figure 4.5: Slip trace orientations plotted on an IPF for samples tested at RT, 120°C, and 200°C, after 2 and 200 cycles. At all temperatures, slip traces tended to occur through grains with a high resolved shear stress on the basal plane.

At all temperatures, slip primarily occurred through grains with high basal and/or pyramidal Schmid factors, with basal slip dominating as a result of its lower CRSS. The relatively high amount of pyramidal slip was likely due to two reasons: 1) slip primarily occurred through grains with their c-axis 30-45° relative to the loading direction, and therefore had appreciable resolved shear stress on basal <a> and pyramidal <c+a> slip systems; and 2) some pyramidal slip occurred in grains with an <a> or <c+a> pyramidal Schmid factor of >0.3 (Figure 4.6), that were located near basal slip activity, attributed to internal stress accommodation. Schmid factors for the dominant crystal orientations were calculated for each of the 24 slip plane-direction combinations. The basal, prismatic, and pyramidal Schmid factors for each trace are reported in Figure 4.6 relative to slip type. At RT and 120°C, over 80% of traces had a basal Schmid factor of 0.35 or greater (at all cycles). At 200°C, over 90% of the slip traces had a basal Schmid factor of 0.35 or greater (at all cycles). Slip also required a pyramidal Schmid factor greater than 0.3, for 99.9% of slip traces and at all temperatures (Figure 4.6).

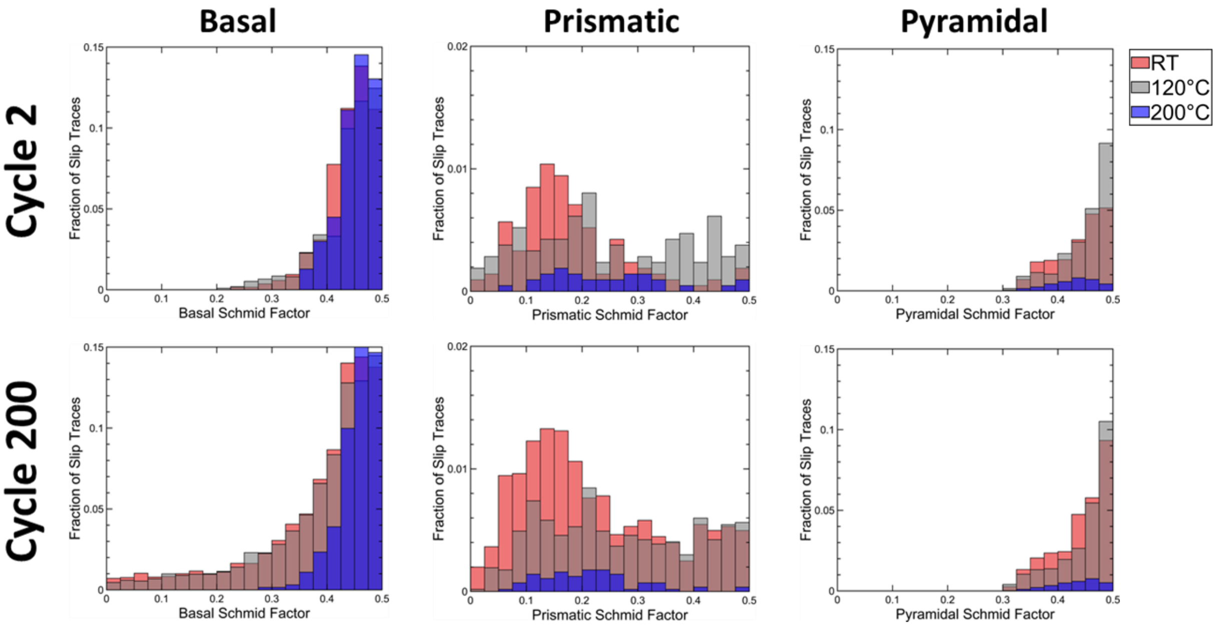

Figure 4.6: Histogram of the **(A)** Basal, **(B)** Prismatic, **(C)** Pyramidal Schmid factors of each slip trace at RT, 120°C, and 200°C. At all temperatures, slip primarily occurred through grains with high basal and pyramidal Schmid factors. In the case of prismatic slip, the small number of traces affected the distribution shape (note the y-axis is set to 2% in this plot for visualization). Note that the red, gray, and blue bars are semitransparent to aid in visualization of overlapping data.

The grains that each slip trace traversed exhibited small orientation variations. The standard deviation of the basal Schmid factor for the grains traversed by each slip trace was less than 0.25, (Figure 4.7). For each slip trace, the basal Schmid factor was calculated for each grain that the trace passed through.

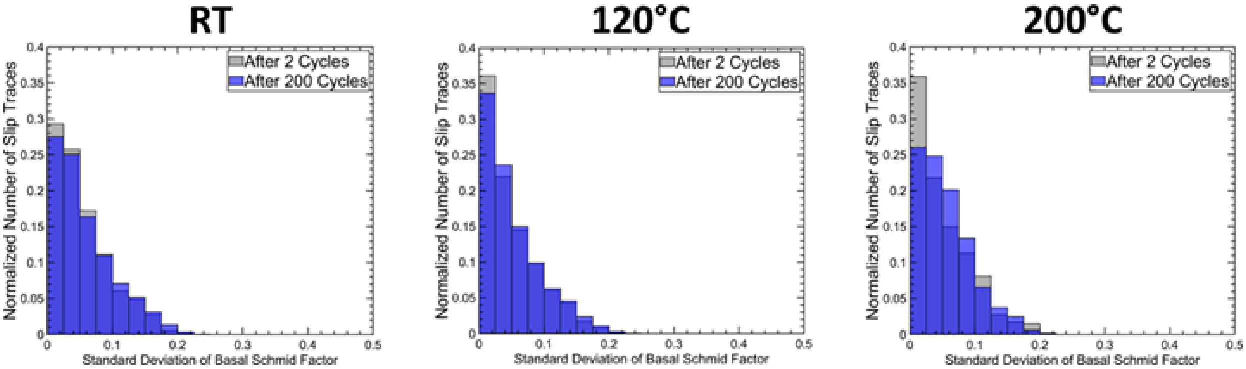

Figure 4.7: Standard deviation of basal Schmid factors for each slip trace at RT, 120°C, and 200°C. The individual grains that each trace traversed exhibited small variations in orientation.

At all temperatures, basal slip initiated early and dominated with cycling, making up over 55% of the total slip activity (Figure 4.8). Basal slip was expected as it is relatively easily activated, but unexpectedly, there was less than 15% prismatic slip activity. Rather, pyramidal slip was the second most active system at all temperatures and cycles. Pyramidal slip is reported as being 3-5 times more difficult to activate than basal and prismatic slip in Ti-6242 [4], [7], [42], yet in every loading case it accounted for more than 25% of slip activity. This is likely due to the exhaustion of easily activated basal slip, followed by the subsequent activation of slip in neighboring regions that favored pyramidal over prismatic slip; this will be further discussed in the context of the relative slip locations, active Schmid factors, and slip travel lengths. It should be noted that it was not possible to distinguish between the <c+a> vs <a> pyramidal slip from the surface traces, and these were counted together as pyramidal slip. While <c+a> pyramidal slip is known to have a CRSS 3-5 times larger than basal and prismatic slip, <a> type pyramidal slip is reported as having a CRSS ~0.9 - 1.1 times larger than basal and prismatic slip in near-alpha titanium alloys [38], [41]. Therefore, it is thought that the slip activity is <a> type pyramidal slip, but this cannot be confirmed without further analysis.

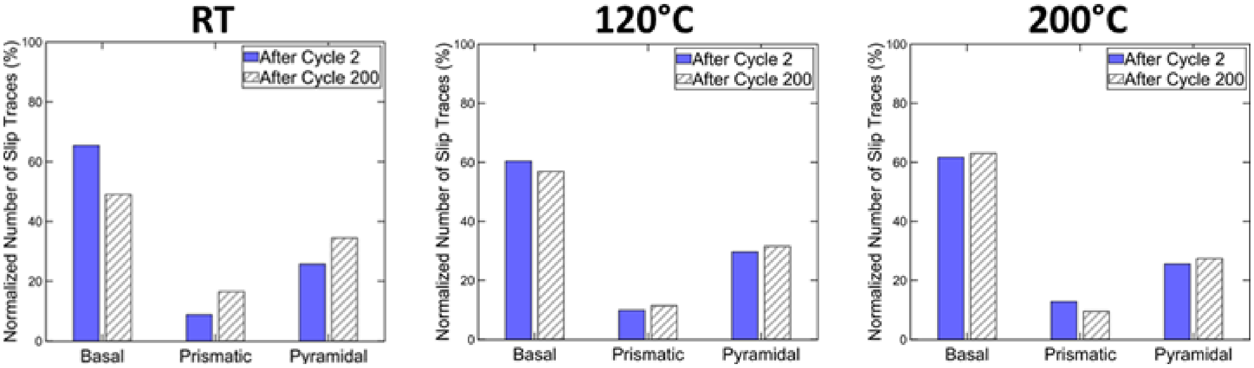

Figure 4.8: Active slip systems for the identified slip traces after 2 and 200 cycles at RT, 120°C, and 200°C. Basal slip initiated early and continued to dominate with cycling, but there was little long-range prismatic activity. Rather, the relatively high activity of pyramidal slip was attributed to the exhaustion of easily activated basal slip, and the subsequent activation of slip in neighboring regions that favored pyramidal over prismatic slip.

Most basal slip traces (>60%) were longer than 80 microns, extending up to 200 microns in length at RT and beyond 1000 microns in length at 120°C and 200°C (Figure 4.9). Despite a larger number of pyramidal slip planes, slip traces observed on pyramidal <a> and/or <c+a> slip systems were typically significantly shorter and less numerous than basal slip traces, with the shortest pyramidal slip traces at RT. In all cases, over 80% of pyramidal slip traces traversed less than 80 microns. At RT, 100% of the observed pyramidal traces were less than 80 microns long. This may be attributed to the accommodation of internal stresses and/or load shedding, where a localized stress was imparted on a hard grain after significant deformation occurred in the nearby basally soft grains.

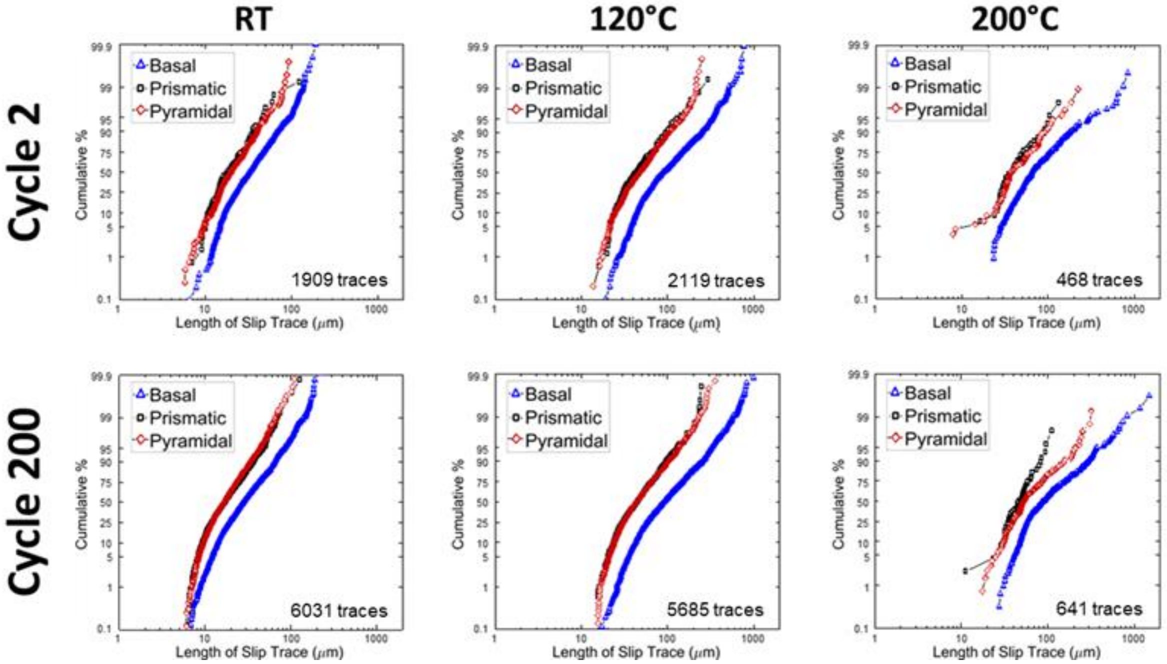

Figure 4.9: Cumulative distribution functions (CDFs) of slip length and family after 2 and 200 cycles at RT, 120°C, and 200°C. The bulk of deformation at all temperatures was accommodated by long-range basal slip in co-located grains, and shorter pyramidal slip in nearby grains that were not necessarily co-located.

Significant slip below the macroscopic yield strength, as in this work, has also been observed in prior experimental studies, although the identified slip trace lengths and families differ [45], [60], [61], [90]. Experiments on surface slip activity in Ti-6-4 have uniformly observed an onset of basal slip first, with prismatic slip then occurring at slightly higher loads [45], [60], [90]. The CRSS required to activate basal and prismatic slip in near-alpha titanium alloys is close, where some work has observed a slightly lower CRSS for basal than prismatic slip [4], [7], [14], [25], [42], [43] and vice versa [41], [44], [45]. The reported CRSS required to activate each slip system varies with alloy and microstructure. In the RT *in-situ* tensile loading of Ti-6-4 at globally applied strains below 0.71%, Echlin et al. identified primarily basal slip across two or fewer grains. In contrast, at globally applied strains of 0.71% and above, they largely observed long-range prismatic slip that traversed the entire length of the prismatic soft MTR, through as many as 20 grains. Lavogiez et al. [45] had similar findings in dwell fatigue experiments on Ti-6-4 at RT, where they observed basal slip dominating in individual soft grains during early dwell cycles at 90% of macroscopic yield. With additional cycling they observed significant prismatic slip in individual grains. They repeated the test, this time loading to a higher stress of 94% of macroscopic yield and observed the onset of prismatic slip earlier than for the 90% of yield case. Zhang et al. [61] also experimentally observed both basal and prismatic slip activity after loading to ~3% strain in Ti-6-4, but that prismatic slip dominated . In this work, even after 200 dwell cycles at a peak stress of 90% of yield, significant prismatic slip was not detected at any temperature. It is important to note that these other studies were performed on Ti-6-4, which is known to have a smaller dwell debit than Ti-6242 at room temperature. When loaded to 90% of the macroscopic yield strength at room temperature, Ti-6-4 only exhibits a dwell debit of ~2-3 times the LCF lifetime, while Ti-6242 has a dwell debit of ~10-20 times the LCF lifetime [6]. While the mechanisms behind the dwell debit are believed to be the same for both materials, one would expect there to be a difference in the strain heterogeneity and load shedding behavior relative to loading and temperature. Because of this unexpected observation, TEM studies are underway to investigate the lack of prismatic slip activity.

While the co-location of grains was a driving factor for basal slip formation, this did not appear to be as important a factor in pyramidal slip formation. The bulk of deformation at all temperatures was accommodated by long-range basal slip in co-located grains (favorably oriented for basal slip), and shorter pyramidal slip in nearby grains that were not necessarily co-located (favorably oriented for pyramidal slip). All pyramidal slip occurred through grains with a pyramidal Schmid factor greater than 0.3, and over 70% of the pyramidal slip traces were in grains that had a pyramidal Schmid factor greater than 0.4 (Figure 4.6). This minimum requirement on the pyramidal Schmid factor did not change with additional cycling.

After two cycles, over 99.5% of basal slip occurred in grains with a high basal Schmid factor (>0.3) at all temperatures. However, with additional cycling from 2 to 200 cycles, the Schmid factor required to initiate basal slip dropped significantly at both RT and 120°C (from 0.21 to 0.08 and 0.22 to 0.08, respectively). After 200 cycles at both RT and 120°, approximately 8% (7.8% and 8.2% respectively) of all basal slip was through grains with a basal Schmid factor lower than 0.25. At 200°C, no such drop in the required basal Schmid factor occurred with additional cycling (the minimum remained constant at 0.35), and 90% of all active basal slip activity had a basal Schmid factor greater than 0.4 after both 2 and 200 cycles. Prior work has observed slip primarily occurring in individual soft grains with a basal Schmid factor above 0.4. A tensile experiment observing grain level slip activity in Ti-6-4 loaded to ~3% strain by Zhang et al. [61] and a dwell fatigue experiment on Ti-6242 by Hemery et al. [44] both observed basal activity in grains with a high basal Schmid factor, but there was some slip activity in soft grains with a basal Schmid factor of 0.2 to 0.4. These studies align with the present study on MTRs, where at all temperatures most long-range plastic slip bands traversed through grains with a basal Schmid factor above 0.4, but a non-negligible number of basal slip traces occurred through grains with a lower basal Schmid factor.

The proposed mechanism for slip activity in regions with low basal Schmid factors and in less favorable hard oriented regions at RT and 120°C is as follows. Deformation was initially and largely accommodated by basal slip in well-oriented grains (Figure 4.6). Prismatic and pyramidal slip was found, by visual inspection, to largely occur in grains where nearby grains were deformed heavily by basal slip (Figure 4.10). This basal slip could not traverse easily into the neighboring hard grain and could therefore create dislocation pileups and associated internal stresses [62]. This internal stress and/or exhaustion of basal slip resulted in deformation either on less favorable slip systems in that grain, or in neighboring hard grains. Pilchak et al. [62] observed both of these mechanisms in TEM foils extracted from beneath dwell fatigue crack nucleation sites in Ti-8Al-1Mo-1V. In our work, these secondary slip processes occurred primarily by pyramidal slip in grains with a high pyramidal Schmid factor, but a small amount of prismatic slip also occurred. The grains that slipped pyramidally required a high Schmid factor, as pyramidal slip is more difficult to activate than prismatic slip. Those that deformed prismatically had a more random distribution of prismatic Schmid factors (with a small peak at around 0.125), based on which grain orientations were adjacent to the long-range basal slip. Whether the basally-soft grains must be surrounded by hard grains to exhibit long-range slip activity is a topic for further research. The moderate number of active pyramidal slip systems indicates that dwell debit and slip activity are not solely orientation dependent, and that there is the additional impact of the surrounding neighborhood. Additionally, pyramidal slip activity could indicate stress redistribution after more favorable slip systems are exhausted and a stress localization is created due to the high level of deformation in the basally soft regions [61]. This is still an open question and an active area of interest.

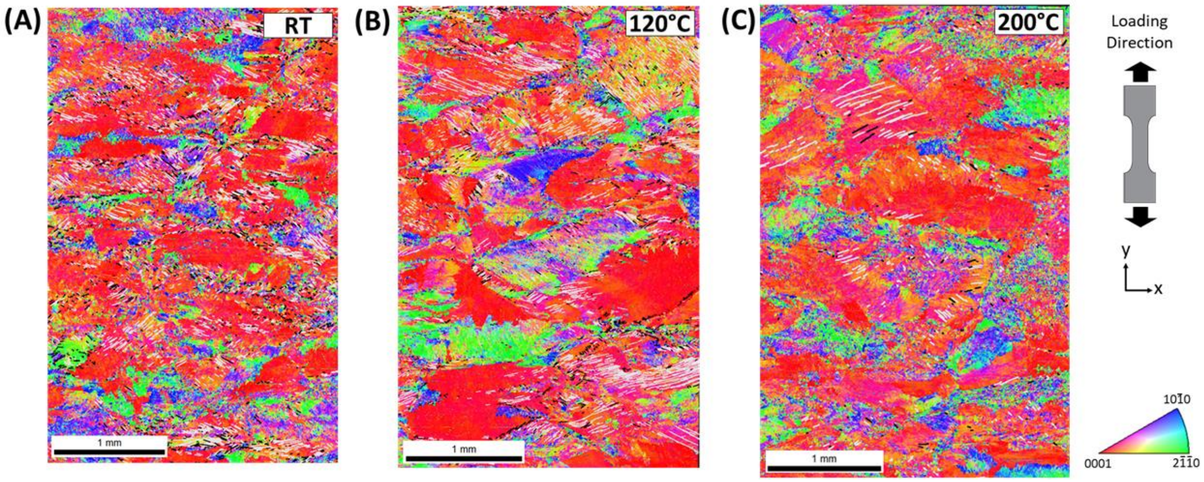

Figure 4.10: Basal (light gray) and pyramidal (black) slip traces overlaid on the IPF map for **(A)** RT, **(B)** 120°C, and **(C)** 200°C. Basal slip traces exist in basally soft grains within hard MTRs, and pyramidal slip exists in nearby grains. This is attributed to the accommodation of internal stresses after basal slip exhaustion.

4.2.4 Implications for Identification of Microtextured Region

The results of this work are relevant to strategies for segmenting MTRs from EBSD data for use in material characterization and modeling. As mentioned earlier, prior approaches allow for a relatively large misorientation or c-axis misorientation tolerance (~20^{o}) and may also permit clustering of non-contiguous groups of alpha phase into the MTR. These approaches result in MTR segmentations that compare favorably with the overall size of the faceted initiation sites of fractured dwell fatigue samples [9], [63], and hence can be used to develop model inputs for MTR-sensitive crack growth models [103]. Moreover, these segmentation approaches have been successfully used to model the effect of MTRs on mean material behavior [11], [12], [24], [104]. However, it is worth noting that there have been no systematic investigations with detailed characterization of a sufficient number of tested samples to determine if these segmentation parameters adequately capture the MTRs that control the minimum, or *life-limiting*, behavior.

When considering the mechanisms that lead to crack initiation, however, the above criteria may not be the most accurate representation of the regions capable of developing slip bands that span many alpha grains and are therefore capable of developing strong dislocation pileups that contribute to crack nucleation. Instead, the regions of intense slip occur in subdomains of active basal-soft grains embedded within slightly harder MTRs defined by prevailing methods. Segmentation strategies for crack initiation need to include a requirement for grain connectivity (Figure 4.3) and a reduced point-to-point c-axis misorientation tolerance. The grains involved in the development of long slip bands also required a higher degree of alignment than the ~20° tolerance used to segment MTRs in prior studies [11], [12], [24]. Furthermore, specific attention should be given to the volume fraction and size of regions capable of deforming by basal slip as these are the structural units which are developing the most intense slip bands and which act as the "soft grain" in the classic hard/soft model of dwell crack nucleation. A low volume fraction of MTRs in this orientation would correlate to improved dwell fatigue crack nucleation resistance, which is consistent with (and only a small refinement) to the work of Woodfield et al. [12]. Since MTRs are important with respect to both crack nucleation and crack propagation, they should be characterized from these two perspectives depending on the intended use of the data.

Finally, we found no evidence that MTRs well-oriented for prismatic <a> slip could develop similarly long slip bands. While seemingly contradicting the results of [45], [60], [61], [90] who observed the activation of prismatic slip, it is worth noting that these investigators were looking at the individual crystallite scale and not the aggregate response of many crystallites. A TEM investigation of the current samples is underway to determine the extent of prismatic <a> slip in suitably-oriented grains, but the present work shows that prism <a> slip bands do not readily organize into long slip bands traversing many grains, and hence may not be suitable to act as the "soft grain" in the currently accepted dwell fatigue crack nucleation mechanism. One obvious reason for this type of behavior would be that if a single prism <a> slip system has a high resolved shear stress, there are, because of crystal symmetry, a multitude of other prism and pyramidal <a> slip systems that could operate to relieve the stress concentration associated with a pileup. In contrast, there is only one basal plane orientation per grain and if these systems are highly stressed, there is necessarily lower resolved shear stress on the easy-to-operate pyramidal and prism <a> slip systems offering fewer opportunities for cross-slip. Such an effect could be exacerbated by the presence of Ti_3Al, which is known to further promote slip planarity.

4.3 Conclusions

An *ex-situ* study of plastic strain accumulation in Ti-6242 was conducted under dwell fatigue loading at room temperature (RT), 120°C, and 200°C to characterize slip activity with a goal of understanding its effects on dwell fatigue lifetimes. Our findings suggest that current segmentation approaches may not be sufficient to capture the intricate details that govern whether a particular microtextured region (MTR) will develop long-range slip. Rather than slip being accommodated homogeneously and diffusely throughout soft-oriented MTRs, we found that slip was instead accommodated by sub-features within classically segmented MTRs. These sub-features were well-oriented for basal slip and spatially arranged in a way that aligned the (0001) traces. Additionally,

- Slip did not transmit across the entirety of MTRs defined by prevailing methods, but rather was driven by contiguous groups of basal-oriented grains. This differs from the behavior of MTRs in crack growth studies, where similarly oriented grains do not need to be interconnected to behave cooperatively and permit rapid crack growth. The observed slip systems and Schmid factors in this study narrow the definition of MTRs that accumulate damage under dwell fatigue loading. In particular, these results indicate the necessity of grain interconnectivity, and that the current allowable 20° spread in c-axes should not be used when identifying the boundaries of a MTR.

- There was both a greater number and a faster accumulation of slip traces at temperatures that exhibit a dwell debit in Ti-6242 (RT and 120°C) versus that which does not (200°C). The lack of slip activity at 200°C may be related to the temperature dependence of strain rate sensitivity [14], [15], [77], where a more rapid stress relaxation occurs with increasing temperature, thereby reducing the number of dislocations in a given pileup and resulting in lower effective stresses due to decreased localized plastic strain accumulation.
- At all temperatures (RT, 120°C, and 200°C), new slip traces occurred largely in regions that had already exhibited slip. There were no locations that exhibited little slip activity after two dwell cycles and subsequently accumulated significant slip. This supports the conjecture that slip and its evolution under dwell cycling are microstructurally driven by cooperative grain groupings that allow the traversal of contiguous slip activity.
- At all temperatures (RT, 120°C, and 200°C), grains that behaved cooperatively and exhibited long-range plastic slip were (i) co-located; (ii) had high basal and/or pyramidal Schmid factors, with basally-soft slip dominating; and (iii) exhibited small variations in orientation.
- There was little observed long-range prismatic slip activity, despite it being typically reported as the softest slip system. These observations do not necessarily imply no prismatic slip is occurring, but that if so, it does not manifest as long-range planar slip traces visible on the surface of the sample during dwell fatigue at 90% of macroscopic yield.

- Deformation at all temperatures was largely accommodated by long-range basal slip in co-located grains with high basal Schmid factors, and shorter pyramidal slip in nearby grains with high pyramidal Schmid factors. No significant prismatic or pyramidal slip was observed to occur independently in areas far from those of basal slip. This is likely due to internal stresses initiating the activation of less favorable slip in the neighboring grains following the exhaustion of basal slip, indicating that the dwell debit is not solely orientation dependent and that we must also consider the effect of microstructural neighborhood.
- With cycling at RT and 120°C, the minimum Schmid factor required to initiate basal slip decreased from ~0.2 to ~0.08; however, at 200°C, the basal Schmid factor required to initiate basal slip remained constant at 0.35. This is due to the exhaustion of easily available slip activity while needing to accommodate additional deformation with cycling at RT and 120°C. At 200°C, little additional deformation accumulated with cycling. Between 2 to 200 dwell cycles, the number of slip traces increased by a factor of 2-3 at both RT and 120°C, but only increased by a factor of 1.4 at 200°C (Table 4.1).
- Pyramidal slip largely manifested in short traces. The relatively high amount of pyramidal slip was likely due to two reasons: 1) slip primarily occurred through grains with their c-axis 30°-45° relative to the loading direction, and which were therefore well oriented for both basal and pyramidal slip; and 2) some pyramidal slip occurred in grains with a high pyramidal Schmid factor (>0.3) that were located near basal slip activity, likely due to the internal stresses and stress redistribution caused by a significant amount of basal slip. Due to the projections of the surface traces on the surface of the sample, it was not possible to distinguish between <a> and <c+a> pyramidal slip. While <c+a> pyramidal slip is known

to have a CRSS 3-5 times larger than basal and prismatic slip in near-alpha Ti alloys, <a> type pyramidal slip is reported as having a CRSS ~1.1 times larger than basal and prismatic slip in near-alpha Ti alloys [41]. Therefore, it is suggested that the pyramidal slip activity is <a> type pyramidal slip, but this cannot be confirmed without further investigation.

Chapter 5 Defining Effective Structural Units in Ti-6242 for Slip Localization in Dwell Fatigued Ti-6242

5.1 Introduction

When defining hard and soft grains or groups of cooperative grains in a MTR under dwell fatigue loading, the sole use of the c-axis is not a complete metric for segmentation or identification. Rather, in this chapter we propose and explore the use of a directionally dependent strength-to-stiffness ratio to define soft MTRs that act cooperatively in dwelled Ti-6242.

This study indicates that an optimal, widely applicable c-axis tolerance angle for the identification of hard and soft grains and microtextured regions in dwell fatigued alpha titanium does not exist. Most existing methods for identifying hard and soft regions utilize the orientation of the c-axis relative to the loading direction. Examples include the modified Stroh model [5] and recent CPFE models [14], [15], [65], [67]. The majority of approaches for MTR segmentation cluster spatially nearby grains with similar c-axis orientations to define regions that behave as an effective structural unit under certain conditions. Each method requires thresholding to categorize orientations in a field. Many different investigations have been performed to determine the optimal threshold for identification [9], [11], [12], [103], [105]. While many of these studies have identified appropriate thresholds, these thresholds are tied to a specific application and none of them apply to the observed deformation of Ti-6242 under dwell fatigue loading. For example, a 20° misorientation tolerance works well to define an MTR when trying to match the size and shape of the faceted site of a dwell fatigue fracture surface to the MTR, but MTRs defines with this tolerance angles do not match the observed long range slip traces in a dwelled sample of microtextured Ti-6242.

In this study, various c-axis tolerances for both the definition of hard and soft grains and the definition of MTRs is compared to the slip activity in a microtextured sample of Ti-6242 under dwell fatigue loading to 90% of the macroscopic yield strength. These investigations are performed over the entire ~2.5 mmx 3 mm gauge section of Ti-6242 dwell samples. When using the c-axis alone, there is no tolerance angle on the c-axis that accurately predicts regions that behave as soft grains in the modified Stroh model for dislocation pile up and load shedding. Additionally, there is no c-axis tolerance angle that correctly defines MTRs and regions of cooperative slip activity under dwell fatigue loading. Even if some tolerance angle produces an appropriate identification of a soft grain or MTR in a small subset of points, that tolerance angle is not applicable to the entire gauge section.

It was found in this work that the ratio of basal slip strength to directional elastic modulus for each grain captures regions that act cooperatively during the dwell fatigue of Ti-6242 and is a promising approach for MTR segmentation and identification. The directional strength-to-stiffness ratio depends on the orientation of the c-axis relative to the loading direction, but uses the effective modulus of elasticity and the directionally-dependent slip strengths of a grain to determine the local, orientation-dependent ease of deformation, specifically slip. The use of the strength-to-stiffness ratio to predict the grain-by-grain succession of slip activity under uniaxial loading was first suggested by Wong et al. [106] for FCC materials. It was later adapted to HCP materials by Kasemer et al. [107] to show the order of slip family activation in a CPFE model. The results were validated against a uniaxially tensile-loaded sample of Ti-6-4. In this work, the experimentally observed slip activity in dwelled Ti-6242 occurred primarily in regions with a low basal strength-to-stiffness ratio. Under the loading conditions and number of cycles examined in this work, basal slip is the predominant active slip type and an accurate metric for the slip strength. In previous work on the strength-to-stiffness ratio by Wong and Kasemer, both works considered more potential active slip systems for their strength parameter of the strength-to-stiffness ratio [107], [108]. Under higher applied loads or at higher cycle counts, it may be necessary to consider different slip systems and their relative slip strengths for an accurate representation of cooperative working grains.

5.2 C-axis Definitions

5.2.1 MTRs

Crystallographic misorientation alone is not sufficient to identify regions of the microstructure that work cooperatively and permit slip transfer through MTRs during dwell fatigue loading of Ti-6242. In section 4.1, MTRs defined with a 20° misorientation tolerance or c-axis orientation relative to the loading direction tolerance do not capture the effective structural unit of the microstructure under dwell fatigue. We explore whether a smaller tolerance angle may capable of capturing the subfeatures of these MTRs defined by prevailing methods.

the contiguous grouping of primary alpha grains is a necessary MTR segmentation parameter in order to allow slip transfer between similarly oriented grains, as suggested in Chapter 4. To examine this hypothesis, misorientation and minimum feature size tolerances were varied in a Dream3D MTR segmentation algorithm to determine an optimal segmentation. The microstructure and slip trace maps for Sample C, the large FOV test run at 200°C, were used in this exploratory study. Example cases with 10°, 15°, and 20° misorientation tolerances and a minimum feature size of 100 um^2 (approximately one grain), 200 um^2, and 280 um^2 were analyzed using a Dream3D pipeline (details about this routine are in Appendix A) that allowed running c-axis average grouping and required contiguous grain groupings. The results of these segmentations are shown in Figure 5.1. Narrowing the misorientation tolerance to 10° still did not produce MTRs that matched the length of identified long-range slip traces after 200 dwell cycles and did not segment features of MTRs that act cooperatively.

Misorientation tolerance alone does not describe the commonality grains share when acting as a single structural unit. A parameter study of misorientation tolerances found no segmentation that groups grain clusters acting cooperatively for slip transfer under dwell fatigue loading. This is further evidenced by an investigation of the effect of tolerance angle, in which a subsection of the full orientation map was segmented. A cropped section of the gauge was selected as a test case, as there was clear variation in grain orientations spatially appearing as clusters approximately 20° relative to the loading direction, as seen in Figure 5.2. The slip traces traversed through the clustered subfeatures with a greater deviation in the angle between the [0001] plane normal and loading direction, meaning that they are less hard by traditional c-axis hard/soft definitions. Segmentations were run with the allowable c-axis misorientation ranging from 2-10° with a minimum feature size of 2 pixels. Unlike the full gauge segmentations, the c-axis averaging feature was turned off to allow for the two separate regions to be individually identified. The c-axis misorientation between these two regions in Figure 5.2 is small and the gradient in c-axis orientations between the two regions appears smooth. If the c-axis running average feature was used, the orientations of the two separate subregions would not cause the average to change dramatically enough to be considered separate regions. Rather, the two regions would be considered one MTR. The c-axis running average feature is meant to make finding the edges of very distinct features easier by averaging over subtle orientation changes outside of the orientation tolerance. This is useful if the grouped regions of interest have distinctly different orientations, such as for MTRs defined by prevailing methods where the c-axis of hard and soft grains are greater than 50° apart from each other. This feature is not useful when trying to capture the basal subfeatures of harder MTRs defined by prevailing methods that appear to work cooperatively, where the difference in c-axis is more subtle. Theoretically, a smooth enough orientation gradient exists that all the possible c-axis orientations could be grouped into one MTR. None of the explored tolerance angles resulted in the definition of these separate regions within the larger MTR defined by prevailing methods, as shown in Figure 5.1. At larger tolerance between 4° and 10°, the main MTR defined by prevailing methods remains with a few stray grains excluded. At lower misorientation tolerances from 2°-3°, the MTR defined by prevailing methods disappears and the orientation map is divided into many smaller features of a few grains each; these smaller features do not match the regions that act cooperatively to allow for basal slip transfer.

Even if a tolerance angle segmentation works for a particular microstructure under load shedding and dwell fatigue, this does not indicate applicability to other microstructures or different loading conditions. Additionally, metrics for determining segmentation quality are elusive. In this work, the segmentation map was compared to the regions of grains acting cooperatively for slip transfer in Ti-6242 under dwell fatigue loading. The aim was to match the boundaries of the slip traces with the boundaries of the MTRs and segment the regions of cooperative grains. When comparing the results in Figure 5.1 and Figure 5.2, it is evident that areas of the microstructure are subdivided differently when trying to capture the true cooperative structural unit; changing the misorientation tolerance improves and tightens the boundary of some MTRs closer to the long-range slip features, whereas other MTRs are lost and broken up into sections smaller than the slip features.

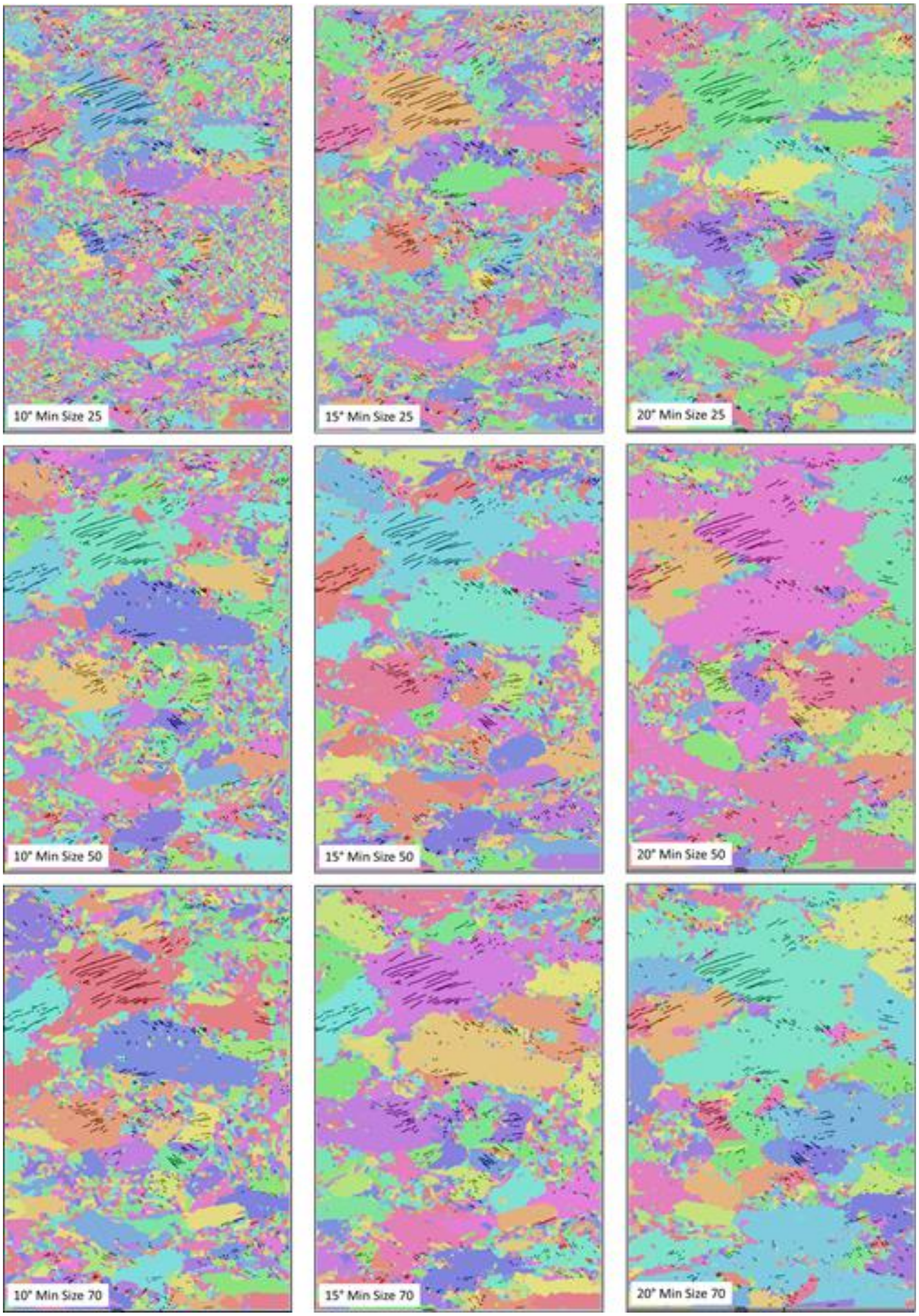

Figure 5.1: MTR segmentations of the full gauge of Sample C (the 200°C test case) made by varying the misorientation parameter from 20-10 degrees and minimum feature size from 25-70 cells.

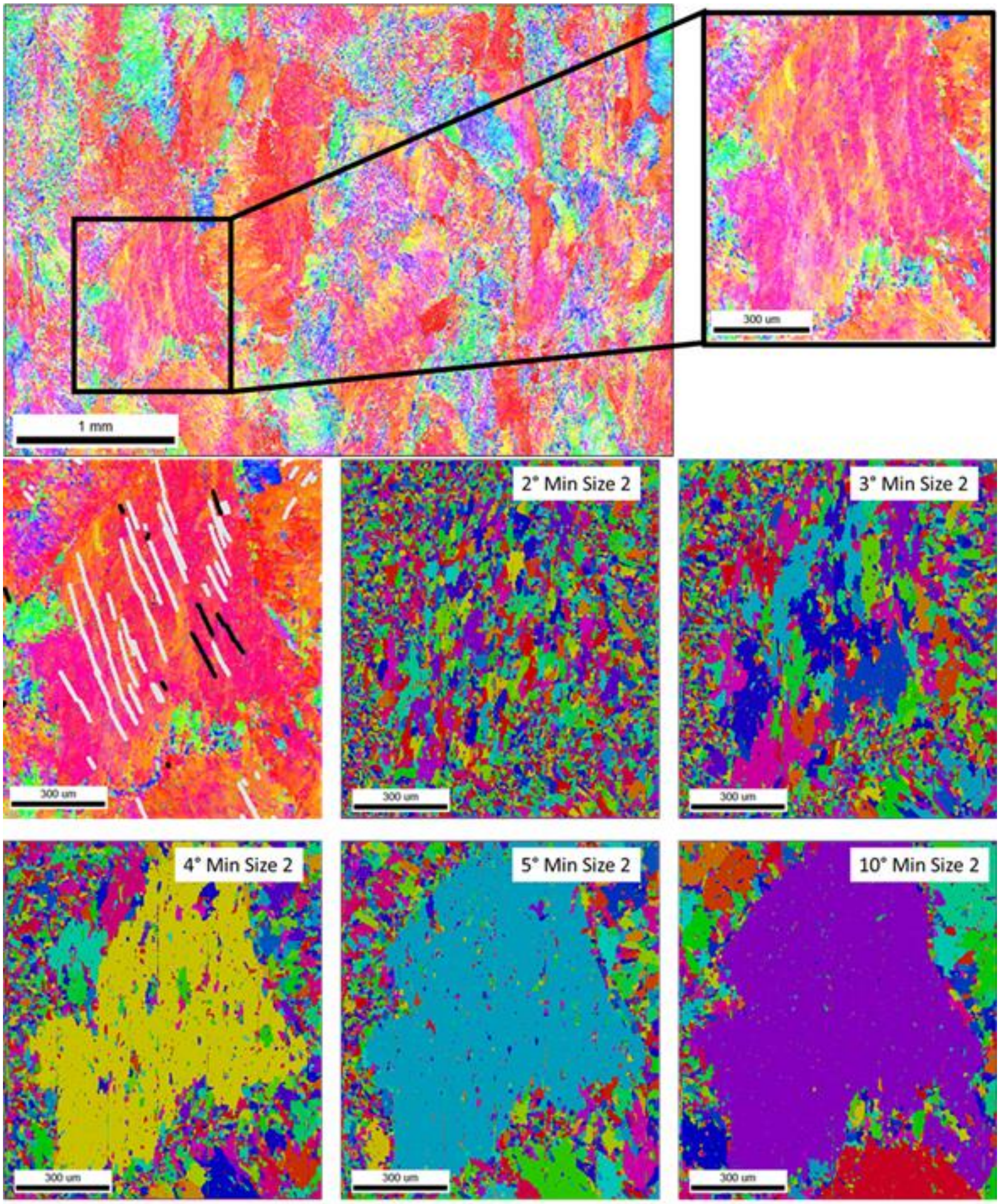

Figure 5.2: Subsection of Sample C microstructure map showing what is categorized as a single MTR but containing clear separate regions. Vertical bands of slightly less hard grains exist in a region surrounded by harder grains. The slip traces appear to exist within the bands of slightly less hard grains. Segmentations allowing for a misorientation from 2°-10° show that the selected misorientation tolerance captures the regions appropriately.

5.2.2 C-axis Definition of Hard and Soft

The modified Stroh model and CPFE models described in section 2.3.1 investigate the behavior of hard and soft microstructural features. The orientation of the c-axis relative to the loading direction dictates whether the region is easy or difficult to deform. For a soft grain in both the modified Stroh model and CPFE, the c-axis is considered nearly perpendicular to the loading direction. While the CPFE models consider the various slip strengths, strain sensitivities, and deformation properties of the modeled crystallography, most modeled soft regions are prismatically soft with their c-axis near perpendicular to the loading direction [14], [15]. Additionally, experimental materials for load shedding and dwell investigations are processed to intentionally produce prismatically soft regions [61], [90]. When studying sub regions and grains of interest in a larger test sample, grains with their c-axis near perpendicular to the loading direction are specifically selected. While excellent progress has been made through these models and experimental studies on prismatic soft grains, the work presented in Chapter 4 suggests that the basally soft grains should also be included in these models, and that the basally soft regions may indeed be the weakest microstructural links for early crack nucleation.

The exact bounds on how much the c-axis can deviate from the loading direction have not been standardized when defining hard and soft regions. One approach to define this tolerance angle is informed by fractography work by Sinha et al. [9] When examining the fracture surface of dwell loaded Ti-6242, it was found that the faceted regions of crack propagation on the fracture surface occurred in grains with their c-axis within ± 15° of the loading direction [5], [6]. When compared to the Schmid factor calculation in equation 2 in section 2.2.3, this corresponds with the high basal stress on the hard grain within that range.

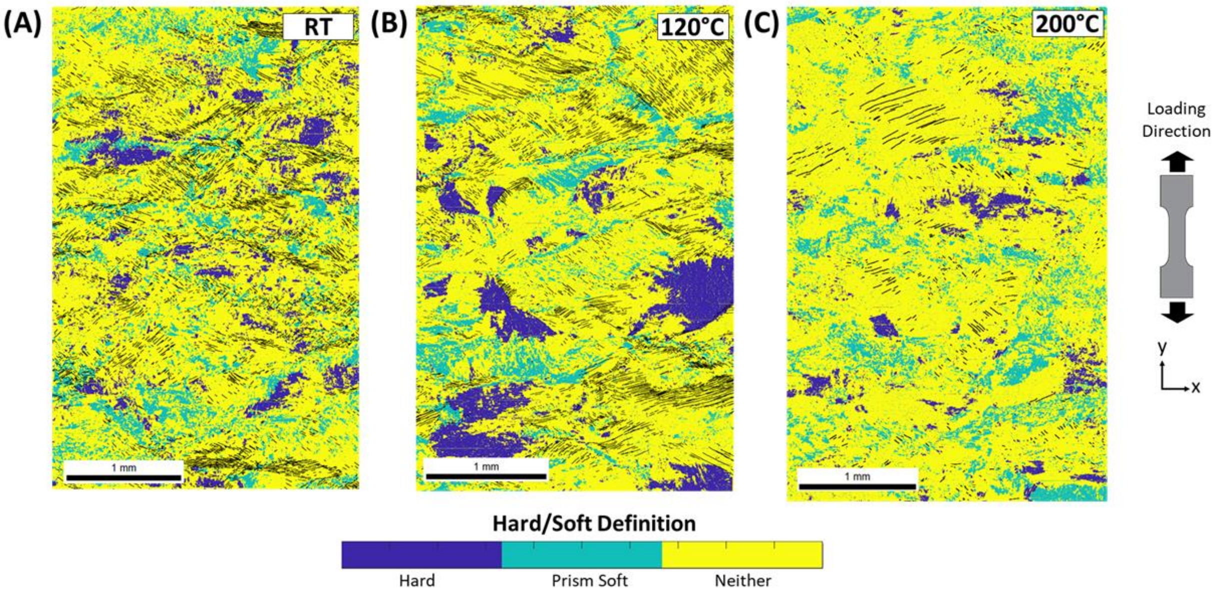

Figure 5.3: The map is colored to define hard, soft, and neither regions, with the slip traces after 200 cycles imposed in black. Prismatic soft regions are defined as having a c-axis misalignment of 75-90° relative to loading direction, while hard regions are defined as having their c-axis within 0-15° of the loading direction. Long range slip activity did not occur in soft regions following this definition.

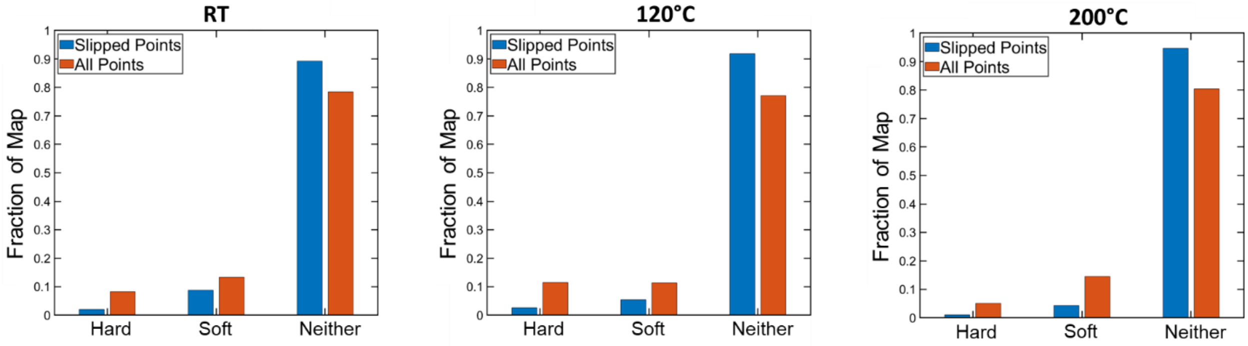

Figure 5.4: Normalized number of slipped points and all points in regions defined as hard, soft, and neither for each whole gauge sample after 200 dwell cycles. Over 95% of all slipped points occurred in regions defined as neither hard nor soft, in agreement with the dominant basal slip activity identified in section 4.2.3.

Another approach to define the boundary conditions for hard and soft grains is presented by Bantounas et al. [105] on high-cycle fatigue of Ti-6Al-4V. In Bantounas's work, they determined the most easily activated slip system and created a "normalized" Schmid factor, given by

$$m' = m \times \left(\tau_{min}/\tau_{\langle uvwt\rangle\{hkil\}}\right) \tag{3}$$

Where m is the traditionally defined Schmid factor from equation (2) , m' is the normalized Schmid factor, and $\tau_{min}/\tau_{\langle uvwt\rangle\{hkil\}}$ is the ratio of the CRSS of a given slip system ($\tau_{\langle uvwt\rangle\{hkil\}}$) to the CRSS of the easiest activated slip system (τ_{min}), known to be basal or prismatic <a> slip for near-alpha titanium alloys. This equation relates the Schmid factor with the CRSS and models the active slip system as a function of the misorientation between the loading direction and the c-axis of the grain. The normalized Schmid factor for each slip system versus the angle between the loading direction and the c-axis of the grain is plotted in Figure 5.5. The intersection of these curves indicates three distinct regions where each slip system is dominant. When the c-axis of a grain is between 0-10° misaligned from the loading direction, pyramidal slip dominates. From 10-66.67° basal slip is the most likely, and from 66.67-90° misalignment prismatic slip dominates. From the classic modified Stroh model described in section 2.2.3, hard grains are oriented for pyramidal slip and soft grains are likely aligned for prismatic slip [5]. Therefore, it is reasonable to use the misorientation ranges defined by Bantounas et al. [105] to set an even tighter bound on the definitions of hard and soft grains.

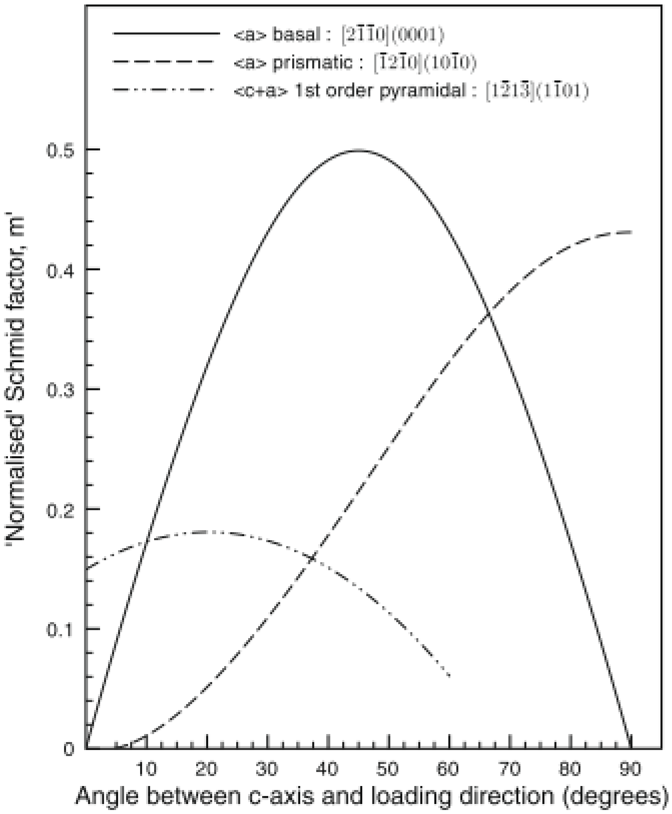

Figure 5.5: Graph of "normalized" Schmid factor vs. the angle between the c-axis and the loading direction for basal and prismatic <a> slip and first order pyramidal <c+a> slip. [105]

When using the often-cited definition of hard (c-axis 0-15° relative to loading direction) and soft grains (c-axis 75-90° relative to loading direction), the long-range slip activity observed in this work did not occur in prismatically-soft regions, and the location of hard regions did not correlate to the spatial distribution of long-range slip activity. Extending the definition of soft regions to grains with their c-axis misaligned by 66.7-90° to the loading direction also did not change this result. Rather, slip primarily occurred through grains with their c-axis 30°-45° aligned to the loading direction, as discussed in section 4.2.3. Figure 5.3 and Figure 5.6 show the orientation information obtained from EBSD for each large FOV sample binned into either hard, soft or neither categories depending on the c-axis of each point relative to the loading direction by the ±15° misorientation tolerance or the angle bounds suggested by Bantounas et al. [105] . The orientation maps are colored according to these categorizations. The segmented long-range slip traces after 200 dwell cycles are superimposed onto each color map to highlight the locations where long-range slip occurred. Whether the points involved in slip activity are hard, soft, or neither are tallied and displayed in a bar graph in Figure 5.4 and Figure 5.7. For both c-axis definition schemes, over 95% of all slipped points occur in regions defined as neither hard nor soft. Instead slip occurs in regions best aligned for basal slip according to the predictions of the "normalized" Schmid factor. This agrees with the trend of dominant basal slip activity in regions with a high basal Schmid factor as identified in section 4.2.3.

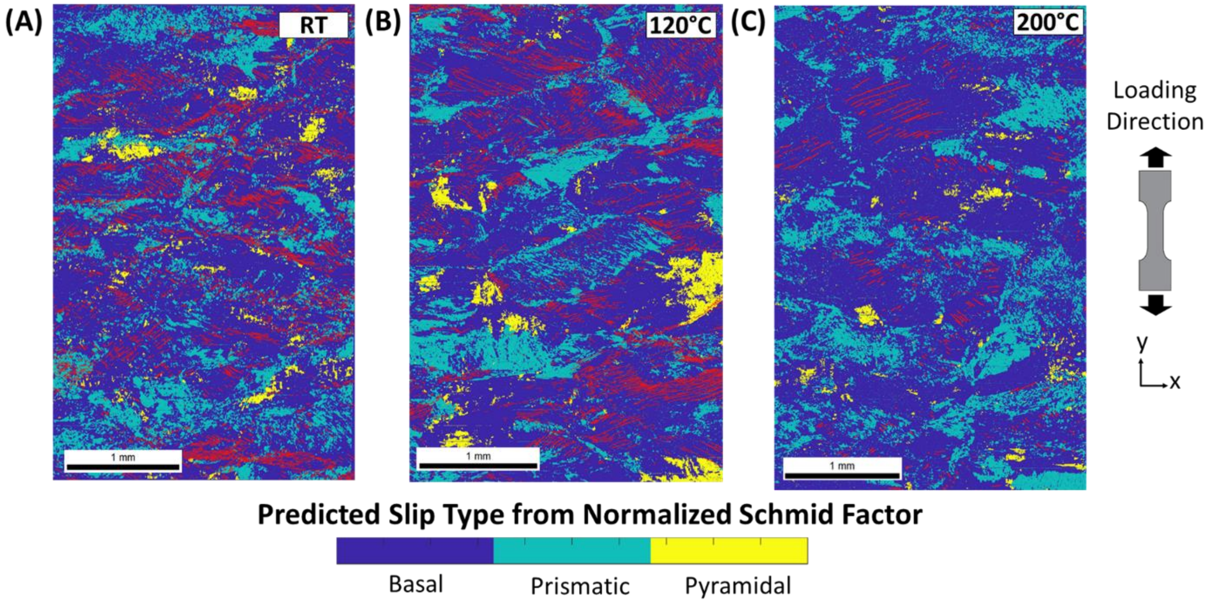

Figure 5.6: Long range slip occurs in regions where basal slip has the highest normalized Schmid factor, from the Bantounas [105] work. This aligns with the known high basal Schmid activity, but it does not align with what would be traditionally defined as hard pyramidal regions and soft prismatic regions.

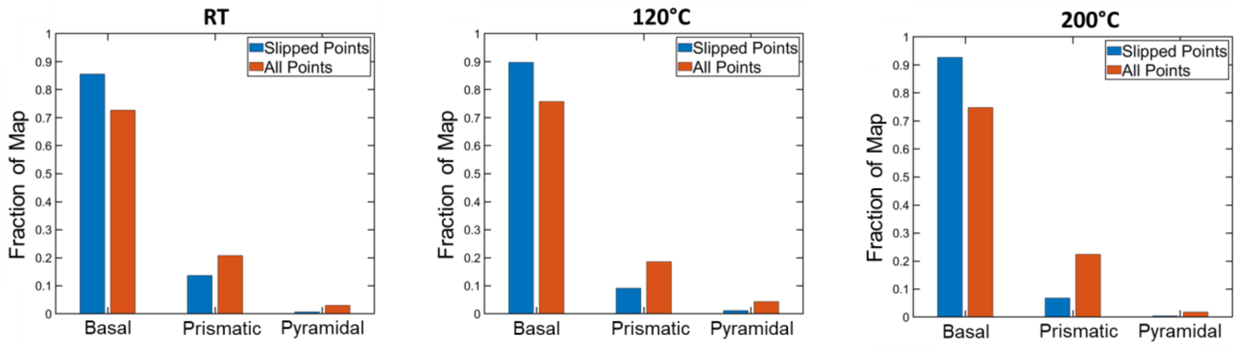

Figure 5.7: Normalized number of slipped points and all points in regions well oriented for basal, prismatic, and pyramidal slip activity according to the normalized Schmid factor [105] for each whole gauge sample after 200 dwell cycles. Over 90% of all slipped points occur in regions defined as basal, which is in agreement with the trend of dominant basal slip activity identified in section 4.2.3.

5.3 Strength-to-Stiffness

For Ti-6242 under dwell fatigue loading, the strength-to-stiffness ratio strongly indicates which grains will act cooperatively and allow long-range slip. Wong and Dawson [106] analyzed the results of a CPFE simulation and showed that the directional strength to the directional stiffness ratio correlated well with the order in which crystals yielded under uniaxial loading in low strain-regimes (i.e. lower values of strength-to-stiffness will yield first). They found that this strength-to-stiffness ratio correlates significantly better with the deformation of grains than strength alone. Both the strength and material stiffness are individually anisotropic for the alpha phase of Ti-6242, and therefore the strength-to-stiffness ratio is orientation dependent as well.

The way in which the strength-to-stiffness ratio predicts the order of yielding is described by Wong and Dawson using a simple conceptual example. Consider two masses loaded in parallel as illustrated in Figure 5.8. The two masses will undergo the same amount of deformation upon loading (isostrain). Each mass has its own effective modulus and yield strength. When considering only their yield strength, one would expect the mass with the lower yield strength to fail first. For this mass pair though, the mass with the larger yield strength also has a larger elastic modulus and will reach its yield strength at a smaller total strain than the mass with the lower modulus and yield strength, as illustrated from the stress strain curve in Figure 5.8. In this case, the mass with the larger yield strength and elastic modulus will yield first. The strength-to-stiffness ratio describes the order in which these masses would fail better than the individual yield strength of each mass. This simple example of masses can be extrapolated to other situations where different objects experience similar loads, like the grains in a polycrystal under uniaxial loading conditions [106]. In a polycrystal, this is clearly a simplification of the behavior as microstructural interactions are important, but the compatibility requirements of the isostrain condition can still be useful to explore basic relationships between grains.

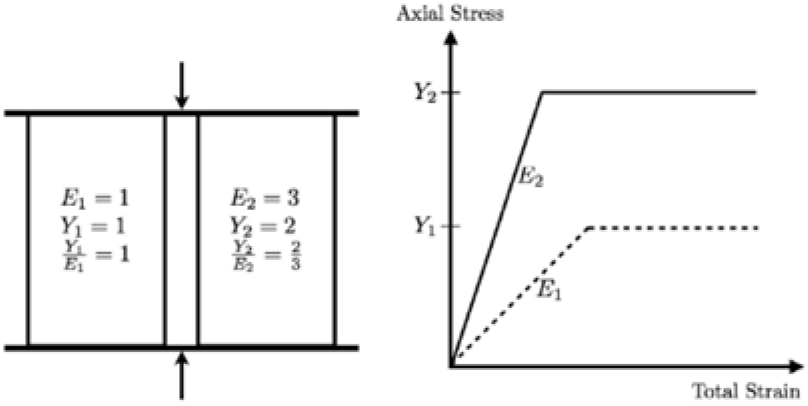

Figure 5.8: Illustration of two masses loaded in parallel under isostrain conditions. If they behave in a perfect elastic-plastic fashion, the material with a higher yield strength will fail first due to its larger elastic modulus.[107]

5.3.1 Elastic Modulus

Material stiffness is described as the inverse of the elastic modulus. The orientation dependence of the effective elastic modulus is described in section 2.2.2. The directional effective elastic modulus is calculated using the following equation

$$\frac{1}{E_{dir}} = S_{11}\sin^4\theta + S_{33}\cos^4\theta + (2S_{13} + S_{44})\cos^2\theta\sin^2\theta \tag{4}$$

Where θ is the angle between the c-axis of the crystal and the loading direction, E_{dir} is the directional effective elastic modulus, and S_{ij} are components of the symmetry reduced compliance tensor in the crystal reference frame. [109]. The material stiffness matrix for alpha phase titanium used in this formulation is the inverse of the compliance matrix reconstructed by Kim et al. from line-focus acoustic microscopy of Ti-6242 single colonies [110].

$$C_{ij} = S_{ij}^{-1} = \begin{bmatrix} 141 & 76.9 & 57.9 & 0 & 0 & 0 \\ 76.9 & 141 & 57.9 & 0 & 0 & 0 \\ 57.9 & 57.9 & 163 & 0 & 0 & 0 \\ 0 & 0 & 0 & 48.7 & 0 & 0 \\ 0 & 0 & 0 & 0 & 48.7 & 0 \\ 0 & 0 & 0 & 0 & 0 & 32.05 \end{bmatrix} GPa$$

Individually, the material stiffness metric appears to describe regions of cooperative slip in Ti-6242 under dwell loading. The effective modulus relative to loading direction from equation 4 is plotted in section 2.2.2. Figure 5.9 shows the effective modulus maps calculated for each point in the orientation maps for Sample A, B, and C, the full gauge samples tested at RT, 120°C and 200°C, respectively. The distribution of the elastic modulus for the entire map versus the elastic modulus of points that a slip trace traverses is shown in Figure 5.10. From these plots, it is clear that most of the slip traces traverse through regions with an elastic modulus between 115-125 MPa. These are neither the stiffest nor the most compliant regions, but rather correlate well to the grain orientations that would deform by basal slip, a key factor highlighted in Chapter 4. About 10% of the map has an effective modulus below 95 GPa and ~7% of the map has an effective modulus above 130 GPa. These steep distribution tails are due to the cosine relationship in the effective modulus. For θ values between 0°-20, the directional elastic modulus is above 130 MPa, and for θ values between 80°-90° the elastic modulus is less than 95 GPa. The rate of change of the effective modulus of θ values from 20-80° is significantly greater, as seen in Figure 2.6.

The regions that accommodate slip also appear to be surrounded by regions with a stiffer elastic modulus. This is not to say that the less stiff slipped regions are surrounded by regions with the stiffest modulus on an absolute scale, but rather that there appears to be a small relative difference of approximately 5 GPa between the material stiffness of the two regions. The effective local modulus map for the same test case area from Sample C used in the C-axis variation exploration is shown in Figure 5.11. This example shows the clear regions of slipped lower modulus material near stiffer unslipped material. This same trend visually appears in the other regions of the full gauge sections, where the effective modulus captures the subfeatures of MTRs defined by prevailing methods that are missed by c-axis segmentation methods alone.

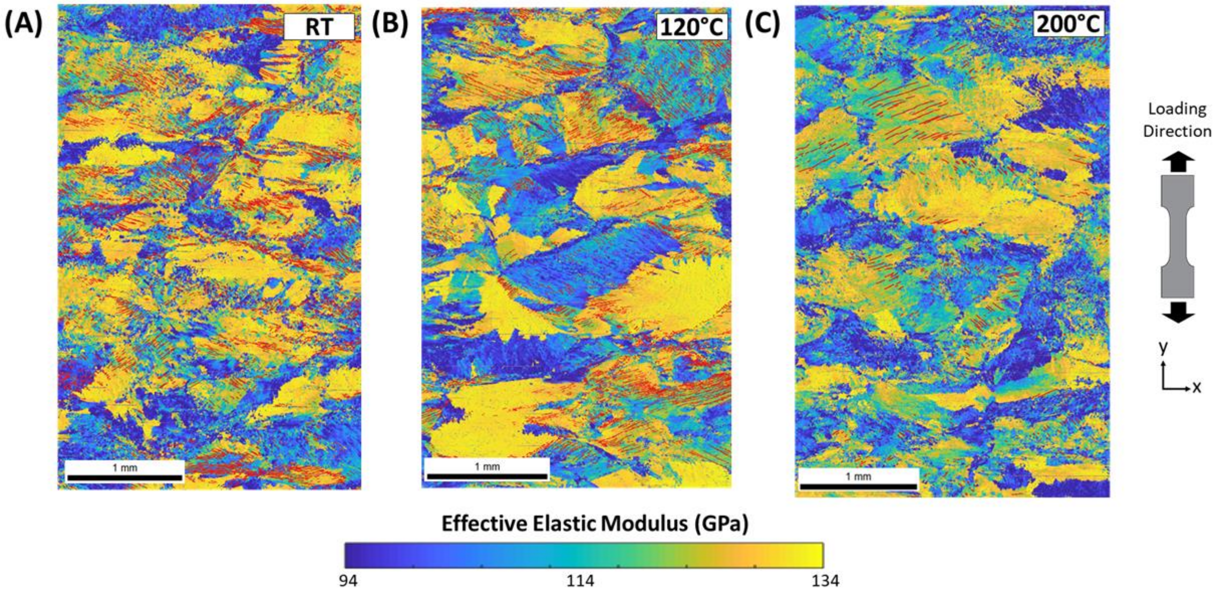

Figure 5.9: Effective modulus map for Samples A-C, which are the full gauge samples tested at RT, 120°C, and 200°C, respectively. The slip traces after 200 dwell cycles are superimposed in red on the effective modulus map. The effective modulus appears to highlight the sub features of MTRs that act cooperatively.

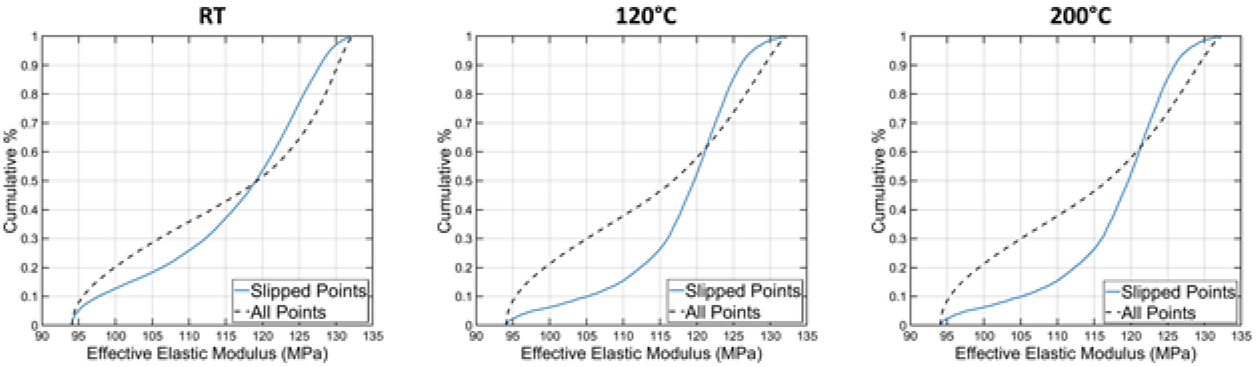

Figure 5.10: CDF plots of the effective modulus of slipped and unslipped points in the effective modulus map. At all temperatures, most of the slipped points are not the least stiff points, but rather most of the slipped points have an effective modulus between 115-125 MPa.

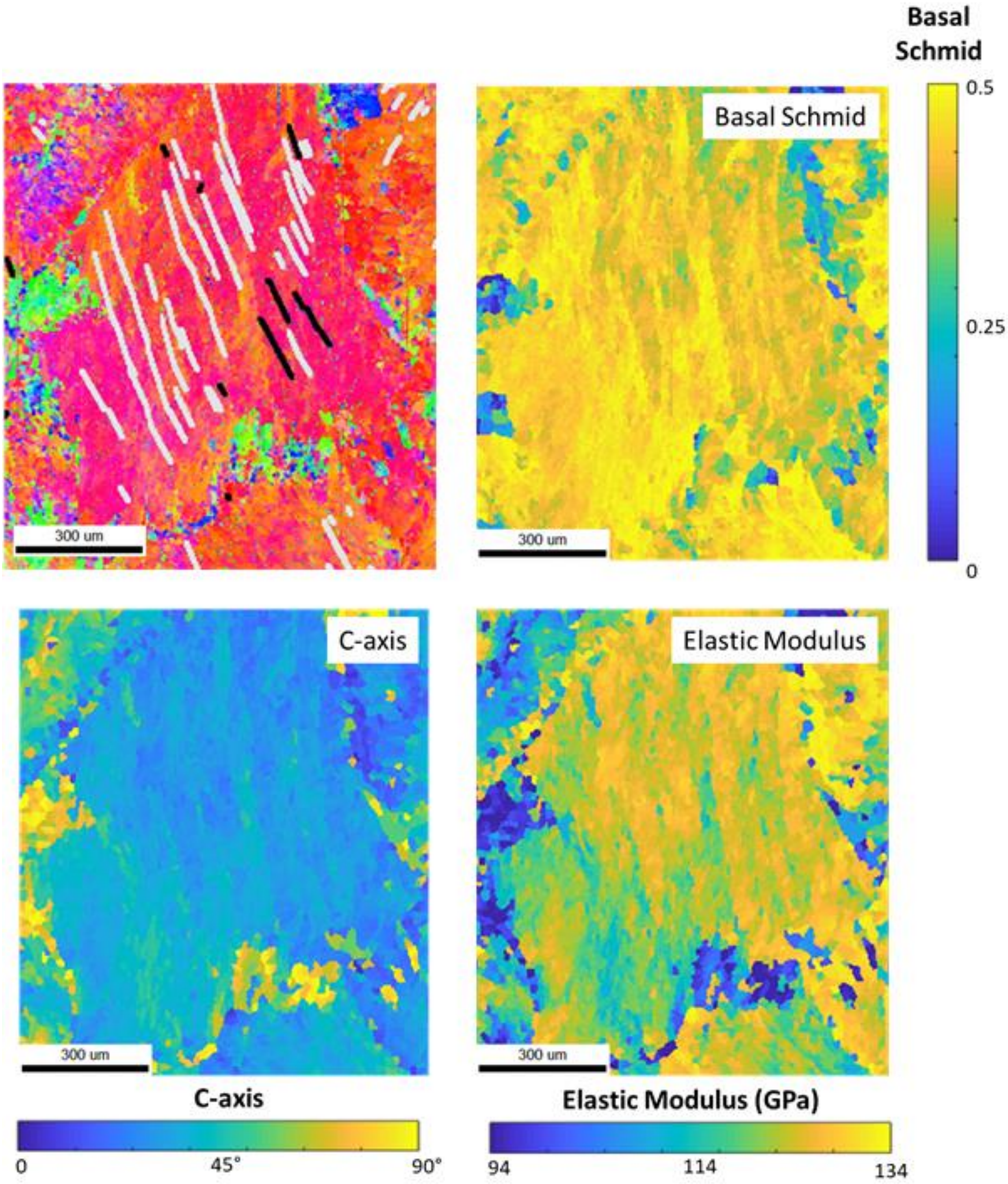

Figure 5.11: Subsection of the 200°C full gauge test. The c-axis orientation relative to loading does not highlight the individual sub-features of the classically defined MTR, while the effective elastic modulus and basal Schmid factor maps clearly highlight these cooperative regions.

5.3.2 Strength – The Schmid Factor and the Taylor Factor

The Schmid and Taylor factors are most commonly used to describe a grain's resistance to deformation under uniaxial loading. Both factors relate the macroscopic yield stress to the CRSS on a slip system. The Schmid factor assumes isostress conditions and satisfies equilibrium, while the Taylor factor assumes isostrain behavior and satisfies compatibility. The Schmid factor is described in section 2.2.3 and relates the crystallographic orientation to the propensity for slip on an individual slip system, while the Taylor factor considers the summation of deformation on all active systems. The latter is most commonly used in interpreting microstructural phenomena during high temperature materials processing.

In this study on dwell fatigue, basal slip was more active than any other type of slip. Therefore, in the absence of detailed finite element models, which would need to include the full three-dimensional microstructure for reliability [111], [112], the use of the basal Schmid factor is examined as a strength metric. The relationship between the basal Schmid factor and slip activity during dwell fatigue at each temperature is discussed in detail in Chapter 4, and Figure 4.2 shows the basal Schmid factor for each point of the orientation maps. The basal Schmid factor is clearly correlated to cooperative slip and can likely be used as a metric to define regions well aligned for cooperative slip.

When using the Schmid factor to define the strength parameter, each individual slip system has its own strength. While the Schmid factor works well for a single crystal, in polycrystals deformation is accommodated by slip on more than one slip system at a time to maintain material continuity. In Wong and Dawson's work [106], they found that using the Schmid factor over-predicted the final strength-to-stiffness value, and therefore proposed averaging the strength over a specific orientation and using the Taylor factor.

The Taylor model considers each of the possible active slip systems that could be active for a specific orientation. The Taylor factor specifically details the strength of a grain by quantifying the magnitude of the slip system shearing rates relative to the effective strain rate experienced by the crystal while minimizing the amount of expended work. Under uniaxial tension, the Taylor factor is expressed by

$$M_{dir} = \sum_{s} \frac{y^{(s)}}{\varepsilon} = \frac{\sigma}{\tau_c} \tag{5}$$

where M_{dir} is the Taylor factor, $\gamma^{(s)}$ is the slip magnitude of the respective slip plane s, ε uniaxial strain, σ is the uniaxial stress, and τ_c is denotes the critical resolved shear stress. The Taylor factor is dependent on both the orientation of the crystal and the applied deformation. Large Taylor factor values imply that deformation would require a significant amount of slip and work, while small Taylor factors imply that deformation could be accommodated efficiently on fewer slip systems resulting in less plastic work. Taylor factor maps produced from the full gauge orientation maps of sample A, B, and C are shown in Figure 5.12. They were produced using the OIM Taylor factor tool under uniaxial tension with a basal: prismatic: pyramidal CRSS ratio of 1:0.7:3.

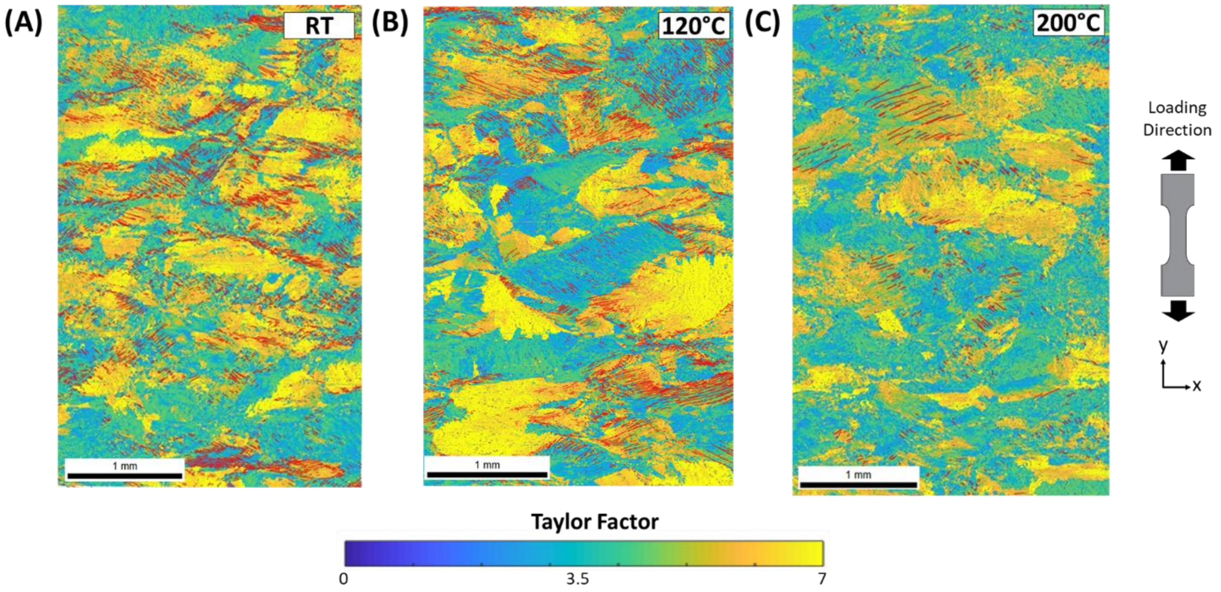

Figure 5.12: Taylor factor maps showing that there is not a link between the Taylor factor and locations of slip activity.

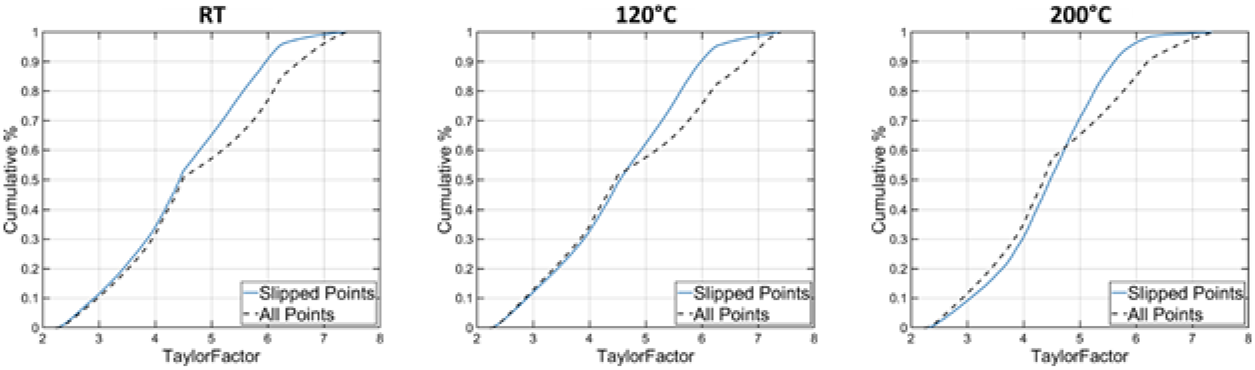

Figure 5.13: Cumulative distribution function of the Taylor factor for all the points in the orientation map and for all the slipped points of the orientation map. Regions with a low Taylor factor are not preferentially slipping, indicating that this calculation for the Taylor factor is not a good indicator for the onset of slip in Ti-6242 under dwell loading. Additionally, due to the texture of the overall behavior, there is an absence of points in the microstructure with a Taylor factor between 4.5 and 5.2.

The Taylor factor does not appear to be an appropriate strength metric to determine the onset of slip in Ti-6242 under dwell loading. While the Taylor factor highlights some of the groups of grains that act cooperatively, there is no relationship between the value of Taylor factor and locations of slip activity. There is no significant difference between the Taylor factor distribution for the entire gauge section and the slipped points. While less than 10% of slipped points have a Taylor factor above 6 for each temperature, there is a relatively even distribution of Taylor factors for slipped points below 6.

For the entire gauge section of each sample, there is an absence of points with a Taylor factor around 5. Overall, every temperature only has approximately 10% of points with a Taylor factor between 4.5 and 5.2. This is likely linked to the texture of the material, which has moderate alignment of {0001} poles with the loading direction. It is important to note that the value of the Taylor factor is more qualitative, as a fully quantitative Taylor factor would require exact measurements of the CRSS for each slip system. The exact quantification of various slip systems in α-Ti is an active field of research and beyond the scope of this study [7], [25], [38], [113]–[115]. Thus, this estimate of the Taylor factor is assumed to be a reasonable estimate of the true Taylor factor, even if the exact measurements of the CRSS each slip system in this material would change the Taylor factor values.

5.3.3 Strength-to-Stiffness Ratio

From looking at the individual maps of the orientation-dependent elastic modulus, basal Schmid factor, and Taylor factor, we find that the basal Schmid factor and elastic modulus provide a better representation and differentiation of regions that act cooperatively than either the Taylor factor approximations or c-axis descriptions. We compute the strength-to-stiffness ratio for both the Schmid factor and the Taylor factor using the following equations:

$$r_{dir} = \frac{\frac{1}{m_{dir}}}{E_{dir}} \tag{6}$$

Or

$$r_{dir} = \frac{M_{dir}}{E_{dir}} \tag{7}$$

Where r_{dir} is the directional strength-to-stiffness ratio, m_{dir} is the directional Schmid factor, M_{dir} is the directional Taylor factor, and E_{dir} is the directional elastic modulus. A low strength-to-stiffness ratio implies that a region is well aligned for early and easy slip activity, while a high strength-to-stiffness ratio implies that a region is less likely to experience plastic deformation. The relative values of the strength-to-stiffness ratio have been shown to align well with the order in which regions will undergo plastic deformation and slip [106], [107]. Maps and distributions for each strength-to-stiffness parameter is shown in Figure 5.14 and Figure 5.16.

The Taylor factor as calculated here does not provide an accurate representation of a grain's proclivity to slip under dwell fatigue loading in Ti-6242. At all tested temperatures, there is no clear link between regions of slip activity and the strength-to-stiffness ratio calculated using the Taylor factor. As seen in the distribution plots of the Taylor factor strength-to-stiffness in Figure 5.15, there is no significant difference between the distribution of Taylor strength-to-stiffness ratios of the entire gauge section and the points that were involved in slip activity. There is no link between a low Taylor strength-to-stiffness ratio and slip activity. Most slipped points do not have a low Taylor strength-to-stiffness ratio. While less than 5% of slipped points have a Taylor strength-to-stiffness factor over 0.045, over 40% of the slipped points have a Taylor strength-to-stiffness ratio between 0.035 and 0.045.

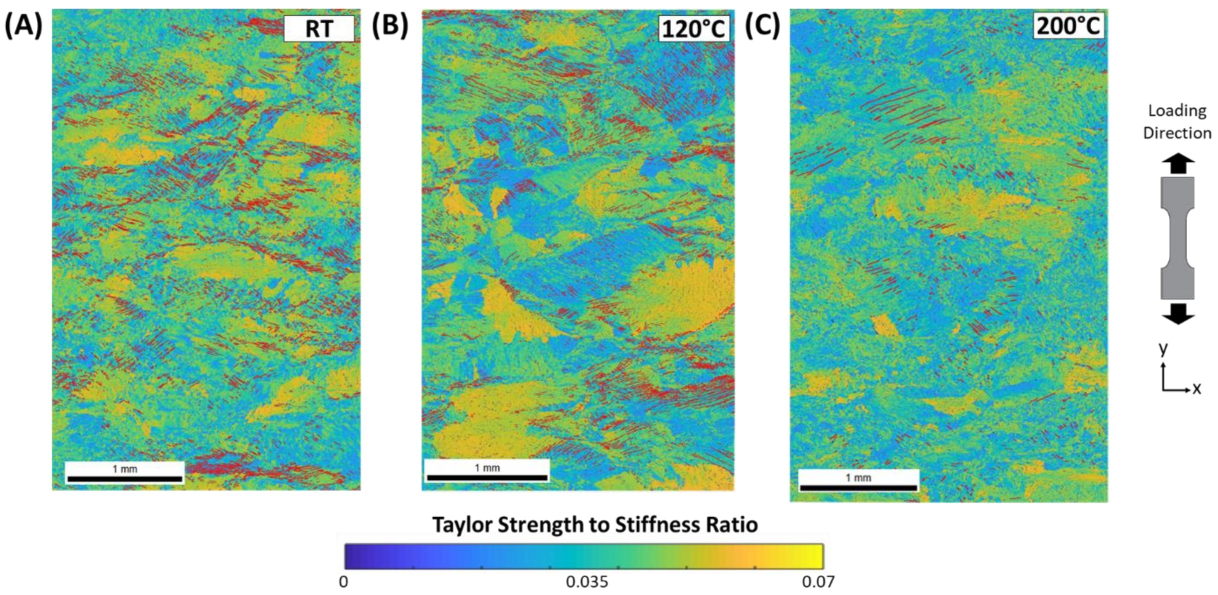

Figure 5.14: Map of Taylor strength-to-stiffness ratio of samples A, B and C with slip traces after 200 dwell cycles superimposed on top in black. There is no link between the strength-to-stiffness ratio calculated using the Taylor factor for strength and the locations of slip activity.

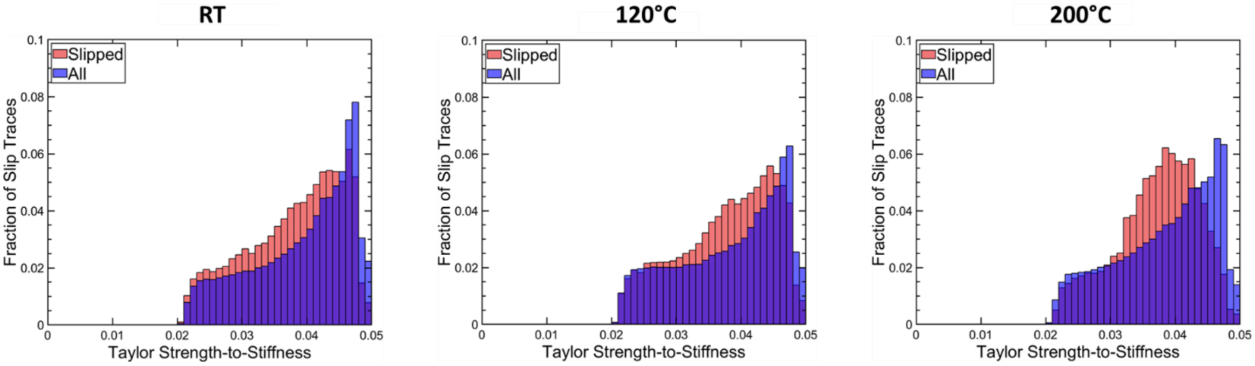

Figure 5.15: Histogram of the Taylor strength-to-stiffness ratio for all slipped points vs. all points in the orientation map at RT, 120°C, and 200°C. There is no apparent correlation between the strength to stiffness ratio calculated using the Taylor factor for strength and the locations of slip activity.

At all tested temperatures, there was a strong correlation between grains that underwent plastic deformation and grains with a low basal Schmid strength-to-stiffness ratio. The strength-to-stiffness maps in Figure 5.16 show that slip primarily exists in regions with a low basal strength-to-stiffness ratio. The basal strength-to-stiffness is bound between the values of 0.0151 and infinity, as bound by possible values of the basal Schmid factor and the effective elastic modulus. Over 85% of all the slipped points have a basal strength-to-stiffness ratio below 0.03 for all temperatures, as seen in the distribution plots in Figure 5.17. The original strength-to-stiffness studies by Wong and Dawson were on FCC materials, and due to the high degree of single crystal stiffness anisotropy present in HCP materials, the Schmid factor (isostress assumption) over-predicts the strength-to-stiffness ratio when compared to the Taylor factor (isostrain assumption). In HCP titanium alloys, the relatively low amount of elastic anisotropy of the alpha phase allows for a reasonable Schmid factor isostress assumption as demonstrated by Kasemer et al. [107].

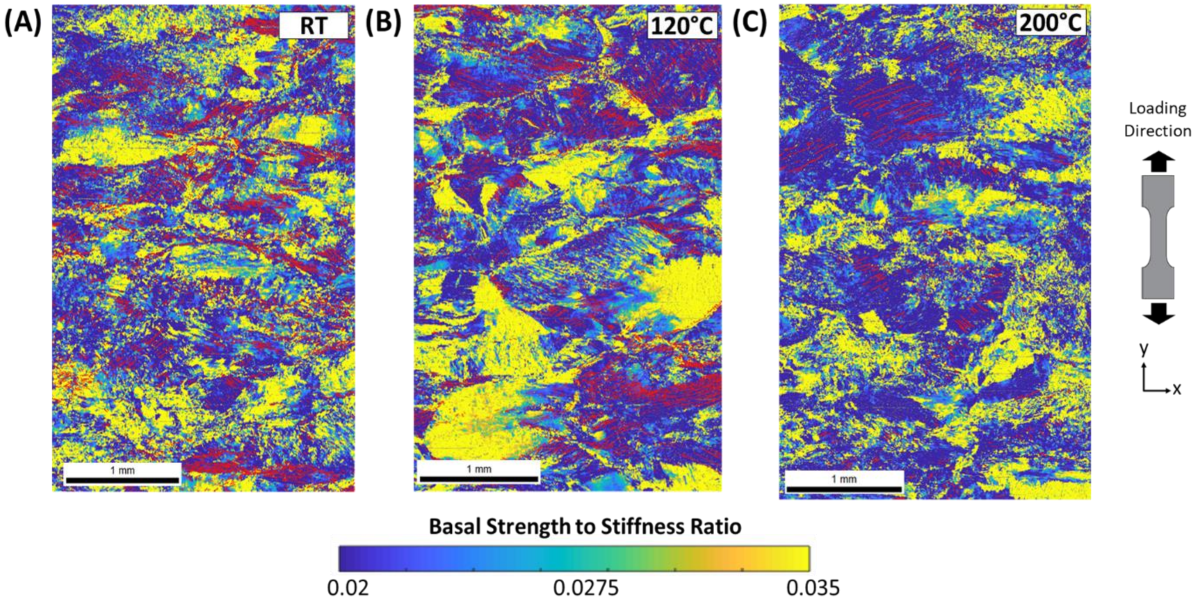

Figure 5.16: Map of basal Schmid factor strength-to-stiffness ratio of samples A, B, and C with slip traces after 200 dwell cycles superimposed on the maps in white. There is a clear correlation

between locations of slip activity and a low strength-to-stiffness ratio calculated with the basal Schmid factor as the strength parameter.

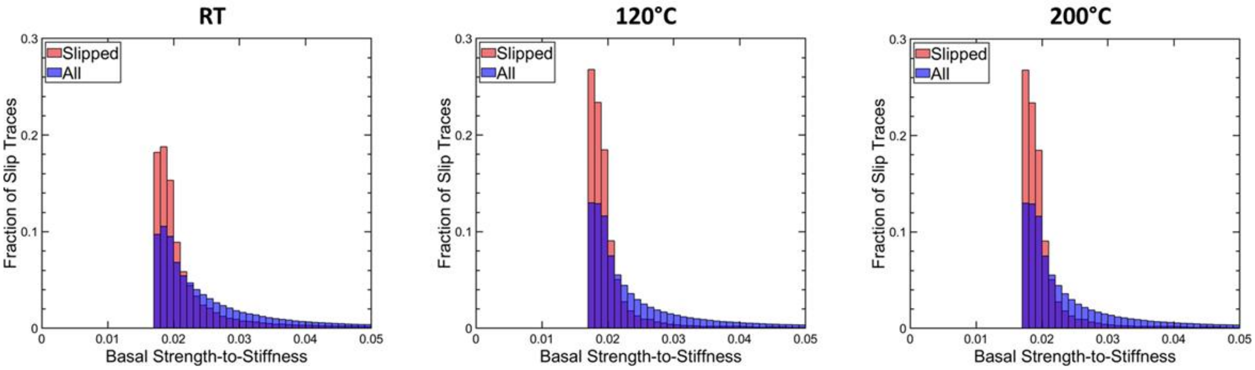

Figure 5.17: Histogram of the basal Schmid strength-to-stiffness ratio for all the points in the orientation map and for all the slipped points in the orientation map for Samples A, B, and C. There is a clear correlation between locations of slip activity and the strength to stiffness ratio calculated with the basal Schmid factor as the strength parameter.

To confirm that the basal Schmid factor is reasonable strength metric, the prismatic strength-to-stiffness ratio was investigated following the same approach as the basal strength-to-stiffness ratio described above. At all tested temperatures, there was no relationship between grains that underwent plastic deformation and grains with a low prismatic Schmid strength-to-stiffness ratio (Figure 5.18 and Figure 5.19). The prismatic Schmid factor was used as the strength metric in the strength-to-stiffness ratio to further investigate what the best strength metric is for identification of cooperative slip regions in Ti-6242. While prismatic slip is often reported as being the most easily activated slip system and typically used as the representative "soft grain" orientation in the modified Stroh model and when setting up parametric CPFE models, it is not indicative of regions that undergo cooperative slip under dwell fatigue loading in Ti-6242. The lack of plastic slip activity in regions with a low prismatic strength-to-stiffness ratio also corroborates the lack of prismatic slip activity reported in Chapter 4 at all temperatures and dwell cycles.

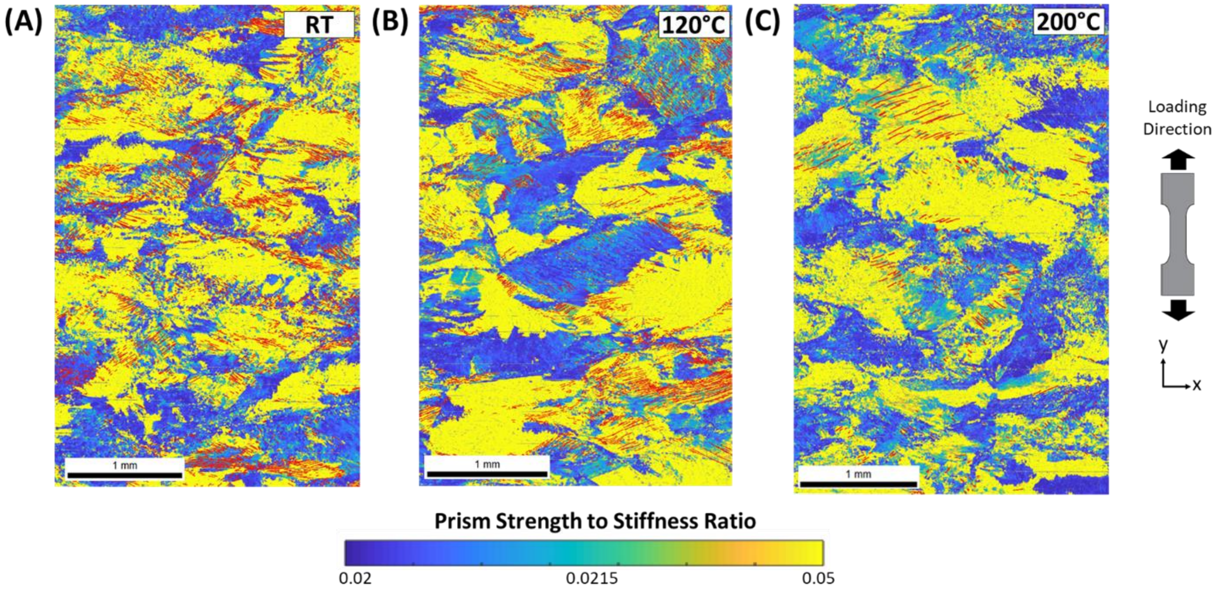

Figure 5.18: Map of prismatic strength-to-stiffness ratio of Samples A, B, and C with slip traces after 200 dwell cycles superimposed on top in black. There is no link between the strength-to-stiffness ratio calculated using the prismatic Schmid factor for strength and the locations of slip activity.

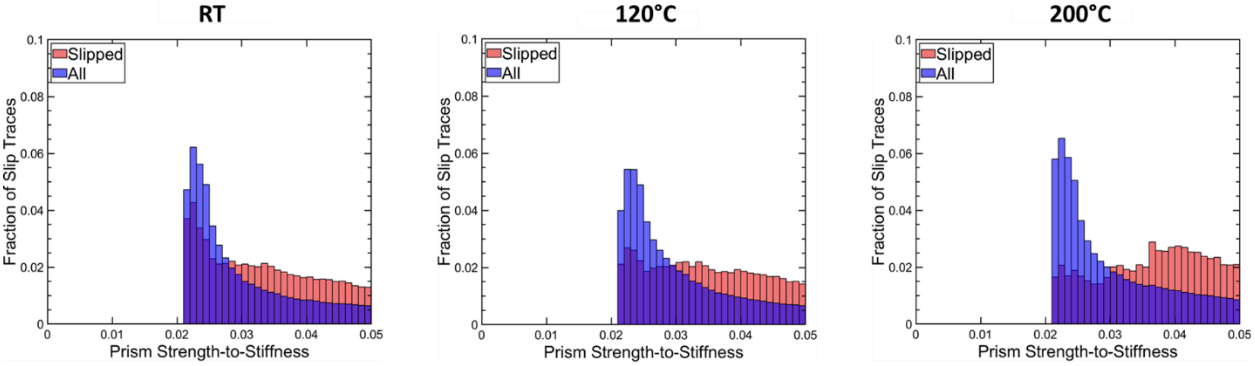

Figure 5.19: Histogram of the prismatic Schmid strength-to-stiffness ratio for all the points in the orientation map and for all the slipped points in the orientation map for Samples A, B, and C. There is no relationship between locations of slip activity and the strength to stiffness ratio calculated with the prismatic Schmid factor as the strength parameter. This is in agreement with the lack of prismatic slip activity observed at all temperatures and cycle counts previously reported in Chapter 4.

There is a clear correlation between locations of slip activity and regions with a low strength-to-stiffness ratio calculated with the basal Schmid factor as the strength parameter. The relationship between the strength-to-stiffness ratio and slip activity has been previously demonstrated for HCP materials in simulations and experimental work by Kasemer et al. [107] on Ti-6-4 under uniaxial tension. They used a parallelized CPFE model using a normalized Schmid factor to investigate the influence of the initial slip strengths on the deformation response of an alpha-phase polycrystal. In the model of Kasemer et al. [107], the grain orientations of the simulated polycrystal were selected to mimic the orientation distribution function of an experimentally tested sample of microtextured Ti-6-4 under uniaxial tension by Echlin et al. [90]. The grain orientations in the modeled polycrystals were selected to match the ODF of the experimentally tested sample. The study simulated both a microtextured and non-microtextured polycrystal by differing the spatial location of the grains while maintaining the same global ODF. The CRSS of the basal, prismatic, and pyramidal <a> slip families and which slip family is the weakest are topics of debate within the titanium community. Different studies report different CRSS and relative strengths. Kasemer et al. [107] explored three different sets of CRSS parameters from literature in their simulation. For both microtextured and non-microtextured simulations, Kasemer et al. [107] found that the best agreement between the model and the experimental results by using weak basal family strength with a slightly higher prismatic family strength at 1.2x the basal strength and a moderately high pyramidal family strength at 1.7x the basal strength. When using these parameters, both the modeling and experimental results show that regions with the lowest strength-to-stiffness ratio slip first at lower strains and that subsequent regions with a higher strength to stiffness ratio undergo slip at progressively higher strains. The presence of MTRs does not change the direct relationship between the strength-to-stiffness ratio in the modeling work, but they do allow for the formation of extended slip bands that traverse multiple grains. In the experimental work in this study, we primarily observe basal slip in grains well oriented for such at all temperatures and cycles. While this result agrees with the selection of the CRSS ratios used by Kasemer et al. [107] that selected the basal slip family as the weakest slip family, the relative values between the basal CRSS and the prismatic CRSS are still under active investigation. The long range observed basal slip instead be due to the presence of the intermetallic Ti_3Al in the alloy. The Ti_3Al, also called the α_2 phase, has a hexagonal phase with a DO_{19} structure. The long-range order of the α_2 limits the number of deformation modes and prevents twinning. Additionally, it makes basal <a> slip more difficult since it creates disorder in the DO_{19} structure of the intermetallic. The high antiphase boundary energy of the α_2 phase inhibits cross slip from the basal plane onto prism and pyramidal planes. Therefore, the observed basal slip activity is extremely planar in alloys with Ti_3Al [17]. The presence of this intermetallic may be responsible for the observation of both the significant long-range planer basal slip and the lack of long range prismatic slip. TEM analysis is actively underway to determine the potential presence of both the Ti_3Al and prismatic slip activity.

Under the dwell loading conditions in the present study, regions with slip activity are strongly correlated with the strength of the basal slip family after 200 cycles. Under other loading conditions with a higher peak stress or with additional cycling, it may be necessary to include and normalize other slip families in the determination of the strength parameter in the strength-to-stiffness ratio. In this study, it is demonstrated that the basal strength-to-stiffness ratio is an important factor when determining the effective structural units and weakest link regions of a microstructure under dwell fatigue. If the proposed life-limiting parameter of dwell fatigue is early crack initiation due to load shedding, the slip planes that allow for the largest and earliest dislocation pile ups should be considered the critical characteristic. Hence, future characterization and segmentation protocols should focus on identifying these features.

5.4 Conclusions

Definitions of MTRs based on clustering of the c-axis do not do a good job at identifying which grains behave as effective structural units. By comparing the plastic deformation of dwell fatigued samples at RT, 120°C, and 200°C to the regions defined by current prevailing c-axis methods as hard and soft, it is clear that these traditionally soft regions do not engage in cooperative long-range slip and therefore would not contribute significantly to load shedding. Rather, the regions of cooperative slip can be initially identified by a directional strength-to-stiffness ratio, where the strength metric is defined by the basal Schmid factor.

- There is no MTR segmentation that accurately describes the bounds of regions of grains that behave cooperatively based upon the grouping of the c-axis orientation relative to loading and the minimum allowable size of an MTR alone. The sub-regions of classically defined MTRs that act cooperatively cannot be captured with a c-axis grouping, no matter how small the allowable tolerance angle is.
- Even if an ideal MTR segmentation using c-axis grouping can be found for a single sample or region, the metrics of that segmentation cannot be applied to other samples freely. For all the sample gauge sections studied in this chapter, different segmentation metrics were better for different regions of each gauge section. Due to the complexity of the phenomenon, there likely exists a variety of different metrics that describe the ability of grains to behave as a structural unit and help determine whether a material with experience long range slip and early crack nucleation.

- The orientation of the c-axis does not accurately describe or predict regions that behave as soft regions in a classic modified Stroh model of load shedding under dwell fatigue at any investigated temperature.
- The directionally dependent elastic modulus captures the subregions of MTRs that facilitate long range slip. Long range slip does not occur in the least stiff regions, but rather in regions with an effective modulus between 115-125 GPa. It also appears that slip activity occurs in subregions of MTRs with a relatively lower effect modulus than its surroundings. This hypothesis is under active investigation.
- Groups of grains that behave cooperatively to facilitate long range slip have a low strength-to-stiffness ratio when the basal Schmid factor is used as the strength metric.
- There is no link between the Taylor factor of a point and its propensity to slip, whether from a comparison to the Taylor factor alone or when the Taylor factor is used as the strength metric in a strength-to-stiffness ratio.
- The strength-to-stiffness ratio better describes grains that are behaving as hard and soft grains in the modified Stroh model of load shedding than the orientation of the c-axis. This metric should be considered as a hierarchical segmentation parameter for MTRs that could be used in future data-driven or CPFE modeling efforts to understand load shedding and crack initiation under dwell fatigue.

Chapter 6 Slip Behavior of Individual Grains Under Dwell Fatigue in Ti-6242

6.1 Introduction

Because titanium alloys lack hard second phases and inclusions, the effective slip length of the material is a primary factor influencing mechanical properties, as shown schematically in Figure 6.1 [17]. Of relevance to this work is the fact that longer slip lengths are known to be detrimental to fatigue crack nucleation. In most studies, MTRs are believed to effectively behave as giant grains that increase the effective slip length of the material [86]. The preceding sections have shown that this is not the case, however, at least within the prevailing method for characterizing MTRs using c-axis misorientations as the grouping criterion. In the previous sections, it was shown that groups of grains that slip cooperatively are well oriented for basal slip and spatially arranged in a way that aligns the basal slip traces.

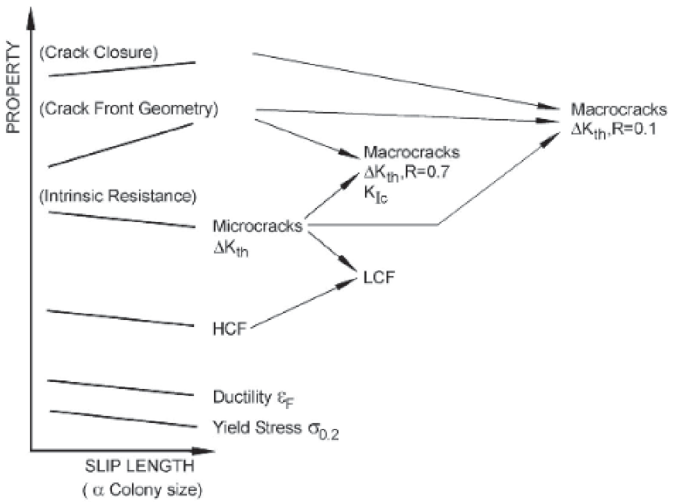

Figure 6.1: Influence of slip length (α colony size) on mechanical properties represented schematically [17]

To compare whether these regions of cooperative slip behave similarly to the slip activity in individual grains, the behavior of individual grains under dwell fatigue loading was explored. SEM DIC experiments (which offer much higher spatial resolution) were performed on 500 um x 500 um regions of the sub regions of the gauge section of Ti-6242 dwell fatigue samples. These regions were selected to explore a more randomly textured region of the material with a low amount of microtexture at a higher resolution. The image resolution of these individual grain studies was 14.65 nm/pixel (~682 pixels across the diameter of a 10μm grain) versus the 73.24 nm/pixel (~136 pixels across the diameter of a 10μm grain) for the full gauge studies. This increased spatial resolution allows us to examine the slip activity more closely within individual grains to gain further insight into the conditions that permit cooperative slip. The results of this study show that basal slip is the dominant slip activity within individual grains of a less microtextured microstructure. Slip lengths are primarily limited to one grain in the absence of microtexture, but similarly oriented grain neighbors can allow for the transfer of basal slip through 2-4 grains. By comparing the results of slip activity in individual grains with the slip activity through a microtextured material, it is demonstrated that grains well oriented for basal slip are the primary deformation mode at all temperatures, length scales, and cycles investigated in this study.

6.2 Results and Discussion

As seen in Chapter 4, the full gauge slip behaviors of RT and the 120°C were extremely similar, and similar load shedding mechanisms are expected. A significant difference in slip activity was observed between experiments run at dwell sensitive temperatures (RT and 120°C) and experiments at dwell insensitive temperatures (200°C). Therefore, tests were only run at the extremes of RT and 200°C to investigate the behavior of individual grains under dwell fatigue loading in Ti-6242.

6.2.1 Effects of Microtexture

When looking at the slip activity in grains, individual grains near hard microtextured regions appear to initiate slip with few cycles at RT. Both orientation maps and pole figures shown in Figure 3.3 indicate that each sample has a moderate basal texture. Slip activity after 2 and 200 dwell fatigue cycles is superimposed over these orientation maps in Figure 6.2. The subregions of the gauge section were selected to investigate a more randomly textured region of the materials. The edges of the RT FOV clearly have large MTRs that extend approximately 100-150 microns into the region. The center of the FOV is relatively low microtexture with a wide distribution of grain orientation that exists in clusters of 1-3 grains. The material tested at 200°C is also relatively free from large microtextured regions. After two dwell cycles more of the slip activity occurs around the edges of the FOV, within and around the (typically assumed to be) hard microtextured regions than in the unmicrotextured center of the FOV. The individual grains in the unmictotextured center of the RT FOV have also slipped by the time 200 cycles are accumulated. This could indicate the influence of MTRs not only on the length of slip traces, but also on how early the slip initiates relative to the number of dwell cycles.

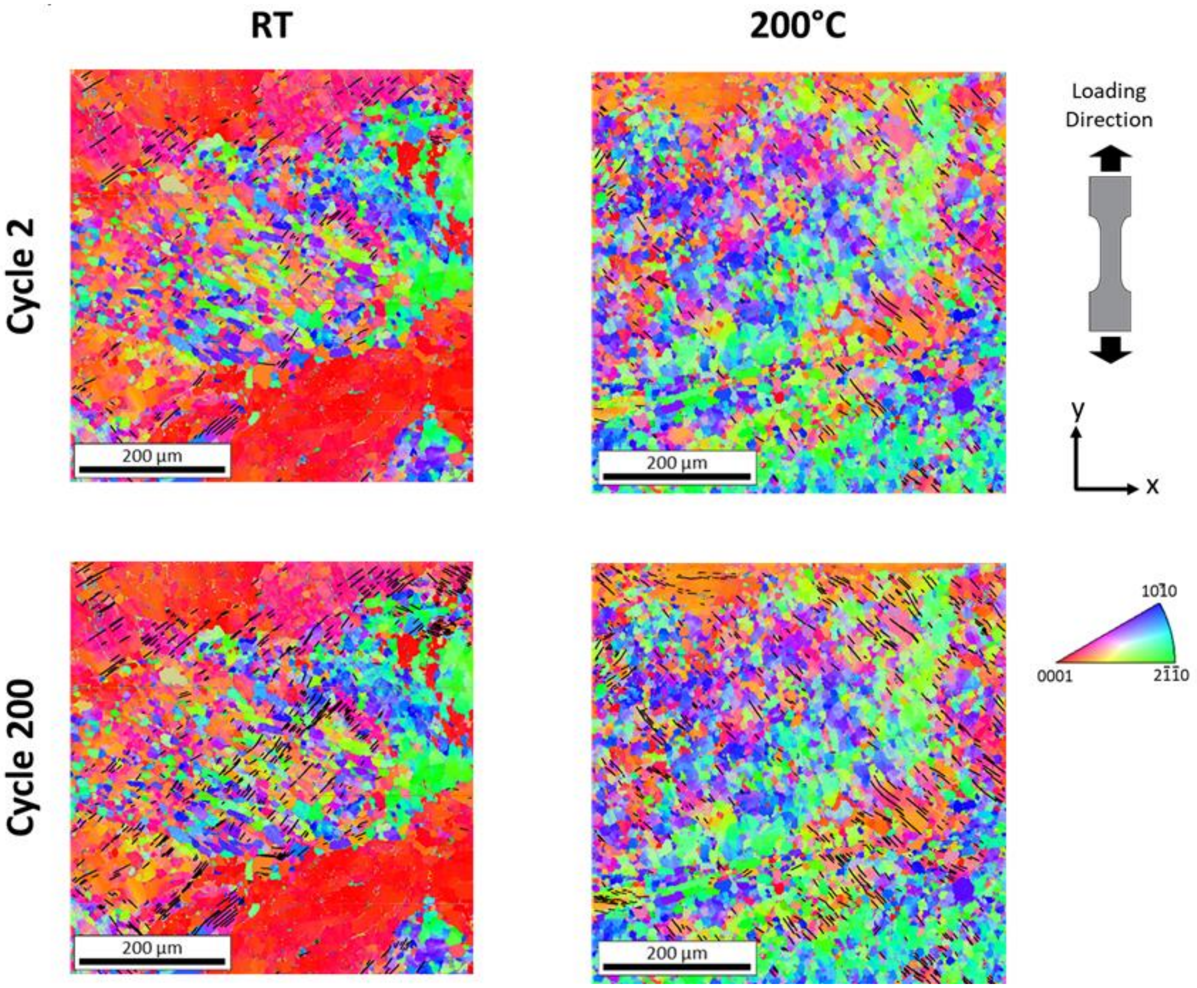

Figure 6.2: EBSD orientation maps for grain level study at RT and 200°C with slip traces segmentation map after 2 and 200 dwell cycles superimposed in black. These maps show that slip activity forms in regions with clusters of similarly oriented basal grains after 2 cycles, with more diffuse slip occurring within the rest of the FOV after 200 cycles. This is especially evident in the RT specimen where more slip after 2 cycles exists in the microtextured regions on the edges of the FOV.

6.2.2 Number of Slip Traces

Both the RT and the 200°C experiments exhibit a similar number of slip traces after 2 and 200 dwell cycles, as shown in Table 6.1. This is in contrast to the very different number of slip traces and rate of strain accumulated in the full gauge of the dwell samples in Chapter 4. As this is just a small subset of the entire gauge, it is not expected to be indicative of the overall behavior of the sample and will have variation. The results in Chapter 4 indicate that the full gauge at 200°C accumulates less slip, less quickly than at RT. The similar number of slip traces is also likely related to the texture of the materials. The slip traces at 200°C are generally shorter than the slip traces at RT as seen in Figure 6.5. The number of shorter slip traces at 200°C is linked to the number of available locations to slip. This will be further discussed in relation to the Schmid factors associated with basal slip in section 6.2.5.

Table 6.1: *Number of slip traces in each sample after 2 and 200 cycles, at room temperature (RT) and 200°C.*

	RT	200°C
Number of Traces After 2 Dwell Cycles	235	224
Number of Traces After 200 Dwell Cycles	625	649

6.2.3 Slip Type

At all temperatures and cycles, basal slip activity dominated with over 55% of all the observed slip activity being basal slip (Figure 2.1). This is consistent with the observations within the whole gauge section, where the slip was dominantly basal, and the co-location of basal orientated grains allowed for the formation of long-range basal slip through tens of grains. At 200°C, an even greater percentage (>70%) of all slip activity at all cycles is basal, indicating that plastic anisotropy alone is not the driving quality of the temperature dependence of load shedding. In previous modelling work, the dwell debit is proposed to disappear at ~200°C in Ti-6242 as the degree of plastic anisotropy diminishes. Ozturk et al. [14] proposed that as temperature increases the CRSS required to activate basal, prismatic, and pyramidal slip begin to lower and converge as shown in Figure 2.10. They claim that this reduction in plastic anisotropy essentially eliminates the large dislocation pile ups at hard/soft interfaces and load shedding and therefore the dwell debit disappears at elevated temperatures. If this were the case, a large amount of slip on a variety of slip families would be expected. However, we continue to see basal slip dominate at all temperatures with 200°C being even more prevalent than at RT. This behavior is apparently length-scale-independent as this same trend is observed for long-range slip traces in experiments performed on the whole gage section of dwell fatigue samples. Due to the model hypothesis assuming diffuse slip activity on multiple slip systems, it would be reasonable to think that the large amount of diffuse slip could operate on the grain level and not be observed at the MTR length scale for long range slip. The fact that basal slip is the most prevalent slip type at elevated temperatures when investigating MTRs and individual grains, refutes this hypothesis as the primary factor for the temperature dependence of the dwell debit.

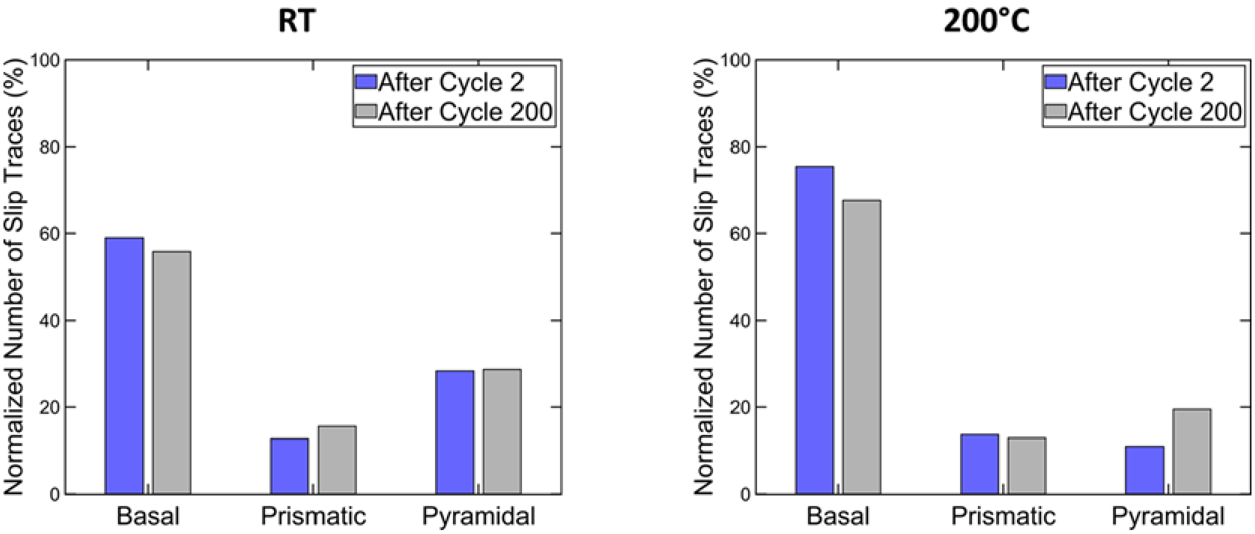

Figure 6.3: Active slip systems for the identified slip traces after 2 and 200 cycles at RT and 200°C. Basal slip initiated early and continued to dominate with cycling, but there was little long-range prismatic activity. Rather, the relatively high activity of pyramidal slip is attributed to the exhaustion of easily activated basal slip, and the subsequent activation of slip in neighboring regions that favored pyramidal over prismatic slip

While prismatic slip is often reported as the slip system with the lowest CRSS, very little prismatic slip is observed within individual grains at any temperature or cycle number. This is consistent with long-range slip observations in section 4.2.3. From the orientation maps in Figure 6.2, there are plenty of grains that are well oriented for prismatic slip but few of those regions are active. The absence of prismatic slip could be due to a lack of slip planarity due to the high number of available slip planes for prismatic slip or due to a difference in the CRSS where basal slip is easier, as discussed in Chapter 4. TEM analysis on clusters of grains well oriented for prismatic slip is underway to further investigate if there is no prismatic slip activity or if it just does not create clear slip traces on the samples surface. Whatever the reason, it is clear that prismatic slip does not contribute significantly to dislocation pile up, load shedding and early crack nucleation in the material under these loading conditions.

Pyramidal slip is the second most prevalent type of slip at the individual grain level, and it exists in regions nearby to the basal slip activity as seen in Figure 6.4. Pyramidal slip makes up ~20-30% of the slip traces at all temperatures and cycles. These same trends are also seen in the behavior of the long-range slip traces in section 4.2.3. From Figure 6.4, the pyramidal slip primarily occurs in clusters of harder grains adjacent to grains with basal slip activity at all temperatures. The stress localization and/or basal slip exhaustion is believed to trigger pyramidal slip in grains with a high pyramidal Schmid factor. Pyramidal slip occurred within larger groups of hard oriented grains, indicating that its existence is influenced by the local neighborhood.

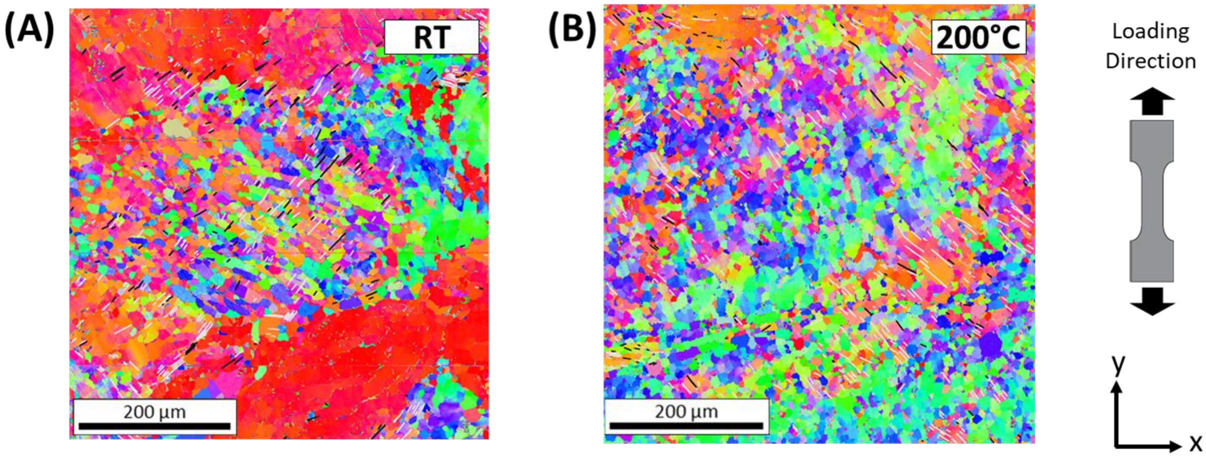

Figure 6.4: Basal (light gray) and pyramidal (black) slip traces overlaid on the IPF map at **(A)** RT and **(B)** 200°C. Basal slip traces exist in basally soft grains, and pyramidal slip exists in nearby grains. This is attributed to the accommodation of internal stresses after basal slip exhaustion.

While pyramidal slip does not directly contribute to load shedding, it may highlight locations where load shedding may occur. Pyramidal slip occurs under dwell loading below the macroscopic yield of the material, but it does not typically exist as long-range traces, as discussed in section 4.2.3. Therefore, it does not contribute to long range dislocation pile up, load shedding, and the overall dwell debit. It may indicate that extensive basal slip requires neighboring hard regions due to some neighborhood effect. The activation of pyramidal slip in hard grains may be an indicator of regions where hard grains are carrying an elevated stress to accommodate for the significant basal deformation in neighboring grains [45].

6.2.4 Slip Lengths

Without the presence of co-located basal oriented grains, deformation be accommodated by long-range slip bands regardless of temperature or cycle count. Over 99% of all traces span less than 4 grains and measure less than 40 µm while over 50% of all slip traces are 10 µm or shorter through 1 or fewer grains Figure 6.5. Most of the traces that do extend through more than one grain are on basal slip systems. Even when looking at the behavior of individual grains within low microtextured material, basal slip activity is the primary slip family that can act cooperatively. This is further evidence of how basal slip is the primary slip activity of concern related to the long-range dislocation pile ups related to dwell fatigue and load shedding.

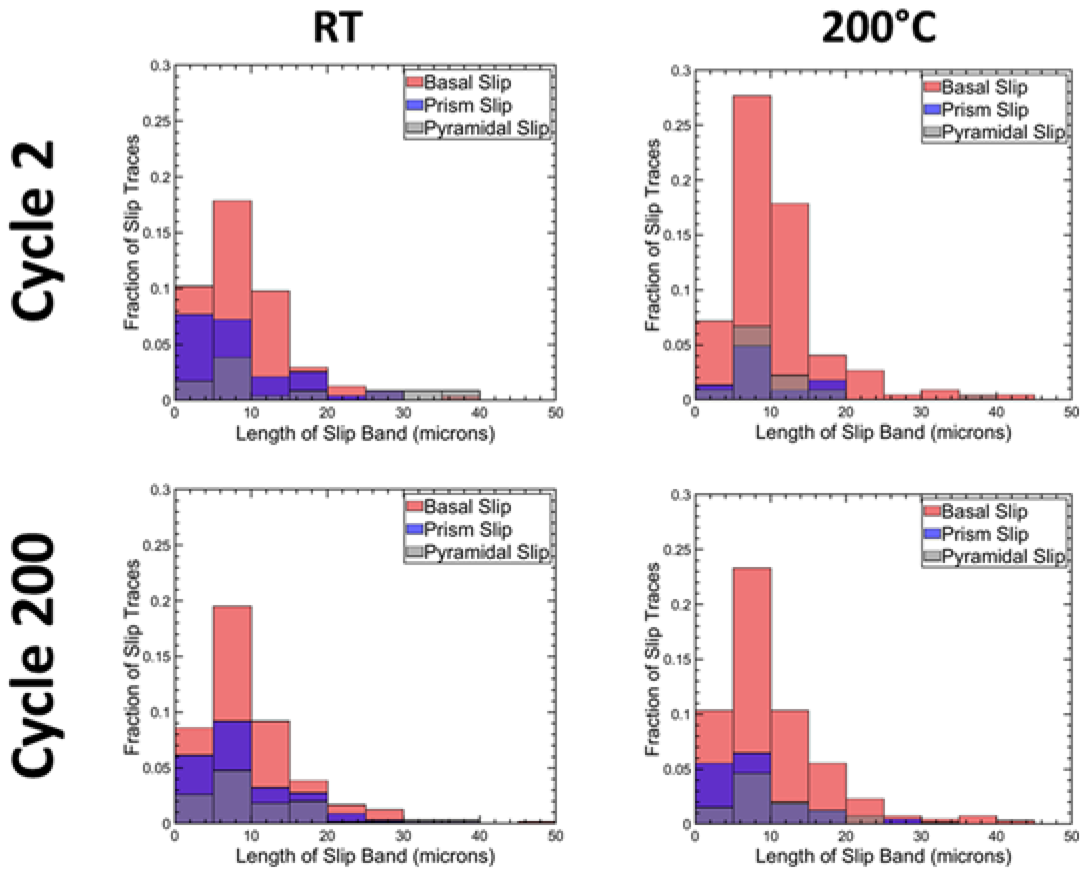

Figure 6.5: Histograms of slip length and family after 2 and 200 cycles at RT and 200°C. Most traces were through only one grain (10 µm) and the bulk of deformation at all temperatures was accommodated by short basal slip activity. Most of the traces that extend through more than one grain are basal, which is in agreement with the finding in Chapter 4 that grains that are able to work cooperatively are co-located grains with a high basal Schmid factor.

The distributions of slip trace lengths remain consistent with cycling at both RT and 200°C, and there are more basal traces longer than 1 grain at RT than at 200°C. This indicates that the slip activity of individual grains is microstructurally driven, and the overall trends and locations of deformation can be predicted from early cycles. The greater number of basal traces longer than 10 microns at RT than at 200°C is also a result of local microtexture. The microtextured regions at the edges of the FOV have clusters of many grains that are well oriented for basal slip and allow for slip transfer between grains while the 200°C FOV has more individual regions oriented for basal slip, but the regions are made up of few grains as seen in Figure 6.4. Microstructure and microtexture clearly dictate both the locations and lengths of the slip activity at all temperatures, cycles, and length scales.

Additionally, at RT, there are a few pyramidal slip traces that extend through more than one grain as a result of microtexture. These longer pyramidal traces all exist on the edges of the FOV where clusters of hard oriented grains exist nearby to basal slip activity, as seen in Figure 6.4. These results highlight the how basal slip activity drives the deformation of Ti-6242 under dwell loading at every length scale, and that the presence of basal slip adjacent to clusters of hard grains can redistribute stresses to activate grains with a higher CRSS than expected at 90% of the macroscopic yield strength.

6.2.5 Schmid Factors

After two dwell cycles at all temperatures, all basal and pyramidal slip activity occurs in regions with a high basal and pyramidal Schmid factor, respectively. Over 95% of basal slip has a basal Schmid factor above 0.4 after 2 dwell cycles as seen in Figure 6.6. Over 99% of pyramidal slip occurs in grains with a pyramidal Schmid factor above 0.4. The locations of pyramidal slip are in grains well oriented for pyramidal slip adjacent to grain undergoing basal slip. These same trends are observed for long-range slip traces in the entire gauge section.

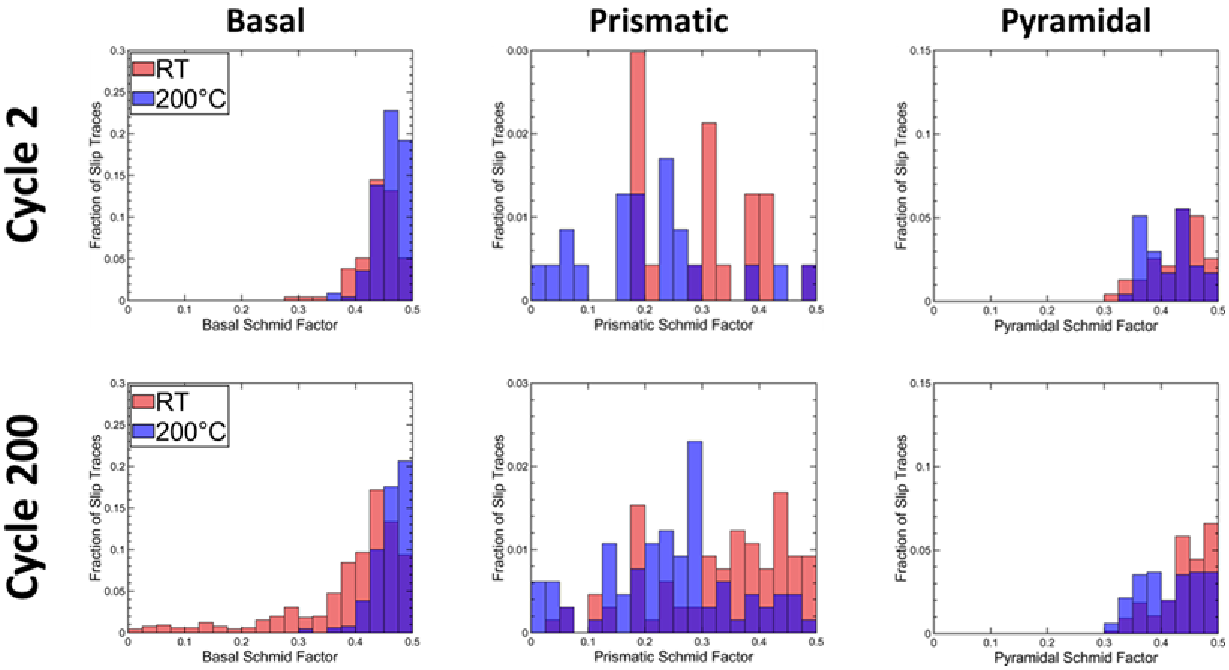

Figure 6.6: Histogram of the **(A)** Basal, **(B)** Prismatic, **(C)** Pyramidal Schmid factors of each slip trace at RT and 200°C. At both temperatures, slip primarily occurred through grains with high basal and pyramidal Schmid factors. In the case of prismatic slip, the small number of traces affected the distribution shape (note the y-axis is set to 3% in this plot for visualization).

The drop in required basal Schmid factor demonstrates the time dependence of dwell fatigue deformation and is proposed to be due to the exhaustion of easily activated slip. After the easily activated basal slip is exhausted, less favorably oriented grains or systems with higher CRSS must slip to accommodate deformation. This is the same proposed mechanism behind the activation of more difficult to initiate pyramidal slip in areas adjacent to extensive basal slip activity. It is also likely an example load shedding, where the extensive basal slip requires the hard oriented grain to carry a higher load. This stress concentration causes localized pyramidal slip to occur in the hard grain at macroscopically applied stress lower than would be expected. It is suggested that basal slip at 200°C does not become exhausted with cycling due the temperature dependence of the strain rate, and therefore there is no need to accommodate deformation via less favorable slip such as basal slip of unfavorable oriented grains and pyramidal slip which has a greater CRSS. With additional cycling from 2 to 200 cycles, a significant amount (~30%) of basal slip at RT activity occurs in grains with a basal Schmid factor below 0.30, while the basal Schmid factors associated with basal slip at 200°C remains above 0.40 for all basal slip traces (Figure 6.6). This same trend is seen in the behavior of basal and pyramidal slip activity in MTRs observed in the whole gauge section of samples at RT and 200°C in section. Basal slip within grains well oriented for basal slip is the driving deformation mechanism at all temperatures, cycles, and length scales.

The reduction in basal Schmid factor needed to activate slip correlated to basal slip activity at RT for individual grains also suggests that similar number of slip traces at RT and 200°C after 200 cycles is specifically related to the microstructure of the inspected region. At 200°C there are more smaller regions that are well oriented for basal slip with a Schmid factor above 0.40, as shown in both the Schmid factor plots in Figure 6.6, orientation maps Figure 6.2, and trace length plots in Figure 6.5. At RT, the regions oriented for basal slip are larger and more continuous as seen in Figure 6.2. Additionally, there is a greater variety of orientations available to slip via basal slip. Due to there being more individual disparate regions well oriented for easy slip activity at 200°C, there is a comparable number of slip traces at 200°C to the number of traces at RT. The entire gauge section tests in section, are believed to indicate a more statistically significant result where the 200°C accumulates less strain less quickly than at lower temperatures. Additionally, long range slip is the most damaging relative to dislocation pile ups and load shedding, therefore trends about the formation of slip through multiple grains are the more critical relationship for dwell fatigue modeling and lifing predictions.

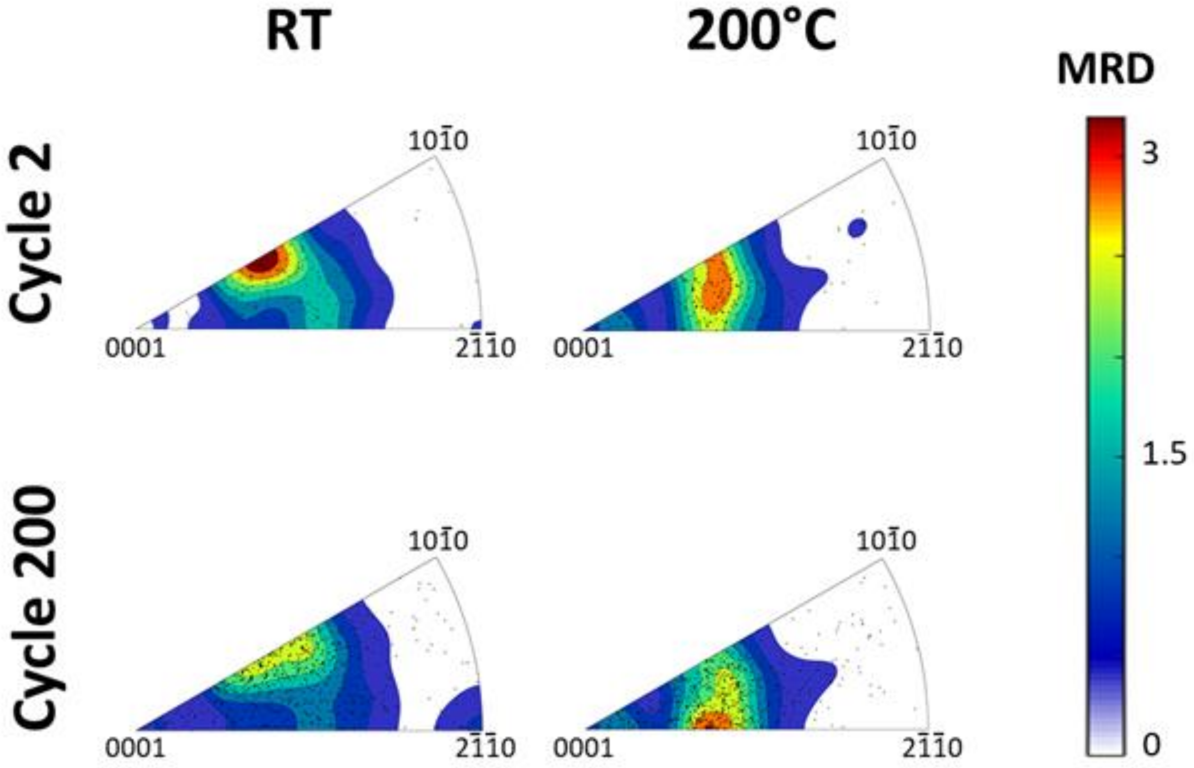

Figure 6.7: Slip trace orientations plotted on an IPF for samples tested at RT and 200°C, after 2 and 200 cycles. At all temperatures, slip traces tended to occur through grains with a high resolved shear stress on the basal plane. The black points indicate the dominant orientation of the grains each discrete slip traces passes through and the contours represent the density of those discrete points on each IPF.

6.2.6 Strength-to-Stiffness Ratio

Slip activity in individual grains occurred in grains with a low strength-to-stiffness ratio when the basal Schmid factor is used as the strength parameter. Using the formulation proposed in Chapter 5, the basal strength-to-stiffness map was calculated from the orientation data for the RT and the 200°C FOVs. These strength-to-stiffness maps with the segmented slip traces overlayed in white are shown in Figure 6.8. The basal strength-to-stiffness is bound between the values of 0.0151 and infinity, as bound by the basal Schmid factor and the effective elastic modulus. Histograms showing the distribution of the basal strength-to-stiffness for the entire FOV and the slipped points in the FOV is in Figure 6.9. At RT, >50% of slip occurs through regions with a strength to stiffness ratio below 0.02 and >70% of slip occurs through regions with a strength-to-stiffness ratio below 0.0225. Compared to the entire map where only ~43% of the whole FOV has a strength-to-stiffness below 0.0225, this indicates a preference for slip to occur in grains with a low strength-to-stiffness ratio rather than just a trend resulting from the distribution of grain orientations investigated. A similar relationship exists at 200°C where 75% of slip occurs through regions with a strength-to-stiffness ratio below 0.0225, and only 45% of all points in the FOV have a strength-to-stiffness ratio below 0.0225.

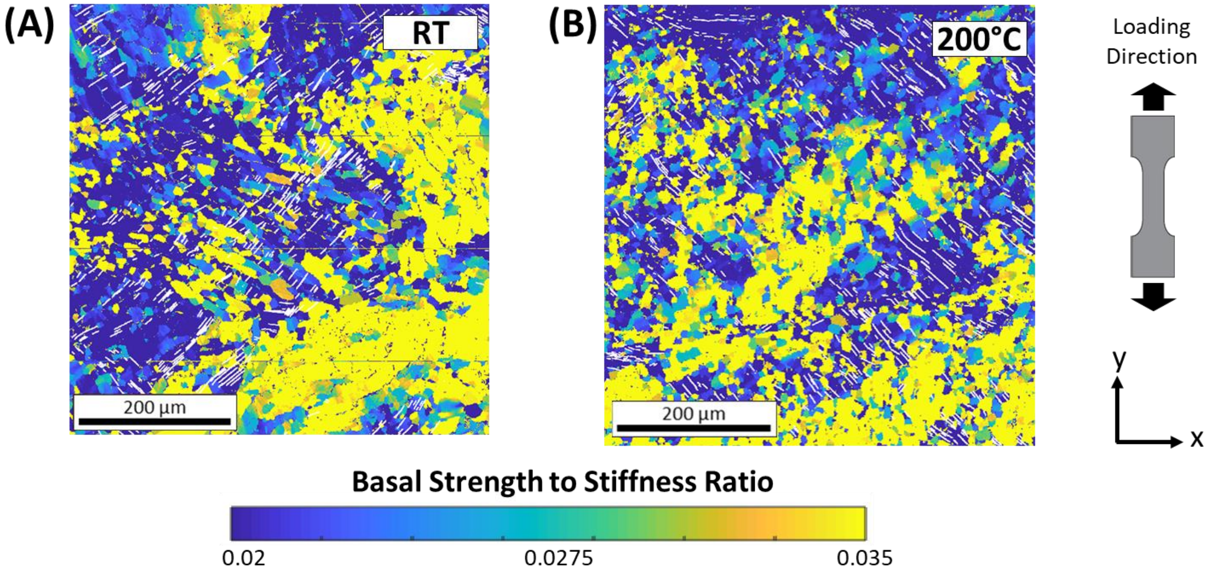

Figure 6.8: Map of basal Schmid factor strength-to-stiffness ratio of samples at RT and 200°C with slip traces after 200 dwell cycles superimposed on the maps in white. There is a clear relationship between locations of slip activity and a low strength-to-stiffness ratio calculated with the basal Schmid factor as the strength parameter. From the images, it is also clear that the slip traces are visually bound within regions with a low strength-to-stiffness ratio by regions with a high strength-to-stiffness ratio.

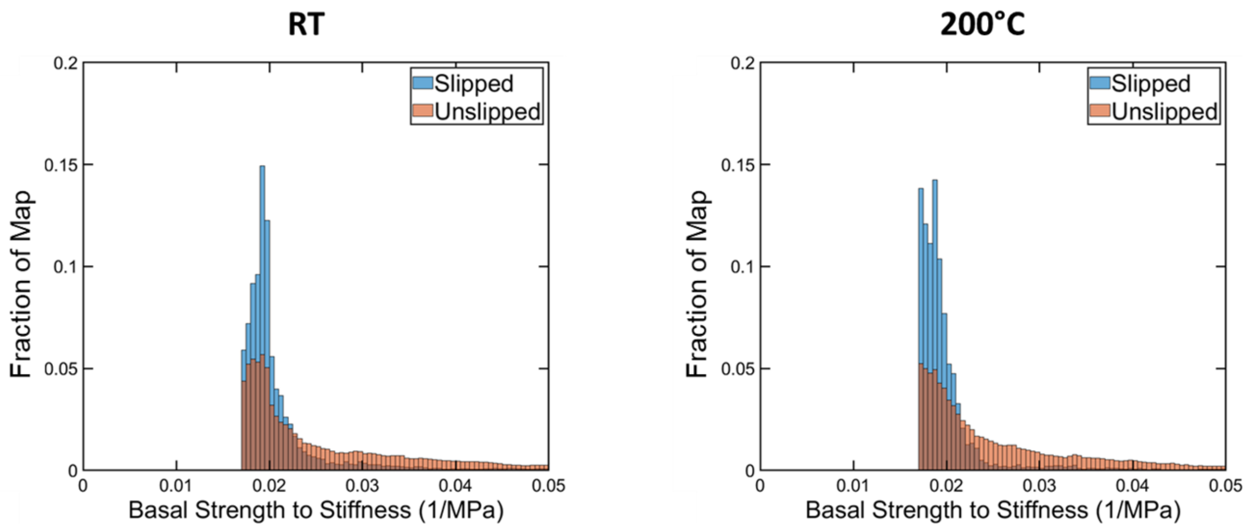

Figure 6.9: Histogram of the Basal Schmid Strength to Stiffness Ratio for all the points in the orientation map and for all the slipped points in the orientation map for Samples D and E. There is a clear relationship between locations of slip activity and the strength to stiffness ratio calculated with the basal Schmid factor as the strength parameter.

Looking at the maps in Figure 6.8, it is also clear that the slip traces are visually bound within regions with a low strength-to-stiffness ratio by regions with a high strength-to-stiffness ratio. This indicates that the basal strength-to-stiffness ratio is a good predictor for slip activity for both long-range slip as seen in section 4.2.3, and for slip activity in less microtextured material through individual grains. From the maps in Figure 6.8, it is also clear that not all regions with a low strength-to-stiffness ratio experience slip. By visual inspection, it appears that the low strength-to-stiffness regions experiencing slip activity have large neighboring regions with a high strength-to-stiffness ratio. The fact that the traces were bound by regions with a higher strength-to-stiffness ratio may indicate a neighborhood effect where the stiffer, higher strength regions produce some type of stress redistribution or allow for load pathways through the material that preferentially activates easy basal slip in spatially nearby regions. A similar relationship is found in the MTR investigation in Chapter 4, where basal slip activity primarily occurs within sub-features of hard MTRs defined with existing methods based on c-axis orientation. As this correlation is found at multiple length scales, it would also be important to define the length scale of influence for this proposed neighborhood effect. It is currently unclear if this is a first nearest neighbor investigation, or if a greater region of influence should be considered. To fully investigate this theory, more experiments on samples with various microstructures would need to be conducted to understand if there is a greater neighborhood effect or if this observation is just a correlation without an underlying mechanistic explanation.

6.2.7 Conclusions

In Ti-6242 under dwell fatigue loading to 90% of the macroscopic, temperature-corrected yield strength, individual grains do not behave like MTRs defined by current prevailing methods. It was found in Chapter 4 that "prism-soft" MTRs defined by prevailing methods do behave cooperatively as effective structural units, but rather long-range slip is accommodated by co-located grains well oriented for basal slip activity. When considering this newly defined effective structural unit that is known to act cooperatively, the slip activity in individual grains matches the slip activity of cooperative grains through microtextured regions at all tested temperatures and cycles. Slip activity is dominantly basal through grains well oriented for basal slip at both RT and 200°C after 2 and 200 cycles. At RT, where the temperature dependent strain rate sensitivity is higher than at 200°C, the easily activated basal slip exhausts or causes additional internal stress [14], [15], [77]. These factors cause less favorable basal and pyramidal slip to occur in neighboring grains to accommodate deformation at RT. This is not believed to occur at 200°C, where the strain rate sensitivity is not as significant [15]. Very little prismatic slip is observed at any temperature or cycle, indicating that even in an unmicrotextured material prismatic slip is not the driving deformation mechanism for load shedding and the dwell debit.

The trends in individual grains follow those observed in the whole gauge section of microtextured Ti-6242 at RT and 200°C. By comparing the results of slip activity in individual grains with the slip activity through a microtextured material, it is demonstrated that basal slip through grains well oriented for basal slip is the primary form of deformation accommodation at all temperatures, length scales, and cycles investigated in this study. In unmicrotextured material, the short length of the slip traces likely prohibits the formation of long-range dislocation pile ups that would result in early load shedding and crack nucleation. The presence of microtextured regions, specifically co-located grain well oriented for basal slip would allow for large pile ups that represent a life-limiting condition leading to early crack nucleation. It is reasonable to assume that with a stricter definition of cooperative grain clusters and MTRs, information from the investigation of single grains could be extrapolated for the modeling and understanding of load shedding in MTRs. The findings in the present study are useful for identifying the grain orientations and grain groupings critical to load shedding and early crack nucleation in Ti-6242 under dwell fatigue.

Chapter 7 Conclusions

7.1 Conclusions

Microtextured Ti-6242 under dwell fatigue loading was investigated at multiple length scales to understand the plastic strain response of individual grains and microtextured regions at RT, 120°C, and 200°C. The dwell fatigue response of near-alpha alloys, such as Ti-6242, is known to be dependent on both temperature and local microstructure. This study utilized orientation information from electron backscatter diffraction (EBSD) and high-resolution plastic strain maps from digital image correlation (DIC) performed in a scanning electron microscope (SEM) to study the correlation between temperature, microstructure, and plastic slip activity over a large area of interest. The key findings from this study relative to the microstructure, microtexture, and temperature dependence of load shedding during dwell fatigue in Ti-6242 are as follows.

7.1.1 Microstructure

- Plastic slip activity at all temperatures and length scales is microstructurally driven, and locations that experience slip are evident from early cycles. At all temperatures (RT, 120°C, and 200°C) and length scales (individual grains and MTRs), new slip traces occurred largely in regions that had already exhibited slip. There were no locations that exhibited little slip activity after two dwell cycles and subsequently accumulated significant slip. This supports the conjecture that slip and its evolution under dwell cycling are microstructurally driven by cooperative grain groupings that allow the traversal of contiguous slip activity.

- Basal slip is the primary active slip family that contributes to long-range slip and dislocation pile ups that could result in load shedding and early crack nucleation. Deformation at all temperatures and length scales was largely accommodated by long-range basal slip in co-located grains with high basal Schmid factors, and shorter pyramidal slip in nearby grains with high pyramidal Schmid factors. No significant prismatic or pyramidal slip was observed to occur independently in areas far from those of basal slip. This is likely due to internal stresses initiating the activation of less favorable slip in the neighboring grains following the exhaustion of basal slip, indicating that the dwell debit is not solely orientation dependent and that we must also consider the effect of microstructural neighborhood.
- In Ti-6242, prismatic slip activity does not contribute to long-range slip and dislocation pile ups that would influence the dwell debit. There was little observed prismatic slip activity, despite it being typically reported as the softest slip system. These observations do not necessarily imply no prismatic slip is occurring, but that if so, it does not manifest as slip traces visible on the surface of the sample during dwell fatigue at 90% of macroscopic yield.

7.1.2 Temperature

- The temperature dependence of the plastic anisotropy of Ti-6242 is the not primary contributor to the temperature dependence of the dwell debit. Plastic deformation is accommodated primarily by basal slip at all temperatures and length scales. Previous modelling work implies that the temperature dependence of dwell sensitivity is mainly due to the temperature dependence of the plastic anisotropy and the CRSS of each slip family as seen in Figure 2.10 [14]. If this were the case, more diffused slip on all different slip systems would be expected 200°C, where the dwell debit is not considered significant. In both individual grains and clusters of grains, basal slip is the most prevalent slip type, which refutes the conjecture that the temperature dependence of plastic anisotropy is the primary factor for the temperature dependence of the dwell debit.

- It is proposed that the temperature dependence of the strain rate sensitivity is more strongly linked to the temperature dependence of the dwell debit in Ti-6242. When observing the full gauge section of dwelled samples, there was both a greater number and a faster accumulation of slip traces at temperatures that exhibit a dwell debit in Ti-6242 (RT and 120°C) versus that which does not (200°C) when observing the full gauge section of dwelled samples. The lack of slip activity at 200°C may be related to the temperature dependence of strain rate sensitivity [14], [15], [77], where a more rapid stress relaxation occurs with increasing temperature, thereby reducing the number of dislocations in a given pileup and resulting in lower effective stresses due to decreased localized plastic strain accumulation.

7.1.3 Microtextured Regions (MTRs)

- MTRs defined by current prevailing methods do not define the groupings of grains that act cooperatively for long-range slip activity that would contribute to large dislocation pile ups and load shedding. Slip did not transmit across the entirety of MTRs defined by prevailing methods, but rather was driven by contiguous groups of basal-oriented grains. This differs from the behavior of MTRs in crack growth studies, where similarly oriented grains do not need to be interconnected to behave cooperatively and permit rapid crack growth. The observed slip systems and Schmid factors in this study narrow the definition of MTRs that accumulate damage under dwell fatigue loading. These results indicate the necessity of grain interconnectivity.

- At all temperatures (RT, 120°C, and 200°C), grains that behaved cooperatively and exhibited long-range plastic slip were (i) co-located; (ii) had high basal and/or pyramidal Schmid factors, with basally-soft slip dominating; and (iii) exhibited small variations in orientation.
- The orientation of the c-axis relative to the loading direction is not a complete metric to segment clusters of grains that act cooperatively for load shedding under dwell fatigue loading. The orientation of the c-axis does not accurately describe or predict regions that behave as hard and soft regions in a classic modified Stroh model of load shedding under dwell fatigue at any investigated temperature. There is no MTR segmentation that accurately describes the bounds of regions of grains that behave cooperatively based upon the grouping of the c-axis orientation relative to loading and the minimum allowable size of an MTR alone. The sub-regions of classically defined MTRs that act cooperatively cannot be captured with a c-axis grouping, no matter how small the allowable tolerance angle is.
- Groups of grains that behave cooperatively to facilitate long range slip have a low strength-to-stiffness ratio when the basal Schmid factor is used as the strength metric. The strength-to-stiffness ratio better describes grains that are behaving as hard and soft grains in the modified Stroh model of load shedding than the orientation of the c-axis. This metric could be used as a hierarchical segmentation metric for MTRs and be used in future modeling efforts to understand load shedding and crack initiation under dwell fatigue.

- The trends in individual grains are identical to the trends observed in the whole gauge section of microtextured Ti-6242 at RT and 200°C. By comparing the results of slip activity in individual grains with the slip activity through a microtextured material, it is demonstrated that basal slip through grains well oriented for basal slip is the primary form of deformation accommodation at all temperatures, length scales, and cycles investigated in this study.
-

7.2 Future Work

The results of this work leave many questions about load shedding and dwell fatigue in Ti-6242 unanswered and raise new questions for study. The future work that logically follows from the findings in this thesis are related to the understanding of MTRs, microstructural neighborhood effects, and the time-dependent nature of load shedding.

7.2.1 MTRs

- The results reveal that MTRs defined by prevailing methods do not define the clusters of grains that act cooperatively for load shedding and crack nucleation in Ti-6242. Rather, it is suggested in this thesis that the regions of cooperative hard and soft grains pertinent to load shedding is correlated to the strength-to-stiffness ratio of spatial neighboring grains. From this study, grains with a low strength-to-stiff metric where the basal Schmid factor is used as the strength factor are associated with regions that experience slip activity, while hard regions that resist slip have a relatively higher strength-to-stiffness metric. These results speak to the mechanistic importance of a grains ability to deform via basal slip and its orientation dependent elastic modulus. An implementation and systematic study of these findings in an MTR segmentation algorithm would likely further the community's ability to identify dwell sensitive materials. This metric could be used as a hierarchical segmentation metric for MTRs and in future modeling efforts to understand load shedding and crack initiation under dwell fatigue.

- Additionally, in this study, it is clear that basal slip dominates during dwell loading in Ti-6242 when the peak stress is 90% of macroscopic yield. Therefore, the basal slip strength is an appropriate metric for the strength parameter of the strength-to-stiffness ratio suggested in this study. For other titanium alloys and peak dwell stress level [44], [45], [90], significant amounts of prismatic have been reported. Typically, prismatic slip is observed at higher stress levels, which do not necessarily represent the lower stress levels that a titanium engine disk would actually experience in service. Therefore, it is reasonable to assume that the basal slip activity initiated at lower stress states may be more applicable to load shedding in Ti-6242. For other Ti alloys, such as Ti-6-4, it may be necessary to determine another strength metric to use in a strength-to-stiffness ratio driven segmentation protocol. As discussed in section 2.2.3, there is much debate about the CRSS of each slip family and therefore it makes a Taylor factor or normalized average Schmid factor strength metric difficult to estimate. Additional studies on the CRSS of a titanium alloy polycrystal could be a useful tool to improve estimates of strength produced from more averaged approaches. Also, it would be incredibly worthwhile to perform a similar study on Ti-6-4 or other titanium alloys of interest to determine the ideal strength metric for the specific alloys system.
- These redefined definitions of an MTR and the behavior of cooperative grains should be implemented into CPFEM dwell fatigue models for crack initiation. Currently, most models use the definitions of an MTR defined from fracture surface and crack growth

studies. Chapter 4 highlights the important difference when considering cooperative grain behavior and effective structural units for crack initiation and crack growth. Experimental studies are both expensive and time consuming compared to computational studies. By implementing the stricter parameters for MTR definitions relative to crack growth and validating models from the data sets in this study, the community may gain a vital understanding of the mechanisms and microstructural impacts relevant to dwell fatigue crack initiation and it's temperature dependence.

7.2.2 Microstructural Neighborhood

- There is evidence of a microstructural neighborhood effect where slip appears to slip first in grains well oriented for basal slip spatially near grains with a relatively higher strength-to-stiffness value, but whether this observation is a coincidence or mechanistically driven is still an open question. Additionally, the data clearly indicates that the neighborhood effect is not just about direct neighbors or hard/soft pairs but that there could be a sphere of influence where the mesoscale texture and location of microtextured regions that impacts the propensity of a basal oriented grain to slip. An experimental material with a differently processed microstructure where the basally soft grains are not preferentially nearby to hard grains and within hard MTRs would be helpful to determine if this a mechanistically driven relationship. A parametric analysis of the experimental data coupled with a modelling study to investigate the length scale of the proposed neighborhood effect is also important to identifying dwell susceptible material.

7.2.3 Time Dependent Experiments

- Finally, the microstructural weak-links identified in the present thesis and from the above suggested studies should be investigated in-situ with a time resolved technique. The plastic strain maps in this thesis suggests that the temperature dependence of the strain rate sensitivity is likely responsible for the temperature dependence of the dwell debit. The rate at which this dislocation evolution occurs is estimated to be on the order of tens of seconds to minutes [77], [116]. The SEM DIC strain fields collected in this thesis took over 22 hours to collect over the 4mm x 2.5mm. Therefore in-situ, fast data collection of the strain data in a susceptible area would likely lead to a better understanding of the mechanisms and temperature dependence of load shedding. Stinville et al. [117] recently tuned the parameters in an SEM DIC study to collect a 40 µm x 40 µm image in tens of seconds. This was achieved by reducing the resolution, dwell time and size of the image. The strain data collected with these reduced parameters accurately captured the slip activity detected in the samples from higher resolution imaging and processing conditions. In this proof of concept study, they found that in the Ti-7Al alloy dislocations were emitted in a more continuous way under a load hold than most other metallic materials which develop slip bands by dislocation motion with a very high propagation velocity that is difficult to capture experimentally [77], [117]. By using the full field findings in this thesis and the above proposed work, the identified regions of interest could be investigated with this time resolved technique at temperature to understand the impact of strain rate sensitivity on load shedding.

Appendices

Appendix A: Dream 3d MTR Segmentation Pipeline

Dream3d segmentation pipeline for MTR segmentation and associated statistics is below. The code remained constant through each iteration, while only the “Group MicroTexture Regions” and “Minimum Size” filters were altered to explore the parameter space for MTR grouping and segmentation.

```
{
  "00": {
    "CellAttributeMatrixName": "CellData",
    "CellEnsembleAttributeMatrixName": "CellEnsembleData",
    "DataContainerName": "ImageDataContainer",
    "FilterVersion": "6.4.27",
    "Filter_Human_Label": "Import EDAX EBSD Data (.ang)",
    "Filter_Name": "ReadAngData",
    "InputFile": "G:/20190819_SampleP_LowRes_SEMDIC/SampleP_ang.ang"
  },
  "01": {
    "DestinationArrayName": "Mask",
    "FilterVersion": "6.4.27",
    "Filter_Human_Label": "Threshold Objects",
    "Filter_Name": "MultiThresholdObjects",
    "SelectedThresholds": [
      {
        "Attribute Array Name": "Image Quality",
        "Attribute Matrix Name": "CellData",
        "Comparison Operator": 1,
        "Comparison Value": 0,
        "Data Container Name": "ImageDataContainer"
      }
    ]
```

```
},
"02": {
    "FilterVersion": "6.4.27",
    "Filter_Human_Label": "Convert Orientation Representation",
    "Filter_Name": "ConvertOrientations",
    "InputOrientationArrayPath": {
        "Attribute Matrix Name": "CellData",
        "Data Array Name": "EulerAngles",
        "Data Container Name": "ImageDataContainer"
    },
    "InputType": 0,
    "OutputOrientationArrayName": "Quats",
    "OutputType": 2
},
"03": {
    "ActiveArrayName": "Active",
    "CellFeatureAttributeMatrixName": "AlphaGlobData",
    "CellPhasesArrayPath": {
        "Attribute Matrix Name": "CellData",
        "Data Array Name": "Phases",
        "Data Container Name": "ImageDataContainer"
    },
    "CrystalStructuresArrayPath": {
        "Attribute Matrix Name": "CellEnsembleData",
        "Data Array Name": "CrystalStructures",
        "Data Container Name": "ImageDataContainer"
    },
    "FeatureIdsArrayName": "AlphaGlobIds",
    "FilterVersion": "6.4.27",
    "Filter_Human_Label": "Segment Features (Misorientation)",
```

```
        "Filter_Name": "EBSDSegmentFeatures",
        "GoodVoxelsArrayPath": {
            "Attribute Matrix Name": "CellData",
            "Data Array Name": "Mask",
            "Data Container Name": "ImageDataContainer"
        },
        "MisorientationTolerance": 2,
        "QuatsArrayPath": {
            "Attribute Matrix Name": "CellData",
            "Data Array Name": "Quats",
            "Data Container Name": "ImageDataContainer"
        },
        "UseGoodVoxels": 1
    },
    "04": {
        "BoundaryCellsArrayName": "BoundaryCells",
        "CellFeatureAttributeMatrixPath": {
            "Attribute Matrix Name": "AlphaGlobData",
            "Data Array Name": "",
            "Data Container Name": "ImageDataContainer"
        },
        "FeatureIdsArrayPath": {
            "Attribute Matrix Name": "CellData",
            "Data Array Name": "AlphaGlobIds",
            "Data Container Name": "ImageDataContainer"
        },
        "FilterVersion": "6.4.27",
        "Filter_Human_Label": "Find Feature Neighbors",
        "Filter_Name": "FindNeighbors",
        "NeighborListArrayName": "NeighborList",
```

```
        "NumNeighborsArrayName": "NumNeighbors",
        "SharedSurfaceAreaListArrayName": "SharedSurfaceAreaList",
        "StoreBoundaryCells": 0,
        "StoreSurfaceFeatures": 0,
        "SurfaceFeaturesArrayName": "SurfaceFeatures"
    },
    "05": {
        "EquivalentDiametersArrayName": "EquivalentDiameters",
        "FeatureAttributeMatrixName": {
            "Attribute Matrix Name": "AlphaGlobData",
            "Data Array Name": "",
            "Data Container Name": "ImageDataContainer"
        },
        "FeatureIdsArrayPath": {
            "Attribute Matrix Name": "CellData",
            "Data Array Name": "AlphaGlobIds",
            "Data Container Name": "ImageDataContainer"
        },
        "FilterVersion": "6.4.27",
        "Filter_Human_Label": "Find Feature Sizes",
        "Filter_Name": "FindSizes",
        "NumElementsArrayName": "NumElements",
        "SaveElementSizes": 0,
        "VolumesArrayName": "Volumes"
    },
    "06": {
        "CentroidsArrayPath": {
            "Attribute Matrix Name": "AlphaGlobData",
            "Data Array Name": "Centroids",
            "Data Container Name": "ImageDataContainer"
```

```
        },
        "FeatureIdsArrayPath": {
            "Attribute Matrix Name": "CellData",
            "Data Array Name": "AlphaGlobIds",
            "Data Container Name": "ImageDataContainer"
        },
        "FilterVersion": "6.4.27",
        "Filter_Human_Label": "Find Feature Centroids",
        "Filter_Name": "FindFeatureCentroids"
    },
    "07": {
        "CellPhasesArrayPath": {
            "Attribute Matrix Name": "CellData",
            "Data Array Name": "Phases",
            "Data Container Name": "ImageDataContainer"
        },
        "FeatureIdsArrayPath": {
            "Attribute Matrix Name": "CellData",
            "Data Array Name": "AlphaGlobIds",
            "Data Container Name": "ImageDataContainer"
        },
        "FeaturePhasesArrayPath": {
            "Attribute Matrix Name": "AlphaGlobData",
            "Data Array Name": "Phases",
            "Data Container Name": "ImageDataContainer"
        },
        "FilterVersion": "6.4.27",
        "Filter_Human_Label": "Find Feature Phases",
        "Filter_Name": "FindFeaturePhases"
    },
```

```
"08": {
    "CentroidsArrayPath": {
        "Attribute Matrix Name": "AlphaGlobData",
        "Data Array Name": "Centroids",
        "Data Container Name": "ImageDataContainer"
    },
    "EquivalentDiametersArrayPath": {
        "Attribute Matrix Name": "AlphaGlobData",
        "Data Array Name": "EquivalentDiameters",
        "Data Container Name": "ImageDataContainer"
    },
    "FeaturePhasesArrayPath": {
        "Attribute Matrix Name": "AlphaGlobData",
        "Data Array Name": "Phases",
        "Data Container Name": "ImageDataContainer"
    },
    "FilterVersion": "6.4.27",
    "Filter_Human_Label": "Find Feature Neighborhoods",
    "Filter_Name": "FindNeighborhoods",
    "MultiplesOfAverage": 1.5,
    "NeighborhoodListArrayName": "NeighborhoodList",
    "NeighborhoodsArrayName": "Neighborhoods"
},
"09": {
    "AvgEulerAnglesArrayPath": {
        "Attribute Matrix Name": "AlphaGlobData",
        "Data Array Name": "AvgEulerAngles",
        "Data Container Name": "ImageDataContainer"
    },
    "AvgQuatsArrayPath": {
```

```
            "Attribute Matrix Name": "AlphaGlobData",
            "Data Array Name": "AvgQuats",
            "Data Container Name": "ImageDataContainer"
        },
        "CellPhasesArrayPath": {
            "Attribute Matrix Name": "CellData",
            "Data Array Name": "Phases",
            "Data Container Name": "ImageDataContainer"
        },
        "CrystalStructuresArrayPath": {
            "Attribute Matrix Name": "CellEnsembleData",
            "Data Array Name": "CrystalStructures",
            "Data Container Name": "ImageDataContainer"
        },
        "FeatureIdsArrayPath": {
            "Attribute Matrix Name": "CellData",
            "Data Array Name": "AlphaGlobIds",
            "Data Container Name": "ImageDataContainer"
        },
        "FilterVersion": "6.4.27",
        "Filter_Human_Label": "Find Feature Average Orientations",
        "Filter_Name": "FindAvgOrientations",
        "QuatsArrayPath": {
            "Attribute Matrix Name": "CellData",
            "Data Array Name": "Quats",
            "Data Container Name": "ImageDataContainer"
        }
    },
    "10": {
        "ActiveArrayName": "Active",
```

```
"AvgQuatsArrayPath": {
    "Attribute Matrix Name": "AlphaGlobData",
    "Data Array Name": "AvgQuats",
    "Data Container Name": "ImageDataContainer"
},
"CAxisTolerance": 20,
"CellParentIdsArrayName": "MTRIds",
"ContiguousNeighborListArrayPath": {
    "Attribute Matrix Name": "AlphaGlobData",
    "Data Array Name": "NeighborList",
    "Data Container Name": "ImageDataContainer"
},
"CrystalStructuresArrayPath": {
    "Attribute Matrix Name": "CellEnsembleData",
    "Data Array Name": "CrystalStructures",
    "Data Container Name": "ImageDataContainer"
},
"FeatureIdsArrayPath": {
    "Attribute Matrix Name": "CellData",
    "Data Array Name": "AlphaGlobIds",
    "Data Container Name": "ImageDataContainer"
},
"FeatureParentIdsArrayName": "MTRIds",
"FeaturePhasesArrayPath": {
    "Attribute Matrix Name": "AlphaGlobData",
    "Data Array Name": "Phases",
    "Data Container Name": "ImageDataContainer"
},
"FilterVersion": "6.4.27",
"Filter_Human_Label": "Group MicroTexture Regions",
```

```
      "Filter_Name": "GroupMicroTextureRegions",
      "NewCellFeatureAttributeMatrixName": "MTRData",
      "NonContiguousNeighborListArrayPath": {
        "Attribute Matrix Name": "AlphaGlobData",
        "Data Array Name": "NeighborhoodList",
        "Data Container Name": "ImageDataContainer"
      },
      "UseNonContiguousNeighbors": 1,
      "UseRunningAverage": 1,
      "VolumesArrayPath": {
        "Attribute Matrix Name": "AlphaGlobData",
        "Data Array Name": "Volumes",
        "Data Container Name": "ImageDataContainer"
      }
    },
    "11": {
      "EquivalentDiametersArrayName": "MTR_EquivalentDiameters_uncheck",
      "FeatureAttributeMatrixName": {
        "Attribute Matrix Name": "MTRData",
        "Data Array Name": "",
        "Data Container Name": "ImageDataContainer"
      },
      "FeatureIdsArrayPath": {
        "Attribute Matrix Name": "CellData",
        "Data Array Name": "MTRIds",
        "Data Container Name": "ImageDataContainer"
      },
      "FilterVersion": "6.4.27",
      "Filter_Human_Label": "Find Feature Sizes",
      "Filter_Name": "FindSizes",
```

```
            "NumElementsArrayName": "MTR_NumElements_uncheck",
            "SaveElementSizes": 0,
            "VolumesArrayName": "MTR_Volumes_uncheck"
        },
        "12": {
            "ApplyToSinglePhase": 0,
            "FeatureIdsArrayPath": {
                "Attribute Matrix Name": "CellData",
                "Data Array Name": "MTRIds",
                "Data Container Name": "ImageDataContainer"
            },
            "FeaturePhasesArrayPath": {
                "Attribute Matrix Name": "CellFeatureData",
                "Data Array Name": "Phases",
                "Data Container Name": "ImageDataContainer"
            },
            "FilterVersion": "6.4.27",
            "Filter_Human_Label": "Minimum Size",
            "Filter_Name": "MinSize",
            "MinAllowedFeatureSize": 25,
            "NumCellsArrayPath": {
                "Attribute Matrix Name": "MTRData",
                "Data Array Name": "MTR_NumElements_uncheck",
                "Data Container Name": "ImageDataContainer"
            },
            "PhaseNumber": 0
        },
        "13": {
            "EquivalentDiametersArrayName": "MTR_EquivalentDiameters",
            "FeatureAttributeMatrixName": {
```

```
            "Attribute Matrix Name": "MTRData",
            "Data Array Name": "",
            "Data Container Name": "ImageDataContainer"
        },
        "FeatureIdsArrayPath": {
            "Attribute Matrix Name": "CellData",
            "Data Array Name": "MTRIds",
            "Data Container Name": "ImageDataContainer"
        },
        "FilterVersion": "6.4.27",
        "Filter_Human_Label": "Find Feature Sizes",
        "Filter_Name": "FindSizes",
        "NumElementsArrayName": "MTR_NumElements",
        "SaveElementSizes": 0,
        "VolumesArrayName": "MTR_Volumes"
    },
    "14": {
        "BoundaryCellsArrayName": "BoundaryCells",
        "CellFeatureAttributeMatrixPath": {
            "Attribute Matrix Name": "MTRData",
            "Data Array Name": "",
            "Data Container Name": "ImageDataContainer"
        },
        "FeatureIdsArrayPath": {
            "Attribute Matrix Name": "CellData",
            "Data Array Name": "MTRIds",
            "Data Container Name": "ImageDataContainer"
        },
        "FilterVersion": "6.4.27",
        "Filter_Human_Label": "Find Feature Neighbors",
```

```
        "Filter_Name": "FindNeighbors",
        "NeighborListArrayName": "MTR_NeighborList",
        "NumNeighborsArrayName": "MTR_NumNeighbors",
        "SharedSurfaceAreaListArrayName": "MTR_SharedSurfaceAreaList",
        "StoreBoundaryCells": 0,
        "StoreSurfaceFeatures": 0,
        "SurfaceFeaturesArrayName": "SurfaceFeatures"
    },
    "15": {
        "CellPhasesArrayPath": {
            "Attribute Matrix Name": "CellData",
            "Data Array Name": "Phases",
            "Data Container Name": "ImageDataContainer"
        },
        "FeatureIdsArrayPath": {
            "Attribute Matrix Name": "CellData",
            "Data Array Name": "MTRIds",
            "Data Container Name": "ImageDataContainer"
        },
        "FeaturePhasesArrayPath": {
            "Attribute Matrix Name": "MTRData",
            "Data Array Name": "MTR_Phases",
            "Data Container Name": "ImageDataContainer"
        },
        "FilterVersion": "6.4.27",
        "Filter_Human_Label": "Find Feature Phases",
        "Filter_Name": "FindFeaturePhases"
    },
    "16": {
        "AvgEulerAnglesArrayPath": {
```

```
            "Attribute Matrix Name": "MTRData",
            "Data Array Name": "MTR_EulerAngles",
            "Data Container Name": "ImageDataContainer"
        },
        "AvgQuatsArrayPath": {
            "Attribute Matrix Name": "MTRData",
            "Data Array Name": "MTR_AvgQuats",
            "Data Container Name": "ImageDataContainer"
        },
        "CellPhasesArrayPath": {
            "Attribute Matrix Name": "CellData",
            "Data Array Name": "Phases",
            "Data Container Name": "ImageDataContainer"
        },
        "CrystalStructuresArrayPath": {
            "Attribute Matrix Name": "CellEnsembleData",
            "Data Array Name": "CrystalStructures",
            "Data Container Name": "ImageDataContainer"
        },
        "FeatureIdsArrayPath": {
            "Attribute Matrix Name": "CellData",
            "Data Array Name": "MTRIds",
            "Data Container Name": "ImageDataContainer"
        },
        "FilterVersion": "6.4.27",
        "Filter_Human_Label": "Find Feature Average Orientations",
        "Filter_Name": "FindAvgOrientations",
        "QuatsArrayPath": {
            "Attribute Matrix Name": "CellData",
            "Data Array Name": "Quats",
```

```
            "Data Container Name": "ImageDataContainer"
        }
    },
    "17": {
        "AvgMisorientationsArrayName": "MTR_AvgMisorientations",
        "AvgQuatsArrayPath": {
            "Attribute Matrix Name": "MTRData",
            "Data Array Name": "MTR_AvgQuats",
            "Data Container Name": "ImageDataContainer"
        },
        "CrystalStructuresArrayPath": {
            "Attribute Matrix Name": "CellEnsembleData",
            "Data Array Name": "CrystalStructures",
            "Data Container Name": "ImageDataContainer"
        },
        "FeaturePhasesArrayPath": {
            "Attribute Matrix Name": "MTRData",
            "Data Array Name": "MTR_Phases",
            "Data Container Name": "ImageDataContainer"
        },
        "FilterVersion": "6.4.27",
        "Filter_Human_Label": "Find Feature Neighbor Misorientations",
        "Filter_Name": "FindMisorientations",
        "FindAvgMisors": 1,
        "MisorientationListArrayName": "MTR_MisorientationList",
        "NeighborListArrayPath": {
            "Attribute Matrix Name": "MTRData",
            "Data Array Name": "MTR_NeighborList",
            "Data Container Name": "ImageDataContainer"
        }
```

```
},
"18": {
    "CentroidsArrayPath": {
        "Attribute Matrix Name": "MTRData",
        "Data Array Name": "MTR_Centroids",
        "Data Container Name": "ImageDataContainer"
    },
    "FeatureIdsArrayPath": {
        "Attribute Matrix Name": "CellData",
        "Data Array Name": "MTRIds",
        "Data Container Name": "ImageDataContainer"
    },
    "FilterVersion": "6.4.27",
    "Filter_Human_Label": "Find Feature Centroids",
    "Filter_Name": "FindFeatureCentroids"
},
"19": {
    "AspectRatiosArrayName": "MTR_AspectRatios",
    "AxisEulerAnglesArrayName": "MTR_AxisEulerAngles",
    "AxisLengthsArrayName": "MTR_AxisLengths",
    "CellFeatureAttributeMatrixName": {
        "Attribute Matrix Name": "MTRData",
        "Data Array Name": "",
        "Data Container Name": "ImageDataContainer"
    },
    "CentroidsArrayPath": {
        "Attribute Matrix Name": "MTRData",
        "Data Array Name": "MTR_Centroids",
        "Data Container Name": "ImageDataContainer"
    },
```

```
        "FeatureIdsArrayPath": {
            "Attribute Matrix Name": "CellData",
            "Data Array Name": "MTRIds",
            "Data Container Name": "ImageDataContainer"
        },
        "FilterVersion": "6.4.27",
        "Filter_Human_Label": "Find Feature Shapes",
        "Filter_Name": "FindShapes",
        "Omega3sArrayName": "Omega3s",
        "VolumesArrayName": "Volumes"
    },
    "20": {
        "AvgCAxisMisalignmentsArrayName": "AvgCAxisMisalignments",
        "AvgQuatsArrayPath": {
            "Attribute Matrix Name": "MTRData",
            "Data Array Name": "MTR_AvgQuats",
            "Data Container Name": "ImageDataContainer"
        },
        "CAxisMisalignmentListArrayName": "MTR_CAxisMisalignmentList",
        "CrystalStructuresArrayPath": {
            "Attribute Matrix Name": "CellEnsembleData",
            "Data Array Name": "CrystalStructures",
            "Data Container Name": "ImageDataContainer"
        },
        "FeaturePhasesArrayPath": {
            "Attribute Matrix Name": "MTRData",
            "Data Array Name": "MTR_Phases",
            "Data Container Name": "ImageDataContainer"
        },
        "FilterVersion": "6.4.27",
```

```
        "Filter_Human_Label": "Find Feature Neighbor C-Axis Misalignments",
        "Filter_Name": "FindFeatureNeighborCAxisMisalignments",
        "FindAvgMisals": 0,
        "NeighborListArrayPath": {
            "Attribute Matrix Name": "MTRData",
            "Data Array Name": "MTR_NeighborList",
            "Data Container Name": "ImageDataContainer"
        }
    },
    "21": {
        "AvgQuatsArrayPath": {
            "Attribute Matrix Name": "MTRData",
            "Data Array Name": "MTR_AvgQuats",
            "Data Container Name": "ImageDataContainer"
        },
        "CellPhasesArrayPath": {
            "Attribute Matrix Name": "CellData",
            "Data Array Name": "Phases",
            "Data Container Name": "ImageDataContainer"
        },
        "CrystalStructuresArrayPath": {
            "Attribute Matrix Name": "CellEnsembleData",
            "Data Array Name": "CrystalStructures",
            "Data Container Name": "ImageDataContainer"
        },
        "FeatureAvgMisorientationsArrayName": "MTR_FeatureAvgMisorientations",
        "FeatureIdsArrayPath": {
            "Attribute Matrix Name": "CellData",
            "Data Array Name": "MTRIds",
            "Data Container Name": "ImageDataContainer"
```

```
    },
    "FeatureReferenceMisorientationsArrayName": "MTR_FeatureReferenceMisorientations",
    "FilterVersion": "6.4.27",
    "Filter_Human_Label": "Find Feature Reference Misorientations",
    "Filter_Name": "FindFeatureReferenceMisorientations",
    "GBEuclideanDistancesArrayPath": {
      "Attribute Matrix Name": "CellData",
      "Data Array Name": "GBEuclideanDistances",
      "Data Container Name": "ImageDataContainer"
    },
    "QuatsArrayPath": {
      "Attribute Matrix Name": "CellData",
      "Data Array Name": "Quats",
      "Data Container Name": "ImageDataContainer"
    },
    "ReferenceOrientation": 0
  },
  "22": {
    "AvgCAxesArrayPath": {
      "Attribute Matrix Name": "MTRData",
      "Data Array Name": "Avg_CAxis_MTRs",
      "Data Container Name": "ImageDataContainer"
    },
    "FeatureIdsArrayPath": {
      "Attribute Matrix Name": "CellData",
      "Data Array Name": "MTRIds",
      "Data Container Name": "ImageDataContainer"
    },
    "FilterVersion": "6.4.27",
    "Filter_Human_Label": "Find Average C-Axis Orientations",
```

```
        "Filter_Name": "FindAvgCAxes",
        "QuatsArrayPath": {
            "Attribute Matrix Name": "CellData",
            "Data Array Name": "Quats",
            "Data Container Name": "ImageDataContainer"
        }
    },
    "23": {
        "AvgCAxesArrayPath": {
            "Attribute Matrix Name": "MTRData",
            "Data Array Name": "Avg_CAxis_MTRs",
            "Data Container Name": "ImageDataContainer"
        },
        "CellPhasesArrayPath": {
            "Attribute Matrix Name": "CellData",
            "Data Array Name": "Phases",
            "Data Container Name": "ImageDataContainer"
        },
        "FeatureAvgCAxisMisorientationsArrayName": "MTR_FeatureAvgCAxisMisorientations",
        "FeatureIdsArrayPath": {
            "Attribute Matrix Name": "CellData",
            "Data Array Name": "MTRIds",
            "Data Container Name": "ImageDataContainer"
        },
        "FeatureReferenceCAxisMisorientationsArrayName":
"MTR_FeatureReferenceCAxisMisorientations",
        "FeatureStdevCAxisMisorientationsArrayName": "MTR_FeatureStdevCAxisMisorientations",
        "FilterVersion": "6.4.27",
        "Filter_Human_Label": "Find Feature Reference C-Axis Misalignments",
        "Filter_Name": "FindFeatureReferenceCAxisMisorientations",
```

```
        "QuatsArrayPath": {
            "Attribute Matrix Name": "CellData",
            "Data Array Name": "Quats",
            "Data Container Name": "ImageDataContainer"
        }
    },
    "24": {
        "CellEulerAnglesArrayPath": {
            "Attribute Matrix Name": "CellData",
            "Data Array Name": "EulerAngles",
            "Data Container Name": "ImageDataContainer"
        },
        "CellIPFColorsArrayName": "IPFColor_map",
        "CellPhasesArrayPath": {
            "Attribute Matrix Name": "CellData",
            "Data Array Name": "Phases",
            "Data Container Name": "ImageDataContainer"
        },
        "CrystalStructuresArrayPath": {
            "Attribute Matrix Name": "CellEnsembleData",
            "Data Array Name": "CrystalStructures",
            "Data Container Name": "ImageDataContainer"
        },
        "FilterVersion": "6.4.27",
        "Filter_Human_Label": "Generate IPF Colors",
        "Filter_Name": "GenerateIPFColors",
        "GoodVoxelsArrayPath": {
            "Attribute Matrix Name": "",
            "Data Array Name": "",
            "Data Container Name": ""
```

```
        },
        "ReferenceDir": {
            "x": 0,
            "y": 0,
            "z": 1
        },
        "UseGoodVoxels": 0
    },
    "25": {
        "CellEulerAnglesArrayPath": {
            "Attribute Matrix Name": "MTRData",
            "Data Array Name": "MTR_EulerAngles",
            "Data Container Name": "ImageDataContainer"
        },
        "CellIPFColorsArrayName": "IPFColor_MTR",
        "CellPhasesArrayPath": {
            "Attribute Matrix Name": "MTRData",
            "Data Array Name": "MTR_Phases",
            "Data Container Name": "ImageDataContainer"
        },
        "CrystalStructuresArrayPath": {
            "Attribute Matrix Name": "CellEnsembleData",
            "Data Array Name": "CrystalStructures",
            "Data Container Name": "ImageDataContainer"
        },
        "FilterVersion": "6.4.27",
        "Filter_Human_Label": "Generate IPF Colors",
        "Filter_Name": "GenerateIPFColors",
        "GoodVoxelsArrayPath": {
            "Attribute Matrix Name": "",
```

```
      "Data Array Name": "",
      "Data Container Name": ""
    },
    "ReferenceDir": {
      "x": 0,
      "y": 0,
      "z": 1
    },
    "UseGoodVoxels": 0
  },
  "26": {
    "FilterVersion": "1.0.67",
    "Filter_Human_Label": "Write DREAM.3D Data File",
    "Filter_Name": "DataContainerWriter",
    "OutputFile":
"G:\\20190819_SampleP_LowRes_SEMDIC\\SampleP_Paper2_smallMTR_CaxisStd\\SampleP_tol20_minsize25.dream3d",
    "WriteTimeSeries": 0,
    "WriteXdmfFile": 1
  },
  "27": {
    "CellFeatureAttributeMatrixPath": {
      "Attribute Matrix Name": "MTRData",
      "Data Array Name": "",
      "Data Container Name": "ImageDataContainer"
    },
    "DelimiterChoice": 0,
    "FeatureDataFile":
"G:\\20190819_SampleP_LowRes_SEMDIC\\SampleP_Paper2_smallMTR_CaxisStd\\SampleP__MTRTol20_Cleaned_RmTempFatigue_WithNeighborData_MTRData.csv",
    "FilterVersion": "1.0.67",
    "Filter_Human_Label": "Export Feature Data as CSV File",
```

```
        "Filter_Name": "FeatureDataCSVWriter",
        "WriteNeighborListData": 1
    },
    "28": {
        "CellFeatureAttributeMatrixPath": {
            "Attribute Matrix Name": "AlphaGlobData",
            "Data Array Name": "",
            "Data Container Name": "ImageDataContainer"
        },
        "DelimiterChoice": 0,
        "FeatureDataFile":
"G:\\20190819_SampleP_LowRes_SEMDIC\\SampleP_Paper2_smallMTR_CaxisStd\\Sample
P_MTRTol20_Cleaned_RmTempFatigue_WithNeighborData_GlobData.csv",
        "FilterVersion": "1.0.67",
        "Filter_Human_Label": "Export Feature Data as CSV File",
        "Filter_Name": "FeatureDataCSVWriter",
        "WriteNeighborListData": 0
    },
    "29": {
        "Delimiter": 0,
        "FileExtension": ".txt",
        "FilterVersion": "1.0.67",
        "Filter_Human_Label": "Export ASCII Data",
        "Filter_Name": "WriteASCIIData",
        "MaxValPerLine": 1,
        "OutputPath": "G:\\20190819_SampleP_LowRes_SEMDIC\\SampleP_Paper2_smallMTR_CaxisStd",
        "SelectedDataArrayPaths": [
            {
                "Attribute Matrix Name": "CellData",
                "Data Array Name": "MTRIds",
                "Data Container Name": "ImageDataContainer"
```

```
},
{
  "Attribute Matrix Name": "CellData",
  "Data Array Name": "X Position",
  "Data Container Name": "ImageDataContainer"
},
{
  "Attribute Matrix Name": "CellData",
  "Data Array Name": "Y Position",
  "Data Container Name": "ImageDataContainer"
},
{
  "Attribute Matrix Name": "CellData",
  "Data Array Name": "MTR_FeatureReferenceMisorientations",
  "Data Container Name": "ImageDataContainer"
},
{
  "Attribute Matrix Name": "CellData",
  "Data Array Name": "EulerAngles",
  "Data Container Name": "ImageDataContainer"
},
{
  "Attribute Matrix Name": "CellData",
  "Data Array Name": "AlphaGlobIds",
  "Data Container Name": "ImageDataContainer"
},
{
  "Attribute Matrix Name": "CellData",
  "Data Array Name": "IPFColor_map",
  "Data Container Name": "ImageDataContainer"
```

```
        }
    ]
},
"30": {
    "Delimiter": 0,
    "FileExtension": ".txt",
    "FilterVersion": "1.0.67",
    "Filter_Human_Label": "Export ASCII Data",
    "Filter_Name": "WriteASCIIData",
    "MaxValPerLine": 1,
    "OutputPath": "G:\\20190819_SampleP_LowRes_SEMDIC\\SampleP_Paper2_smallMTR_CaxisStd",
    "SelectedDataArrayPaths": [
        {
            "Attribute Matrix Name": "MTRData",
            "Data Array Name": "MTR_EquivalentDiameters",
            "Data Container Name": "ImageDataContainer"
        },
        {
            "Attribute Matrix Name": "MTRData",
            "Data Array Name": "MTR_EulerAngles",
            "Data Container Name": "ImageDataContainer"
        },
        {
            "Attribute Matrix Name": "MTRData",
            "Data Array Name": "MTR_AvgMisorientations",
            "Data Container Name": "ImageDataContainer"
        },
        {
            "Attribute Matrix Name": "MTRData",
            "Data Array Name": "Avg_CAxis_MTRs",
```

```
    "Data Container Name": "ImageDataContainer"
  },
  {
    "Attribute Matrix Name": "MTRData",
    "Data Array Name": "MTR_AvgQuats",
    "Data Container Name": "ImageDataContainer"
  },
  {
    "Attribute Matrix Name": "MTRData",
    "Data Array Name": "MTR_FeatureAvgMisorientations",
    "Data Container Name": "ImageDataContainer"
  },
  {
    "Attribute Matrix Name": "MTRData",
    "Data Array Name": "MTR_Centroids",
    "Data Container Name": "ImageDataContainer"
  },
  {
    "Attribute Matrix Name": "MTRData",
    "Data Array Name": "MTR_AspectRatios",
    "Data Container Name": "ImageDataContainer"
  },
  {
    "Attribute Matrix Name": "MTRData",
    "Data Array Name": "MTR_NumNeighbors",
    "Data Container Name": "ImageDataContainer"
  },
  {
    "Attribute Matrix Name": "MTRData",
    "Data Array Name": "MTR_AxisLengths",
```

```
                "Data Container Name": "ImageDataContainer"
            },
            {
                "Attribute Matrix Name": "MTRData",
                "Data Array Name": "IPFColor_MTR",
                "Data Container Name": "ImageDataContainer"
            },
            {
                "Attribute Matrix Name": "MTRData",
                "Data Array Name": "MTR_FeatureStdevCAxisMisorientations",
                "Data Container Name": "ImageDataContainer"
            },
            {
                "Attribute Matrix Name": "MTRData",
                "Data Array Name": "MTR_FeatureAvgCAxisMisorientations",
                "Data Container Name": "ImageDataContainer"
            }
        ]
    },
    "PipelineBuilder": {
        "Name": "20170627_MTRNonContiguousSegmentation_AngFile_WithMTRstats",
        "Number_Filters": 31,
        "Version": 6
    }
}
```

Bibliography

[1] M. A. Cuddihy, A. Stapleton, S. Williams, and F. P. E. Dunne, “On cold dwell facet fatigue in aero-engine components,” *Int. J. Fatigue*, vol. 97, pp. 177–189, 2016.

[2] France-BEA, “Accident to the AIRBUS A380-861 equipped with Engine Alliance GP7270 engines registered F-HPJE operated by Air France on 30 September 2017 in cruise over Greenland (Denmark),” 2020.

[3] NTSB, “NTSB-Accident Reports,” *ntsb.gov/investigations/AccidentReports/*, 2020. .

[4] J. Gong and A. J. Wilkinson, “Anisotropy in the plastic flow properties of single-crystal a titanium determined from micro-cantilever beams,” *Acta Mater.*, vol. 57, no. 19, pp. 5693–5705, 2009.

[5] W. J. Evans and M. R. Bache, “Dwell-sensitive fatigue under biaxial loads in the near-alpha titanium alloy IMI685,” *Int. J. Fatigue*, vol. 16, no. 7, pp. 443–452, 1994.

[6] M. R. Bache, “A review of dwell sensitive fatigue in titanium alloys: The role of microstructure, texture and operating conditions,” in *International Journal of Fatigue*, 2003, vol. 25, no. 9–11, pp. 1079–1087.

[7] V. Hasija, S. Ghosh, M. J. Mills, and D. S. Joseph, “Deformation and creep modeling in polycrystalline Ti–6Al alloys,” *Acta Mater.*, vol. 51, no. 15, pp. 4533–4549, Sep. 2003.

[8] J. Qiu *et al.*, “A Comparative Study on Dwell Fatigue of Ti-6Al-2Sn-4Zr-xMo (x = 2 to 6) Alloys on a Microstructure-Normalized Basis,” *Metall. Mater. Trans. A Phys. Metall. Mater. Sci.*, vol. 45, no. 13, pp. 6075–6087, 2014.

[9] V. Sinha, J. E. Spowart, M. J. Mills, and J. C. Williams, “Observations on the faceted initiation site in the dwell-fatigue tested Ti-6242 alloy: Crystallographic orientation and size effects,” *Metall. Mater. Trans. A Phys. Metall. Mater. Sci.*, vol. 37, no. 5, pp. 1507–1518, May 2006.

[10] A. L. Pilchak, J. C. Tucker, and T. J. Weihing, “Determining the Probability of Occurrence of Rarely Occurring Microstructural Configurations for Titanium Dwell Fatigue,” in *From Microstructure Investigations to Multiscale Modeling*, Hoboken, NJ, USA: John Wiley & Sons, Inc., 2017, pp. 41–66.

[11] A. P. Woodfield, M. D. Gorman, J. A. Sutliff, and R. R. Corderman, “Effect of Microstructure on Dwell Fatigue Behavior of Ti-6242,” *Titanium’95 Sci. Technol.*, pp. 1116–1123, 1995.

[12] A. P. Woodfield, M. D. Gorman, J. A. Sutliff, and R. R. Corderman, “Effect of Microstructure on Dwell Fatigue Behavior of Ti-6242,” in *TMS Fall Meeting ’98*, 1998, pp. 111–118.

[13] A. L. Pilchak, A. H. Young, and J. C. Williams, “Stress corrosion cracking facet crystallography of Ti-8Al-1Mo-1V,” *Corros. Sci.*, vol. 52, no. 10, pp. 3287–3296, 2010.

[14] D. Ozturk, A. Shahba, and S. Ghosh, “Crystal plasticity FE study of the effect of thermo-mechanical loading on fatigue crack nucleation in titanium alloys,” *Fatigue Fract. Eng. Mater. Struct.*, vol. 39, no. 6, pp. 752–769, 2016.

[15] Z. Zhang, M. A. Cuddihy, and F. P. E. Dunne, “On rate-dependent polycrystal

deformation: the temperature sensitivity of cold dwell fatigue," *Proc. R. Soc. A Math. Phys. Eng. Sci.*, vol. 471, no. 2181, Sep. 2015.

[16] Z. Zheng, D. S. Balint, and F. P. E. Dunne, "Investigation of slip transfer across HCP grain boundaries with application to cold dwell facet fatigue," *Acta Mater.*, vol. 127, pp. 1–18, 2017.

[17] G. Lütjering and J. C. Williams, *Titanium*, 2nd ed. Verlag Berlin Heidelberg : Springer, 2007.

[18] J. C. Schuster and M. Palm, "Reassessment of the binary aluminum-titanium phase diagram," *J. Phase Equilibria Diffus.*, vol. 27, no. 3, pp. 255–277, 2006.

[19] D. C. Leyens and D. M. Peters, *Titanium and Titanium Alloys*. Wiley, 2003.

[20] R. D. Doherty *et al.*, "Current issues in recrystallization: A review," *Mater. Sci. Eng. A*, vol. 238, no. 2, pp. 219–274, 1997.

[21] L. Germain, N. Gey, M. Humbert, P. Vo, M. Jahazi, and P. Bocher, "Texture heterogeneities induced by subtransus processing of near a titanium alloys," vol. 56, pp. 4298–4308, 2008.

[22] F. Bridier, P. Villechaise, and J. Mendez, "Slip and fatigue crack formation processes in an a / b titanium alloy in relation to crystallographic texture on different scales," vol. 56, pp. 3951–3962, 2008.

[23] I. Lonardelli, N. Gey, H. R. Wenk, M. Humbert, S. C. Vogel, and L. Lutterotti, "In situ observation of texture evolution during α → β and β → α phase transformations in titanium alloys investigated by neutron diffraction," *Acta Mater.*, vol. 55, no. 17, pp. 5718–5727, 2007.

[24] A. L. Pilchak, J. Shank, J. C. Tucker, S. Srivatsa, P. N. Fagin, and S. L. Semiatin, "A dataset for the development, verification, and validation of microstructure-sensitive process models for near-alpha titanium alloys," *Integr. Mater. Manuf. Innov.*, vol. 5, no. 1, pp. 259–276, 2016.

[25] J. C. Williams, J. C. Williams, R. G. Baggerly, R. G. Baggerly, N. E. Paton, and N. E. Paton, "Deformation behavior of HCPTi-Al alloy single crystals," *Metall. Mater. Trans. a-Physical Metall. Mater. Sci.*, vol. 33, no. 3, pp. 837–850, 2002.

[26] J. C. Williams, A. W. Sommer, and P. P. Tung, "The influence of oxygen concentration on the internal stress and dislocation arrangements in α titanium," *Metall. Trans.*, vol. 3, no. 11, pp. 2979–2984, 1972.

[27] A. ZARKADES and F. R. LARSON, *Elasticity of Titanium Sheet Alloys*. Pergamon Press Ltd, 1970.

[28] H. Conrad, B. de Meester, M. Döner, and K. Okazaki, "Strengthening of Alpha Titanium by the Interstitial Solutes C, N, and O," in *Physics of Solid Solution Strengthening*, Boston, MA: Springer New York, 1975, pp. 1–45.

[29] P. G. Partridge, "The crystallography and deformation modes of hexagonal close-packed metals," *Metall. Rev.*, vol. 12, no. 1, pp. 169–194, 1967.

[30] M. H. Yoo, "Slip, twinning, and fracture in hexagonal close-packed metals," *Metall. Trans. A*, vol. 12, no. 3, pp. 409–418, 1981.

[31] S. Zaefferer, "A study of active deformation systems in titanium alloys: Dependence on," *Mater. Sci. Eng. A*, vol. 344, no. 1–2, pp. 20–30, 2003.

[32] J. J. Fundenberger, M. J. Philippe, F. Wagner, and C. Esling, "Modelling and prediction of mechanical properties for materials with hexagonal symmetry (zinc, titanium and zirconium alloys)," *Acta Mater.*, vol. 45, no. 10, pp. 4041–4055, 1997.

[33] T. R. Bieler and S. L. Semiatin, "The origins of heterogeneous deformation during primary hot working of Ti-6Al-4V," *Int. J. Plast.*, vol. 18, no. 9, pp. 1165–1189, 2002.

[34] X. Wu, S. R. Kalidindi, C. Necker, and A. A. Salem, "Prediction of crystallographic texture evolution and anisotropic stress-strain curves during large plastic strains in high purity α-titanium using a Taylor-type crystal plasticity model," *Acta Mater.*, vol. 55, no. 2, pp. 423–432, 2007.

[35] A. Poty *et al.*, "Classification of the critical resolved shear stress in the hexagonal-close-packed materials by atomic simulation: Application to -zirconium and -titanium," *Journal of Applied Physics*, vol. 110, no. 1. 2011.

[36] A. A. Salem, S. R. Kalidindi, and S. L. Semiatin, "Strain hardening due to deformation twinning in α-titanium: Constitutive relations and crystal-plasticity modeling," *Acta Mater.*, vol. 53, no. 12, pp. 3495–3502, 2005.

[37] S. Balasubramanian and L. Anand, "Plasticity of initially textured hexagonal polycrystals at high homologous temperatures: Application to titanium," *Acta Mater.*, vol. 50, no. 1, pp. 133–148, 2002.

[38] I. P. Jones and W. B. Hutchinson, "Stress-state dependence of slip in Titanium-6Al-4V and other H.C.P. metals," *Acta Metall.*, vol. 29, no. 6, pp. 951–968, 1981.

[39] J. A. Medina Perilla and J. Gil Sevillano, "Two-dimensional sections of the yield locus of a Ti6%Al4%V alloy with a strong transverse-type crystallographic α-texture," *Mater. Sci. Eng. A*, vol. 201, no. 1–2, pp. 103–110, 1995.

[40] T. Dick and G. Cailletaud, "Fretting modelling with a crystal plasticity model of Ti6Al4V," *Comput. Mater. Sci.*, vol. 38, no. 1, pp. 113–125, 2006.

[41] F. Bridier, P. Villechaise, and J. Mendez, "Analysis of the different slip systems activated by tension in a α/β titanium alloy in relation with local crystallographic orientation," *Acta Mater.*, vol. 53, no. 3, pp. 555–567, 2005.

[42] H. Li, D. E. Mason, T. R. Bieler, C. J. Boehlert, and M. A. Crimp, "Methodology for estimating the critical resolved shear stress ratios of α-phase Ti using EBSD-based trace analysis," *Acta Mater.*, vol. 61, no. 20, pp. 7555–7567, 2013.

[43] G. Venkatramani, S. Ghosh, and M. Mills, "A size-dependent crystal plasticity finite-element model for creep and load shedding in polycrystalline titanium alloys," *Acta Mater.*, vol. 55, no. 11, pp. 3971–3986, 2007.

[44] S. Hémery and P. Villechaise, "Comparison of slip system activation in Ti-6Al-2Sn-4Zr-2Mo and Ti-6Al-2Sn-4Zr-6Mo under tensile, fatigue and dwell-fatigue loadings," *Mater. Sci. Eng. A*, vol. 697, no. March, pp. 177–183, Jun. 2017.

[45] C. Lavogiez, S. Hémery, and P. Villechaise, "Analysis of deformation mechanisms operating under fatigue and dwell-fatigue loadings in an α/β titanium alloy," *Int. J. Fatigue*, vol. 131, no. October 2019, p. 105341, 2020.

[46] D. Deka, D. S. Joseph, S. Ghosh, and M. J. Mills, "Crystal Plasticity Modeling of Deformation and Creep in Polycrystalline Ti-6242," *Metall. Mater. Trans. A*, vol. 37A, pp. 1371–1388, 2006.

[47] T. B. Britton, F. P. E. Dunne, and A. J. Wilkinson, "On the mechanistic basis of deformation at the microscale in hexagonal close-packed metals," *Proc. R. Soc. A Math. Phys. Eng. Sci.*, vol. 471, no. 2178, pp. 20140881–20140881, 2015.

[48] Z. Zheng, D. S. Balint, and F. P. E. Dunne, "Rate sensitivity in discrete dislocation plasticity in hexagonal close- packed crystals," *Acta Mater.*, vol. 107, pp. 17–26, 2016.

[49] G. Gottstein, *Physical foundations of materials science*, vol. 42, no. 05. 2005.

[50] A. W. Thompson and B. C. Odegard, “The influence of microstructure on low temperature creep of ti-5 al-2.5 sn,” *Metall. Trans.*, vol. 4, no. 4, pp. 899–908, 1973.

[51] B. C. Odegard and A. W. Thompson, “LOW TEMPERATURE CREEP OF Ti-6 Al-4 V.,” *Met. Trans*, vol. 5, no. 5, pp. 1207–1213, 1974.

[52] G. Venkataramani, K. Kirane, and S. Ghosh, “Microstructural parameters affecting creep induced load shedding in Ti-6242 by a size dependent crystal plasticity FE model,” vol. 24, pp. 428–454, 2008.

[53] G. S. Daehn, “Modeling thermally activated deformation with a variety of obstacles, and its application to creep transients,” *Acta Mater.*, vol. 49, no. 11, pp. 2017–2026, 2001.

[54] T. Neeraj and M. J. Mills, “Short-range order (SRO) and its effect on the primary creep behavior of a Ti-6wt.%Al alloy,” *Mater. Sci. Eng. A*, vol. 319–321, pp. 415–419, 2001.

[55] M. C. Brandes, M. J. Mills, J. C. Williams, G. S. Daehn, and A. P. Woodfield, “CREEP, FATIGUE, AND DEFORMATION OF α AND α-β,” 2008.

[56] Z. Song and D. W. Hoeppner, “Dwell time effects on the fatigue behaviour of titanium alloys,” *Int. J. Fatigue*, vol. 10, no. 4, pp. 211–218, 1988.

[57] J. T. Ryder, D. E. Pettit, W. E. Krupp, and D. W. Hoeppner, “Final Report on Evaluation of Mehcanical Property Characteristics of IMI 685,” Rye Canyon Laboratory, 1973.

[58] M. R. Bache, M. Cope, H. M. Davies, W. J. Evans, and G. Harrison, “Dwell sensitive fatigue in a near alpha titanium alloy at ambient temperature,” vol. 19, no. 1, pp. 83–88, 1998.

[59] M. C. Brandes, M. J. Mills, and J. C. Williams, “The Influence of Slip Character on the Creep and Fatigue Fracture of an a Ti-Al Alloy,” vol. 41, no. December, pp. 3463–3472, 2010.

[60] S. Hémery, V. T. Dang, L. Signor, and P. Villechaise, “Influence of Microtexture on Early Plastic Slip Activity in Ti-6Al-4V Polycrystals,” *Metall. Mater. Trans. A Phys. Metall. Mater. Sci.*, vol. 49, no. 6, pp. 2048–2056, 2018.

[61] Z. Zhang, D. Lunt, H. Abdolvand, A. J. Wilkinson, M. Preuss, and F. P. E. Dunne, “Quantitative investigation of micro slip and localization in polycrystalline materials under uniaxial tension,” *Int. J. Plast.*, vol. 108, no. April, pp. 88–106, 2018.

[62] A. L. Pilchak and J. C. Williams, “Observations of facet formation in near-α titanium and comments on the role of hydrogen,” *Metall. Mater. Trans. A Phys. Metall. Mater. Sci.*, vol. 42, no. 4, pp. 1000–1027, 2011.

[63] A. L. Pilchak, M. C. Brandes, R. E. A. Williams, and J. C. Williams, “Investigation of faceted crack initiation and propagation in near-alpha titanium alloys,” in *Ti 2011 - Proceedings of the 12th World Conference on Titanium*, 2012, vol. 2, pp. 993–997.

[64] I. Bantounas, T. C. Lindley, D. Rugg, and D. Dye, “Effect of microtexture on fatigue cracking in Ti – 6Al – 4V,” vol. 55, pp. 5655–5665, 2007.

[65] F. P. E. Dunne, D. Rugg, and A. Walker, “Lengthscale-dependent, elastically anisotropic, physically-based hcp crystal plasticity: Application to cold-dwell fatigue in Ti alloys,” *Int. J. Plast.*, vol. 23, no. 6, pp. 1061–1083, Jun. 2007.

[66] M. Anahid, P. Chakraborty, D. S. Joseph, and S. Ghosh, “Wavelet decomposed dual-time scale crystal plasticity FE model for analyzing cyclic deformation induced crack nucleation in polycrystals,” *Model. Simul. Mater. Sci. Eng.*, vol. 17, no. 6, 2009.

[67] M. Anahid, M. K. Samal, and S. Ghosh, “Dwell fatigue crack nucleation model based on crystal plasticity finite element simulations of polycrystalline titanium alloys,” *J. Mech. Phys. Solids*, vol. 59, no. 10, pp. 2157–2176, 2011.

[68] S. Ghosh and M. Anahid, “Homogenized constitutive and fatigue nucleation models from crystal plasticity FE simulations of Ti alloys, Part 1: Macroscopic anisotropic yield function,” *Int. J. Plast.*, vol. 47, pp. 182–201, 2013.

[69] M. Anahid and S. Ghosh, “Homogenized constitutive and fatigue nucleation models from crystal plasticity FE simulations of Ti alloys, Part 2: Macroscopic probabilistic crack nucleation model,” *Int. J. Plast.*, vol. 48, pp. 111–124, 2013.

[70] F. P. E. Dunne, A. Walker, and D. Rugg, “A systematic study of hcp crystal orientation and morphology effects in polycrystal deformation and fatigue,” *Proc. R. Soc. A Math. Phys. Eng. Sci.*, vol. 463, no. 2082, pp. 1467–1489, 2007.

[71] Z. Zheng, D. S. Balint, and F. P. E. Dunne, “Discrete dislocation and crystal plasticity analyses of load shedding in polycrystalline titanium alloys,” *Int. J. Plast.*, vol. 87, pp. 15–31, 2016.

[72] W. J. Evans and C. R. Gostelow, “The effect of hold time on the fatigue properties of a β-processed titanium alloy,” *Metall. Trans. A*, vol. 10, no. 12, pp. 1837–1846, Dec. 1979.

[73] E. E. Sackett, L. Germain, and M. R. Bache, “International Journalof Fatigue Crystal plasticity , fatigue crack initiation and fatigue performance of advanced titanium alloys,” vol. 29, no. 2007, pp. 2015–2021, 2015.

[74] V. Sinha, M. J. Mills, and J. C. Williams, “Understanding the Contributions of Normal-Fatigue and Static Loading to the Dwell Fatigue in a Near-Alpha Titanium Alloy,” vol. 35, no. OCTOBER, pp. 3141–3148, 2004.

[75] M. R. Bache, W. J. Evans, and H. M. Davies, “Electron back scattered diffraction (EBSD) analysis of quasi-cleavage and hydrogen induced fractures under cyclic and dwell loading in titanium alloys,” *J. Mater. Sci.*, vol. 32, no. 13, pp. 3435–3442, 1997.

[76] M. R. Winstone and M. J. Weaver, “THE STRAIN CONTROLLED FATIGUE BEHAVIOUR OF A NEAR-ALPHA TITANIUM ALLOY,” in *Titanium science and technology : proceedings of the fifth International Conference on Titanium*, 1984, pp. 2275–2280.

[77] Z. Zheng, F. P. E. Dunne, Z. Zheng, and F. P. E. Dunne, “Mechanistic basis of temperature-dependent dwell fatigue in titanium alloys,” *J. Mech. Phys. Solids*, vol. 107, pp. 185–203, 2017.

[78] T.-S. Jun, Z. Zhang, G. Sernicola, F. P. E. Dunne, and T. B. Britton, “Local strain rate sensitivity of single α phase within a dual-phase Ti alloy,” *Acta Mater.*, vol. 107, pp. 298–309, 2016.

[79] K. May, “Small Scale Tensile Testing of Titanium Alloys,” *PhD Thesis*, pp. 1–61, 2010.

[80] F. P. E. Dunne and D. Rugg, “On the mechanisms of fatigue facet nucleation in titanium alloys,” *Fatigue Fract. Eng. Mater. Struct.*, vol. 31, no. 11, pp. 949–958, 2008.

[81] K. Kirane and S. Ghosh, “A cold dwell fatigue crack nucleation criterion for polycrystalline Ti-6242 using grain-level crystal plasticity FE Model,” vol. 30, pp. 2127–2139, 2008.

[82] T.-S. Jun, D. E. J. Armstrong, and T. B. Britton, “A nanoindentation investigation of local strain rate sensitivity in dual-phase Ti alloys,” *J. Alloys Compd.*, vol. 672, pp. 282–291, 2016.

[83] D. R. Chichili, K. T. Ramesh, and K. J. Hemker, “The high-strain-rate response of alpha-titanium: Experiments, deformation mechanisms and modeling,” *Acta Mater.*, vol. 46, no. 3, pp. 1025–1043, 1998.

[84] Z. Zheng, D. S. Balint, and F. P. E. Dunne, “Dwell fatigue in two Ti alloys : An integrated

crystal plasticity and discrete dislocation study," *J. Mech. Phys. Solids*, vol. 96, pp. 411–427, 2016.

[85] G. Regazzoni, U. F. Kocks, and P. S. Follansbee, "Dislocation kinetics at high strain rates," *Acta Metall.*, vol. 35, no. 12, pp. 2865–2875, 1987.

[86] D. Rugg, M. Dixon, and F. P. E. Dunne, "Effective structural unit size in titanium alloys," *J. Strain Anal. Eng. Des.*, vol. 42, no. 4, pp. 269–279, 2007.

[87] K. Le Biavant, S. Pommier, and C. Prioul, "Local texture and fatigue crack initiation in a Ti-6Al-4V titanium alloy," *Fatigue Fract. Eng. Mater. Struct.*, vol. 25, no. 6, pp. 527–545, Jun. 2002.

[88] M. G. Glavicic, B. B. Bartha, S. K. Jha, and C. J. Szczepanski, "The origins of microtexture in duplex Ti alloys," *Mater. Sci. Eng. A*, vol. 513–514, no. C, pp. 325–328, 2009.

[89] L. Germain, N. Gey, M. Humbert, P. Bocher, and M. Jahazi, "Analysis of sharp microtexture heterogeneities in a bimodal IMI 834 billet," *Acta Mater.*, vol. 53, no. 13, pp. 3535–3543, 2005.

[90] M. P. Echlin, J. C. Stinville, V. M. Miller, W. C. Lenthe, and T. M. Pollock, "Incipient slip and long range plastic strain localization in microtextured Ti-6Al-4V titanium," *Acta Mater.*, vol. 114, pp. 164–175, 2016.

[91] D. Lunt, J. Q. da Fonseca, D. Rugg, and M. Preuss, "Microscopic strain localisation in Ti-6Al-4V during uniaxial tensile loading," *Mater. Sci. Eng. A*, vol. 680, no. October 2016, pp. 444–453, Jan. 2017.

[92] M. A. Sutton, N. Li, D. C. Joy, A. P. Reynolds, and X. Li, "Scanning Electron Microscopy for Quantitative Small and Large Deformation Measurements Part I : SEM Imaging at Magnifications from 200 to 10 , 000," pp. 775–787, 2007.

[93] M. A. Sutton *et al.*, "Recent Progress in Digital Image Correlation: Background and Developments since the 2013 W M Murray Lecture," *Exp. Mech.*, vol. 57, no. 1, pp. 1–30, Jan. 2017.

[94] A. D. Kammers and S. Daly, "Digital Image Correlation under Scanning Electron Microscopy: Methodology and Validation," *Exp. Mech.*, vol. 53, no. 9, pp. 1743–1761, 2013.

[95] W. C. Lenthe, J. C. Stinville, M. P. Echlin, Z. Chen, S. Daly, and T. M. Pollock, "Advanced detector signal acquisition and electron beam scanning for high resolution SEM imaging," *Ultramicroscopy*, vol. 195, no. September, pp. 93–100, 2018.

[96] Z. Chen, W. Lenthe, J. C. Stinville, M. Echlin, T. M. Pollock, and S. Daly, "High-Resolution Deformation Mapping Across Large Fields of View Using Scanning Electron Microscopy and Digital Image Correlation," *Exp. Mech.*, vol. 58, no. 9, pp. 1407–1421, 2018.

[97] C. B. Montgomery, B. Koohbor, and N. R. Sottos, "A Robust Patterning Technique for Electron Microscopy-Based Digital Image Correlation at Sub-Micron Resolutions," *Exp. Mech.*, vol. 59, no. 7, pp. 1063–1073, 2019.

[98] R. Manual, "Vic-2D."

[99] Z. Chen and S. Daly, "Deformation twin identification in magnesium through clustering and computer vision," *Mater. Sci. Eng. A*, vol. 736, no. July, pp. 61–75, 2018.

[100] Z. Chen and S. H. Daly, "Active Slip System Identification in Polycrystalline Metals by Digital Image Correlation (DIC)," *Exp. Mech.*, vol. 57, no. 1, pp. 115–127, 2017.

[101] F. Bachmann, R. Hielscher, and H. Schaeben, "Texture analysis with MTEX- Free and

open source software toolbox," *Solid State Phenom.*, vol. 160, pp. 63–68, 2010.

[102] M. A. Groeber and M. A. Jackson, "DREAM.3D: A Digital Representation Environment for the Analysis of Microstructure in 3D," *Integr. Mater. Manuf. Innov.*, vol. 3, no. 1, pp. 56–72, 2014.

[103] V. Venkatesh *et al.*, "Icme of Microtexture Evolution in Dual Phase Titanium Alloys," in *Proceedings of the 13th World Conference on Titanium*, vol. VI, no. 1, Hoboken, NJ, USA: John Wiley & Sons, Inc., 2016, pp. 1907–1912.

[104] A. L. Pilchak, "A simple model to account for the role of microtexture on fatigue and dwell fatigue lifetimes of titanium alloys," *Scr. Mater.*, vol. 74, pp. 68–71, 2014.

[105] I. Bantounas, D. Dye, and T. C. Lindley, "The effect of grain orientation on fracture morphology during high-cycle fatigue of Ti-6Al-4V," *Acta Mater.*, vol. 57, no. 12, pp. 3584–3595, 2009.

[106] S. L. Wong and P. R. Dawson, "Influence of directional strength-to-stiffness on the elastic-plastic transition of fcc polycrystals under uniaxial tensile loading," *Acta Mater.*, vol. 58, no. 5, pp. 1658–1678, Mar. 2010.

[107] M. Kasemer, M. P. Echlin, J. C. Stinville, T. M. Pollock, and P. Dawson, "On slip initiation in equiaxed α/β Ti-6Al-4V," *Acta Mater.*, vol. 136, pp. 288–302, 2017.

[108] S. L. Wong and P. R. Dawson, "Influence of directional strength-to-stiffness on the elastic-plastic transition of fcc polycrystals under uniaxial tensile loading," *Acta Mater.*, vol. 58, no. 5, pp. 1658–1678, Mar. 2010.

[109] W. F. Hosford, *The mechanics of crystals and textured polycrystals*. New York: Oxford University Press, 1993.

[110] J.-Y. Kim, V. V. Yakovlev, and S. L. Rokhlin, "Line-focus acoustic microscopy of Ti-6242 α/β single colony: determination of elastic constants," in *AIP Conference Proceedings*, 2002, vol. 615, no. May 2002, pp. 1118–1125.

[111] T. J. Turner, P. A. Shade, J. C. Schuren, and M. A. Groeber, "The influence of microstructure on surface strain distributions in a nickel micro-tension specimen," *Model. Simul. Mater. Sci. Eng.*, vol. 21, no. 1, 2013.

[112] T. J. Turner, P. A. Shade, J. Schuren, M. A. Groeber, M. Miller, and M. D. Uchic, "Two Integrated Experimental and Modeling Approaches to Study Strain Distributions in Nickel and Nickel-Base Superalloy Polycrystals," *Superalloys 2012*, pp. 643–652, 2012.

[113] X. Song, S. Y. Zhang, D. Dini, and A. M. Korsunsky, "Finite element modelling and diffraction measurement of elastic strains during tensile deformation of HCP polycrystals," *Comput. Mater. Sci.*, vol. 44, no. 1, pp. 131–137, 2008.

[114] F. Bridier, D. L. McDowell, P. Villechaise, and J. Mendez, "Crystal plasticity modeling of slip activity in Ti-6Al-4V under high cycle fatigue loading," *Int. J. Plast.*, vol. 25, no. 6, pp. 1066–1082, 2009.

[115] Y. Yang *et al.*, "Characterization and modeling of heterogeneous deformation in commercial purity titanium," *Jom*, vol. 63, no. 9, pp. 66–73, 2011.

[116] S. Waheed, Z. Zheng, D. S. Balint, and F. P. E. Dunne, "Microstructural effects on strain rate and dwell sensitivity in dual-phase titanium alloys," *Acta Mater.*, vol. 162, pp. 136–148, 2019.

[117] J. C. Stinville *et al.*, "Time-Resolved Digital Image Correlation in the Scanning Electron Microscope for Analysis of Time-Dependent Mechanisms," *Exp. Mech.*, 2020.